Structural optimization of nanostructured aluminum for enhancing mechanical properties and formability

Kidmose, Jacob

Publication date:
2014

Document Version
Publisher's PDF, also known as Version of record

Structural optimization of nanostructured aluminum for enhancing mechanical properties and formability

DTU Vindenergi
PhD Rapport 2014

Jacob Kidmose

DTU Wind Energy PhD-0038 (EN)

February 2014

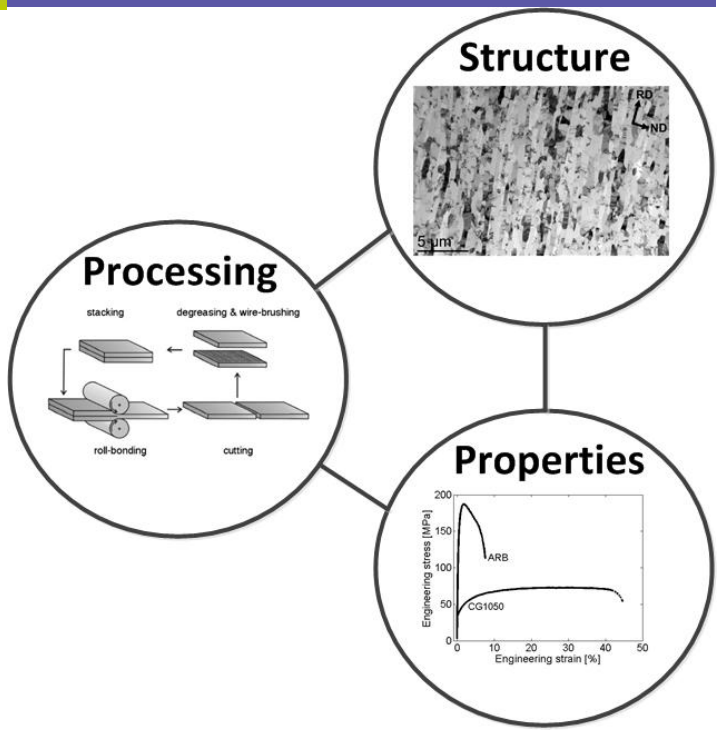

DTU Vindenergi
Institut for Vindenergi

Forfatter(e): Jacob Kidmose

Titel: Structural optimization of nanostructured aluminum for enhancing mechanical properties and formability

Institut: Department of Wind Energy

Resume:
The aim of this project is i) to optimize processing parameters of accumulative roll bonding (ARB) to produce a nanostructure of a commercial pure aluminium (Al1050), ii) to apply post-ARB process treatments in the form of thermal annealing or plastic deformation to tailor the structure and mechanical properties, iii) to do a detailed experimental investigation of the onset and evolution of strain localization and iv) to investigate the performance of the sheets produced using standard formability tests.

Two processing parameters of ARB, wire brushing and stacking, were carefully improved so ARB processing succeeded in producing nanostructured metal sheets with a width of up to 190 mm, allowing standard formability tests to be performed.

The initial coarse grained Al1050 had a yield strength of 39 MPa and a total tensile elongation of about 45%. The as-ARB processed nanostructured Al1050 sheets showed an enhanced yield strength (135 MPa) but limited tensile ductility (7%). Post-process thermal annealing at a medium temperature (225°C) resulted in a good compromise between strength and ductility. The yield stress (98 MPa) is more than twice that of the initial material and the total elongation was restored to around 28%, which is nearly four times of that of the as-ARB state.

Post-process deformation by cold rolling up to 50% thickness reductions led to a small change in strength but gradually and monotonically increase in tensile elongation as compared with the as-ARB state. After 50% post-process cold rolling, the yield strength (138 MPa) was maintained comparable with the as-ARB sheet, while the total tensile elongation was increased to 17%, which is more than twice of the ARB state.

Tensile behavior analysis done by an advanced digital image correlation technique (ARAMIS) showed that the onset of localized deformation occurred at a very low strain for the as-processed nanostructured metal even before the UTS, which had not been observed before. The localized deformation developed into a shear band by further tensile straining. After 50% post-process rolling only small localizations were observed and they did not develop before the very end of the test.

Formability testing results showed that the ARB conditions perform much better in the biaxial stress region than in uniaxial tension. In particular the ARB and the medium temperature annealed conditions exhibited biaxial stretching capabilities close to that of initial material while the post process cold rolled sheets perform slightly poorer but still better than the Al1050 sheets conventionally cold rolled to similar thickness reductions.

DTU Wind Energy PhD-0038 (EN)
February 2014

Projektperiode:
2010.01.01-2014.28.02

Uddannelse:
PhD

Område:
Wind Energy

Vejledere:
Xiaoxu Huang
Grethe Winther

Kontrakt nr.:
DNRF86-5
51261130091

Projektnr.:
DTU Wind Energy PhD-0038 (EN)

Sponsorship:
Danish National Research Foundation
National Natural Science Foundation of China

ISBN:
978-87-92896-85-8

Sider: 152
Referencer: 93

Danmarks Tekniske Universitet
DTU Vindenergi
Nils Koppels Allé
Bygning 403
2800 Kgs. Lyngby
Telefon

www.vindenergi.dtu.dk

Structural optimization of nanostructured aluminum for enhancing mechanical properties and formability

Jacob Kidmose

Supervised by Xiaoxu Huang and Grethe Winther

Technical University of Denmark

Department of Wind Energy

12th May 2014

Contents

Contents **iii**

1 Introduction **5**

2 Background **9**

2.1 Structural evolution with strain 9

2.2 Processing of nanostructured metals by deformation 13

2.2.1 Accumulative roll-bonding (ARB) 14

2.3 Structure and properties of nanostructured metals 15

2.3.1 Characteristic structures 16

2.3.2 Characteristic mechanical properties 17

2.3.2.1 Tensile strength and ductility 17

2.3.2.2 Strain rate sensitivity 19

2.4 Effects of post-processing treatments (P-PT) 21

2.4.1 Annealing 21

2.4.2 Deformation 24

2.5 Formability of nanometals 26

2.6 Objective and overview of the thesis 29

3 Material and processing **33**

3.1 Starting material 33

3.2 Optimization of ARB processing 34
3.2.1 Edge cracking 36
3.3 Scaling up of sample dimensions 37
3.3.1 Homogeneity of the sheet 37
3.4 Post-process treatments 38
3.4.1 Annealing 39
3.4.2 Deformation 39

4 Mechanical and structural characterization 41
4.1 Mechanical testing 41
4.1.1 Conventional tensile tests 41
4.1.2 Strain rate jump tests 43
4.1.3 The ARAMIS system 43
4.1.3.1 Tensile tests 43
4.1.3.1.1 Tensile behavior 48
4.1.3.2 Anisotropy 49
4.1.4 True stress-strain curves 52
4.2 Formability testing 55
4.2.1 Erichsen test 55
4.2.2 Bulge test 57
4.2.2.1 Strain measurement 59
4.2.2.2 Forming limit diagram 60
4.3 Microstructural investigation 61
4.3.1 Electron backscatter diffraction (EBSD) 61
4.3.1.1 Texture of CG1050 63
4.3.2 Transmission electron microscopy (TEM) 65

5 Structure and tensile behavior of nanostructured Al 67

5.1 Structure 67
5.2 Texture 71
5.3 Tensile properties 73
5.3.1 Anisotropy 75
5.4 ARAMIS analysis of strain evolution during tensile testing . 76
5.4.1 Pre-UTS behavior 77
5.4.2 Post-UTS behavior 79
5.4.3 Width strain 80
5.5 Discussion 82
5.5.1 Structure and strength 82
5.5.2 Texture 83
5.5.3 Anisotropy 84
5.5.4 Tensile instability 86
5.6 Summary 88

6 Effects of Post-Process Treatment (P-PT) on structure and tensile behavior 91

6.1 Annealing 91
6.1.1 Structure 92
6.1.2 Texture 97
6.1.3 Tensile properties 100
6.1.4 Anisotropy 102
6.1.5 ARAMIS analysis of strain evolution during tensile testing 102
6.1.5.1 ARB-225 103
6.2 Deformation 105
6.2.1 Structure 105
6.2.2 Texture 106

6.2.3 Tensile properties 109
6.2.4 Anisotropy 110
6.2.5 ARAMIS analysis of strain evolution during tensile testing 111
6.2.5.1 Pre-UTS behavior 111
6.2.5.2 Post-UTS behavior 113
6.2.5.3 Width strain 114
6.3 Discussion 115
6.3.1 Tensile instability enhanced by annealing 116
6.3.2 Tensile stability enhanced by deformation 118
6.3.2.1 Annealing followed by deformation 119
6.3.2.1.1 ARB-175-CR 119
6.3.2.1.2 ARB-225-CR 120
6.4 Summery 124

7 Effects of post-process treatments on the formability of nanostructured Al 127

7.1 Bulge test 127
7.1.1 Lüders band observation 128
7.1.1.1 Discussion of the raw data 129
7.1.2 Swift theory 131
7.1.3 Applying Swift 132
7.1.4 Fitting 135
7.1.5 Forming limit diagram 135
7.2 Discussion of the forming limit diagram 137
7.3 Erichsen test 140
7.3.1 Thickness effect 142
7.4 Discussion of the Erichsen tests 144

7.5 Summary 146

8 Conclusions and outlook **149**

Bibliography **153**

Preface

This thesis is submitted in partial fulfillment of the requirements for the PhD degree at the Technical University of Denmark. The project was carried out within the Danish-Chinese Center for Nanometals, Section for Materials Science and Advanced Characterization, Department of Wind Energy, under the supervision of senior scientists, Drs. Xiaoxu Huang and Grethe Winther. The study was conducted during the period from January 2010 to February 2014.

I am grateful to the Head of Section Dorte Juul Jensen, who gave me the opportunity to work within the Danish-Chinese Center for Nanometals. I am thankful to my supervisors Xiaoxu Huang and Grethe Winther, who have provided me with constant support and many useful discussions. I am deeply indebted to Dr. Niels Hansen, who instructed, enlightened, and encouraged me all the time. I spent 3 month at Shenyang National Laboratory for Materials Science where I did all my experiments associated with the ARAMIS system and formability testing. I gracefully thank Prof. Lei Lu and her group for all their help during my training and performing experiments with the ARAMIS system. Likewise I would like to thank Prof. Shihong Zhang and his group especially Dr. Ming Cheng for their help with my formability experiments. I would also like to thank Prof. Brian Ralph, Prof. Povl Brøndsted, Drs. Wolfgang Pantleon, Jette Oddershede, Yubin

Zhang, Tianbo Yu, Fengxiang Liu and Chuanshi Hong who all have helped me during my time as a PhD. Special thanks to the very skilful technicians, Gitte Christiansen, Preben Olesen, Lars Lorentzen and Frank Adrian for their help. I would also like to thank present and former co-workers.
Finally, I would like to thank my family, friends but especially my girlfriend, Dong Thao Quan, for supporting me throughout the years.

Publications

- Kidmose, J., Cai, Y., Hansen, N., Winther, G., and Huang, X. Strain rate dependence of the flow stress in nanostructured aluminium sheets produced by accumulative roll bonding. 31th Risoe International Symposium and Material Science, 2010.

- Kidmose, J., Lu, L., Winther, G., Hansen, N., and Huang, X. Strain distribution during tensile deformation of nanostructured aluminum samples. Journal of Materials Science, 2012, pages 1-7.

- Kidmose, J., Lu, L., Hansen, N., Winther, G., and Huang, X. Onset of strain localisation in nanostructured aluminium. 33rd Risoe International Symposium and Material Science, 2012, pages 265-270.

- Kidmose, J., Zhang, S.H., Cheng, M., Hansen, N., Winther, G., and Huang, X. Formabilty of nanostructured aluminium (in preparation).

Chapter 1

Introduction

Since the bronze age man has used metals due to their high strength and their ability to be shaped. The evolution of society has gone hand in hand with the ability of the more advanced use of metals. Especially in the industrialization the use of metals was a key element to the world we know today. Cars and airplanes all the time strive to be faster or more fuel efficient and one way of doing this is by decreasing weight. Therefore more and more research goes into light and strong metals. Nanostructured metals (metals with grain sizes in the sub-micrometer to nanometer regime) are promising emerging light and strong metals. In the 1950s Hall (Hall, 1951; Petch, 1953) introduced to relationship between yield stress and grain size and later Petch derived strength-structure relationship named Hall-Petch (H-P) where the yield stress is proportional to the inverse square root of the grain size of a metal. This indicates that decreasing the grain size will increase the strength of the metal. With this strength-structure relationship there has been a constant strive to decrease grain sizes further and further to achieve increasingly stronger metals. This strive which is defined as metals with internal boundaries with a spacing below $1\mu m$ has led to nano-

structured metals. A more detailed description of nanostructured metals is given in the next chapter.
In general nanostructured metals achieve strengths 2-4 times higher than that of the coarse grained metals but low ductility. Its therefore crucial to improve the strength-ductility combination of nanostructured metals for exploring their industrial application. There are also practical problems to produce acceptable bulk sample sizes which strongly impedes industrial applications of nanostructured metals. Further nanostructured metals needs to be characterized in more advanced deformation modes than uniaxial tension to obtain relevant mechanical parameters. For example formability is extremely important for the application of sheet metals because many of the structural metal parts used every day are formed from a sheet into the final shape of the part by e.g. deep drawing, extrusion or stretching operations.

In this project, we apply accumulative roll bonding (ARB) to produce nanostructured sheets of a commercial purity aluminium (Al1050). Efforts are made to optimize ARB processing parameters to produce nanostructured metal sheets of large dimensions. Post-process treatments in the form of thermal annealing and deformation are applied to optimize the structure and mechanical properties. The formability of the sheets produced is characterized using standard formability tests including bulge tests and Erichsen tests.

In brief, the structure of the thesis is as follows: Chapter 2 gives a short review of the background; Chapter 3 presents the selected material and its processing; Chapter 4 introduces the mechanical and microstructural char-

acterization techniques; Chapter 5 characterizes the structure and tensile behavior of the nanostructured metal; Chapter 6 reports the effects of post-process treatments (P-PT) on the structure and tensile behavior; Chapter 7 investigates the formability of the materials; and Chapter 8 gives conclusions and outlook.

Chapter 2

Background

2.1 Structural evolution with strain

The structural evolution during plastic deformation has been studied extensively and a short summary is given here. During plastic deformation most of the energy is transformed into heat but a small amount of the mechanical energy is stored in the metal, mostly in the form of dislocations. The dislocations are not randomly distributed but they accumulate in dislocation boundaries that separate regions with a relatively low dislocation density. The key structural parameters characterizing deformed metals are the structural morphology, spacing between boundaries, misorientation across boundaries, and density of interior dislocations present in the volume between the boundaries (Hansen et al., 2001; Huang, 2007).

Two examples showing the structural evolution of deformation done by cold rolling are shown in Fig. 2.1 (Liu et al., 1998) and Fig. 2.2 (Liu et al., 2002). Fig. 2.1 shows a typical microstucture for lightly cold rolled metals of medium to high stacking fault energy. The microstructure consists of ran-

domly orientated cell boundaries in between planar dislocation boundaries, which delineate cell blocks. The planar cell block boundaries have the misorientation given and are referred to as geometrically necessary boundaries (GNBs). The cell boundaries are formed by statistical trapping of dislocations, and are therefore termed incidental dislocation boundaries (IDBs). The GNBs most often have several to a few IDBs along their length. Fig. 2.1 also shows that the planar cell block boundaries are inclined about 40° to the rolling direction (RD) at low strain.

At increasing rolling strain, the structural evolution brings the cell block structure into a macroscopic orientation almost parallel to the rolling plane. This is shown in Fig. 2.2(a) where the cell block structure is a typical lamellar structure, with lamellar boundaries nearly parallel to the rolling plane and short interconnecting boundaries forming a bamboo structure. The lamellar boundaries are high-angle boundaries ($\theta \geq 15°$) or dislocation boundaries ($\theta \leq 15°$) whereas the interconnecting boundaries are typically low angle boundaries (see Fig. 2.2(b)). In the volumes between the boundaries, individual dislocations and loose dislocation tangles can be observed. The crystallographic orientations of the cell blocks consist of typical rolling texture components copper $\{112\}\left\langle 11\bar{1}\right\rangle$, S $\{123\}\left\langle 63\bar{4}\right\rangle$ and brass $\{110\}\left\langle \bar{1}12\right\rangle$ (see Fig. 2.2(c)). It is not an entire grain that rotates into a new position as the deformation texture evolves. Individual parts of a grain can rotate toward different orientations, and the mutually misoriented cell blocks comprise the (macroscopic) texture components (Hansen et al., 2001; Liu et al., 2002).

The microstructural evolution within a grain follows a general pattern of a continuous reduction in cell block size and an increase in misorientation angle across dislocation boundaries (Hansen et al., 2001). This is clearly

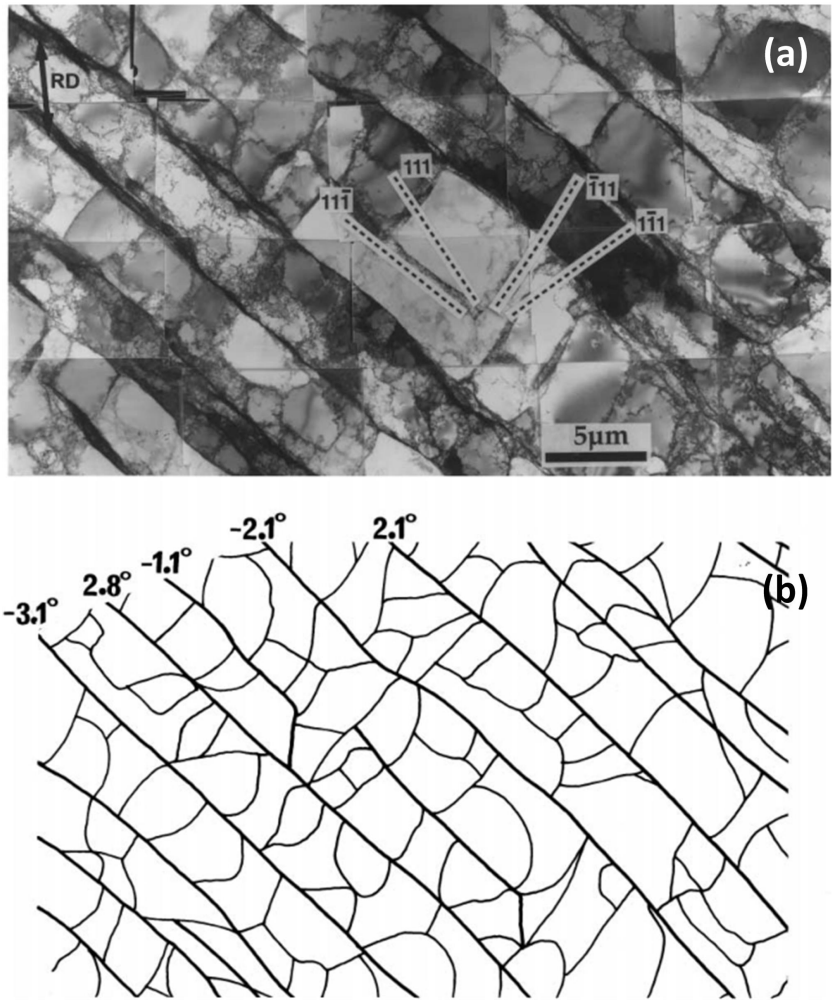

Figure 2.1: *A TEM image of a cell-block structure of a 99.996% pure Al with a starting grain size of 300μm sample cold-rolled 10% seen in the transverse direction. (Liu et al., 1998) (b) The sketch shows the cell-block boundaries and ordinary cell boundaries. The misorientation angles across the cell-block boundaries is marked on the sketch. The signs are determined by considering the misorientation across the boundaries from the left to right around axes which have the same sense. (Liu et al., 1998)*

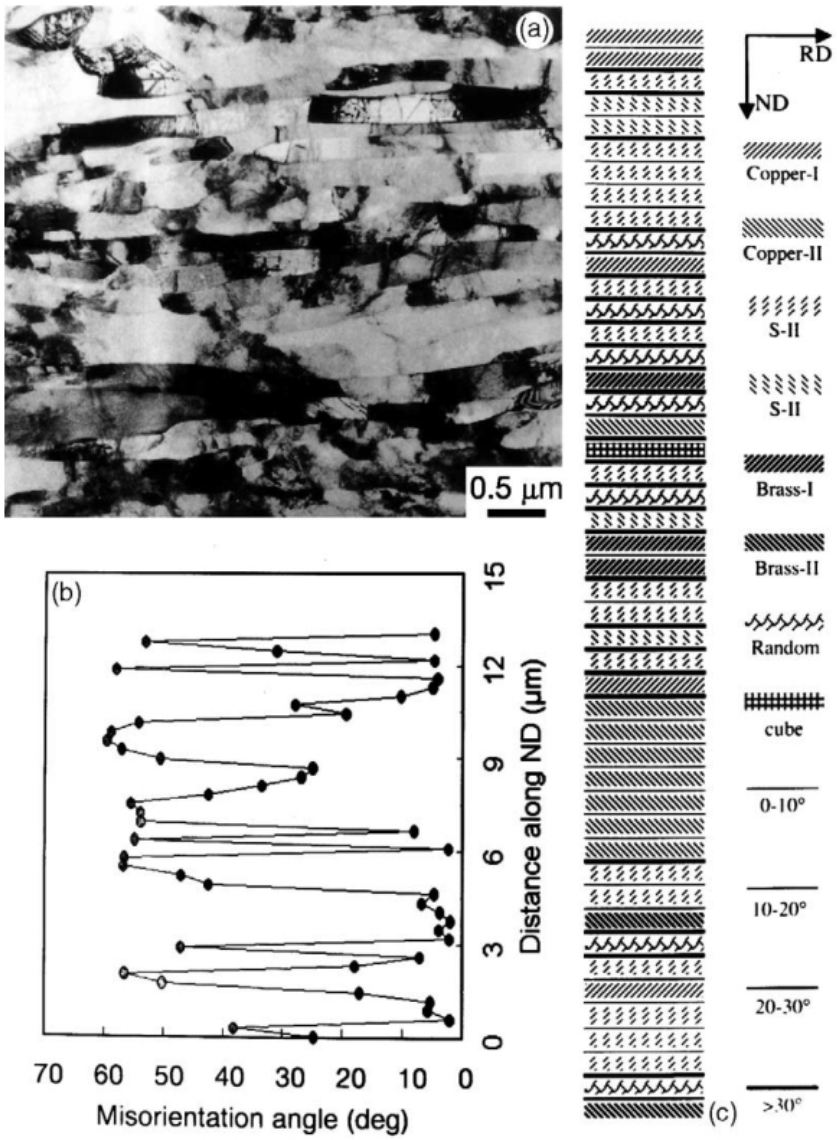

Figure 2.2: *Microstructure and crystallography of a 1200 Al specimen cold-rolled to a strain of 5.0. (a) A typical lamellar structure. (b) The misorientation across the lamellar boundaries measured along ND. (c) Rolling texture components in the lamellar structure. (Liu et al., 2002)*

seen in Fig. 2.3 where the average GNB spacing (D_{av}^{GNB}) and misorientation angle (θ_{av}^{GNB}) are shown as a function of strain.

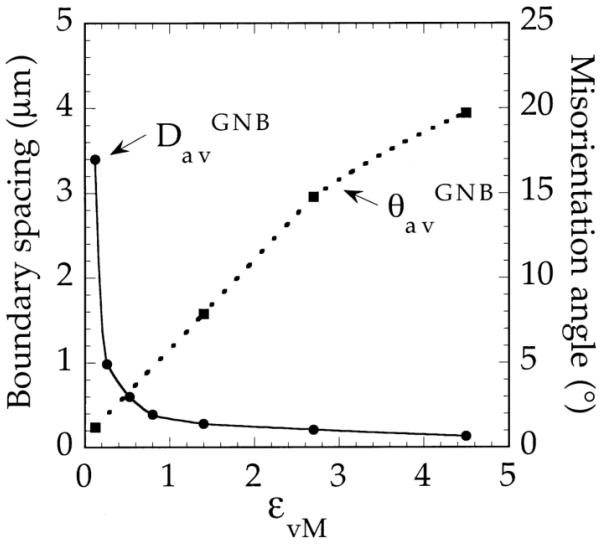

Figure 2.3: *The average GNB spacing (D_{av}^{GNB}) and misorientation angle (θ_{av}^{GNB}) as a function of rolling strain for Ni (Hughes and Hansen, 2000).*

2.2 Processing of nanostructured metals by deformation

Processing of bulk nanostructured metals can in principle be accomplished by either the bottom-up assembly of atoms or molecules into nanoscale clusters, or the top-down methods which start with a bulk metal and obtain a nanostructure by deformation which led to structural refinement, as described in the previous section.

In the present study a top-down approach is taken to produce nanostructured metals by plastic deformation to high strains, often called severe plastic deformation (SPD) in the literature. In conventional deformation processes like rolling, drawing and extrusion the thickness or diameter of

samples becomes smaller with increasing deformation making it hard to use for structural parts. In order to impose an extremely large strain on the bulk metal without changing the sample shape, several SPD techniques have been developed. Common SPD processes include equal channel angular pressing (ECAP) (Valiev and Langdon, 2006; Iwahashi et al., 1998), high pressure torsion (HPT) (Valiev et al., 1991; Valiev, 1997) and accumulative roll-bonding (ARB) (Saito et al., 1999; Tsuji et al., 2003; Saito et al., 1998). In this study we apply ARB to achieve high strain for structural refinement. The principle and features of the ARB process is briefly described in the following.

2.2.1 Accumulative roll-bonding (ARB)

The ARB processing was develop by Tsuji and his co-workers (Tsuji et al., 1999; Saito et al., 1998). The ARB process consist of 4 steps which are shown in Fig. 2.4.

1. Cutting: A sheet is cut into two.
2. Surface treatment: The surface of the two sheets are carefully degreased and wire brushed.
3. Stacking: The two sheets are accurately stacked on top of each other.
4. Roll bonding: The stacked sheets are rolled from the thickness of two sheets to the thickness of one thereby achieving bonding of the sheets and a thickness reduction of 50% (Corresponding to a von Mises strain of 0.8).

These four steps comprise one ARB cycle. If further cycles are desired the four steps can be repeated. Laboratory scale ARB process has been used by many researchers to produce sheet samples of nanostructured metals. The ARB sheet width that has been reported is in general less than 100

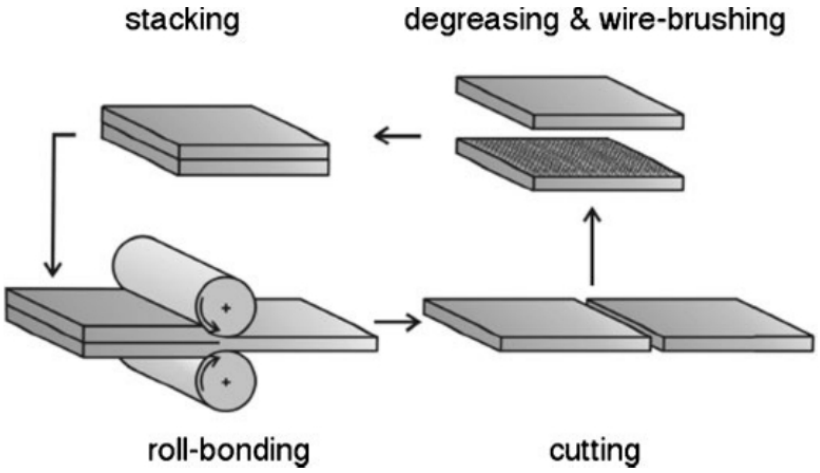

Figure 2.4: *Sketch of one ARB cycle consisting of the following steps. (1) Two sheets are cut into the wished dimensions, (2) The sheets are prepared by degreasing and wire brushing, (3) The sheets are stacked together, (4) The stacked sheets are rolled thereby bonding the sheets. If more than one cycle is performed, step 1 to 4 is repeated until the wished amount of cycles are reached. (Tsuji, 2010)*

mm. However, ARB has the potential of been scaled up in size.

The ARB processing has been applied to several metals and alloys for example aluminium alloys, copper alloys, ferritic steels, austenitic steels and nickel (Tsuji et al., 2003). In the present study ARB processing is used to produce nanostructured aluminium, and efforts are made to optimize the processing parameters (see Chapter 3) to produce sheets of good quality and large dimensions for further testing.

2.3 Structure and properties of nanostructured metals

In this section nanostructured metals produced by ARB will be used to illustrate the characteristic structure and mechanical properties of nano-

structured metals.

2.3.1 Characteristic structures

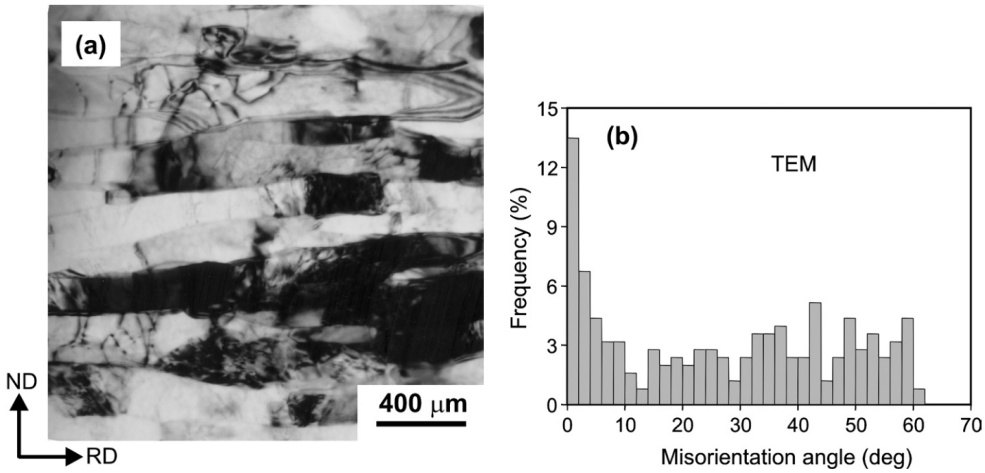

Figure 2.5: *(a) TEM image showing a lamellar structural morphology and dislocation configurations in nanostructured 99.2% pure Al processed by 6-cycle ARB (b) Histogram showing the distribution of boundary misorientation angles (Huang et al., 2008c)*

Fig. 2.5(a) illustrates a TEM microstructure of a commercial purity Al (99.2% purity) sheet processed by 6 ARB cycles showing a well-developed very fine lamellar structure, as in the sample cold rolled to high strains (see Fig. 2.2). Fig. 2.5(b) shows the distribution of misorientation angles measured for all boundaries. A bimodal distribution is seen, with one peak located below 2° and the other located between 40° and 55°. Within the volume between the boundaries, the presence of individual dislocations and dislocation tangles is observed. Sample tilting in the TEM confirmed that almost all lamellae contain dislocations although the dislocation density varies from lamella to lamella (Huang et al., 2008b).

2.3.2 Characteristic mechanical properties

2.3.2.1 Tensile strength and ductility

Nanostructured metals have been reported to have 2-4 times the strength of the conventional coarse grained (CG) metals (Erbel, 1979; Valiev et al., 1993; Saito et al., 1998). Fig. 2.6 shows one example of this.

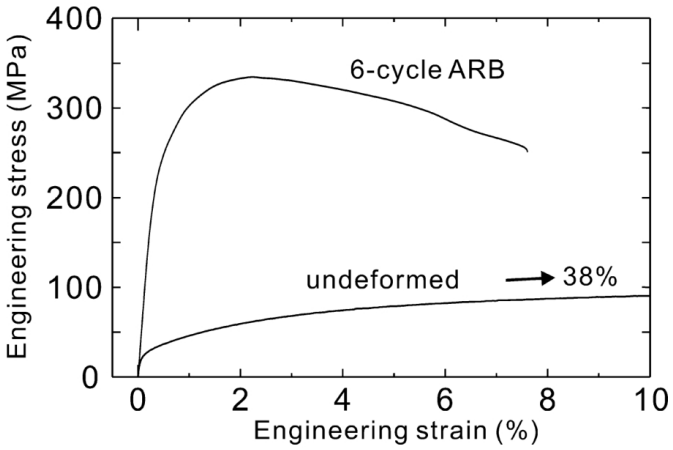

Figure 2.6: *Engineering stress-strain curve for a 99.2% pure aluminium in the undeformed state and processed by 6 cycles of ARB.(Huang et al., 2008c)*

The evolution of mechanical properties with ARB cycles have been studied for Al1100 (Kim et al., 2005). Fig. 2.7 shows the increase in strength with increasing ARB cycles. However, as shown in Fig. 2.7(b), the uniform and total elongations drop dramatically after one cycle from over 35% to less than 5%.

The strength of nanostructured metals is often studied by the strength-structure relationship derived by Hall and Petch in the 1950s (Hall, 1951; Petch, 1953) which relates the yield stress to the inverse square root of grain size. Fig. 2.8 shows one example for nanostructured 99.99% pure aluminium

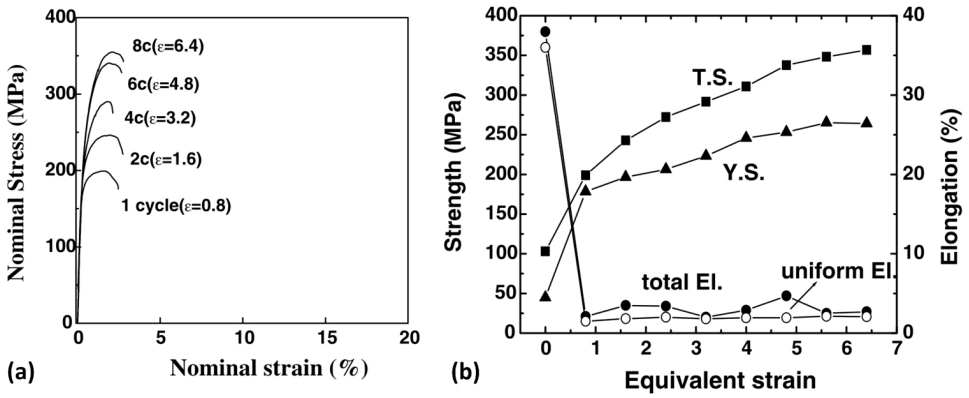

Figure 2.7: *(a) Nominel stress-strain curves for an Al1000 processed with different ARB cycles (Kim et al., 2005) (b) Tensile properties of the ARB processed 1100 Al sheets as a function of equivalent strain where 0.8 corresponds to one ARB cycle.(Kim et al., 2005).*

(Kamikawa et al., 2009).

Here it has been shown that the Hall-Petch relationship is only valid down to the micrometer range, indicating that boundary strengthening is not the only strengthening mechanism operating. One other mechanism is likely to be dislocation strengthening from low-angle dislocation boundaries and individual dislocations between the boundaries (Hansen et al., 2001).

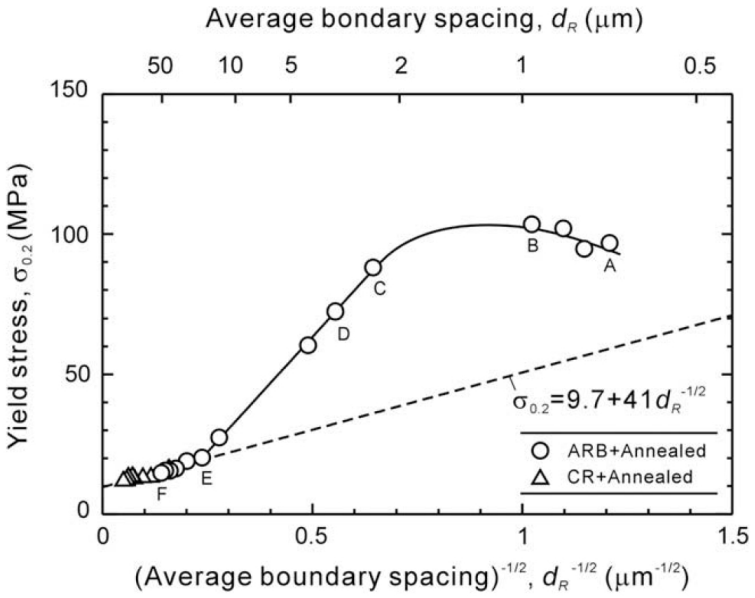

Figure 2.8: *Relationship between yield stress and average boundary spacing (D_R) of a 99.99% pure aluminium procces by ARB + annealed and cold-rolled + annealed samples (Kamikawa et al., 2009)*

2.3.2.2 Strain rate sensitivity

Another pronounced mechanical feature of nanostructured metals is the change in strain rate sensitivity (SRS or m exponent) which has been studied by several authors (Kim et al., 2005; May et al., 2006; Shi et al., 2008; Takata et al., 2008; Isaev et al., 2009; May et al., 2005; Sabirov et al., 2009). A review given by Wei in (Wei, 2007) reports that the general observation is that the SRS of FCC metals increases regardless of the processing techniques used to produce the nanostructured metals. May et al. (2005) has performed strain rate jump tests for a coarse grained (CG) 99.5% pure aluminium and UFG sample processed by eight passes of ECAP at room temperature which are shown in Fig. 2.9. For the CG sample no significant change can be observed when the cross-head speed is changed but for the nanostructured sample clear jumps in the flow stress can be observed. The

relationship between these jumps and the strain rate sensitivity (m) is explained in Section 4.1.2.

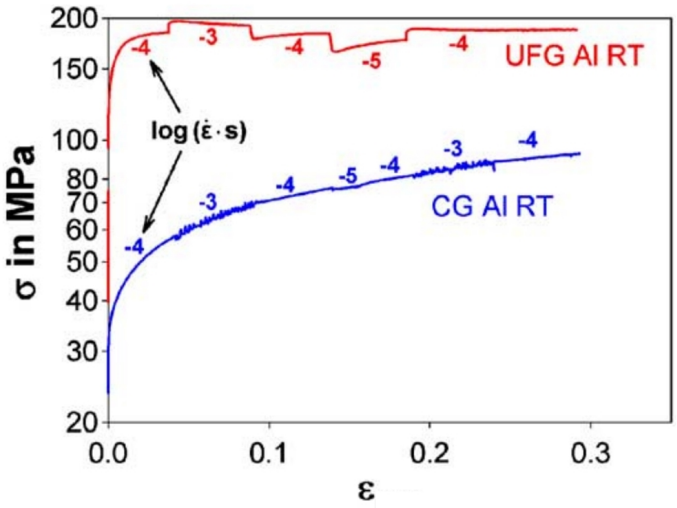

Figure 2.9: *Stress-strain curves from compression tests for nanostructured Al1050 and coarse grained Al1050 including strain rate jumps at room temperature (May et al., 2005).*

Chen et al. (2006) collected and presented the variation of m-exponents as a function of grain size ranging over 5 orders of magnitude of strain rates for Cu (see Fig. 2.10). A 99.998% pure Cu was in Chen et al. (2006) study. It is seen that the m-exponent decrease with increasing grain size and shows nearly no further change as the grain size is larger than 10 μm. Kim et al. (2005) has also reported the m-exponent for a 8011 Al has increased from 0.010-0.015 to 0.047 after 8 cycles of ARB.

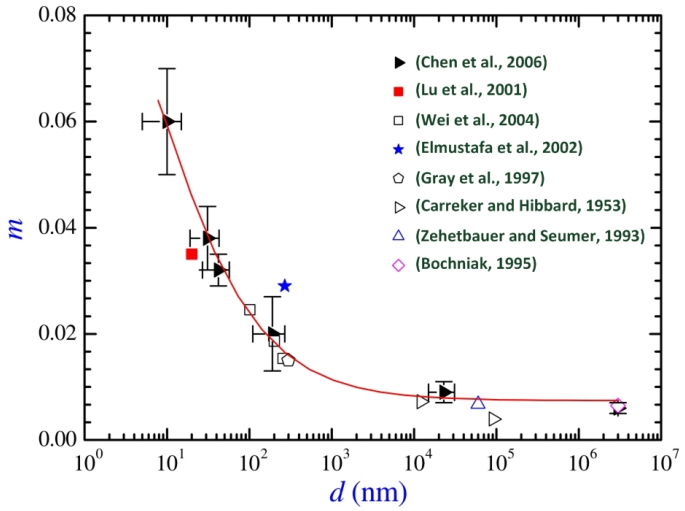

Figure 2.10: *The variation of m as a function of d for Cu using experimental data from the literature ((Carreker and Hibbard, 1953; Wei et al., 2004; Lu et al., 2001; Gray et al., 1997; Zehetbauer and Seumer, 1993; Bochniak, 1995; Elmustafa et al., 2002)) and presented by (Chen et al., 2006).*

2.4 Effects of post-processing treatments (P-PT)

To modify and optimize the microstucture and mechanical properties, post-process treatments by annealing or deformation have been explored. Some interesting results have been reported which are described in the following.

2.4.1 Annealing

The effect of post-process annealing has been studied by Tsuji et al. (2002) for ARB-processed 99.2% Al, and by Yu et al. (2005) for ECAP-processed 99.5% Al. Similar effects on the microstuctural evolution and mechanical properties have been found.

Fig. 2.11 shows the TEM microstructures of a 99.2% pure aluminium specimens annealed for 1.8 ks at different temperatures after 6 cycles of ARB

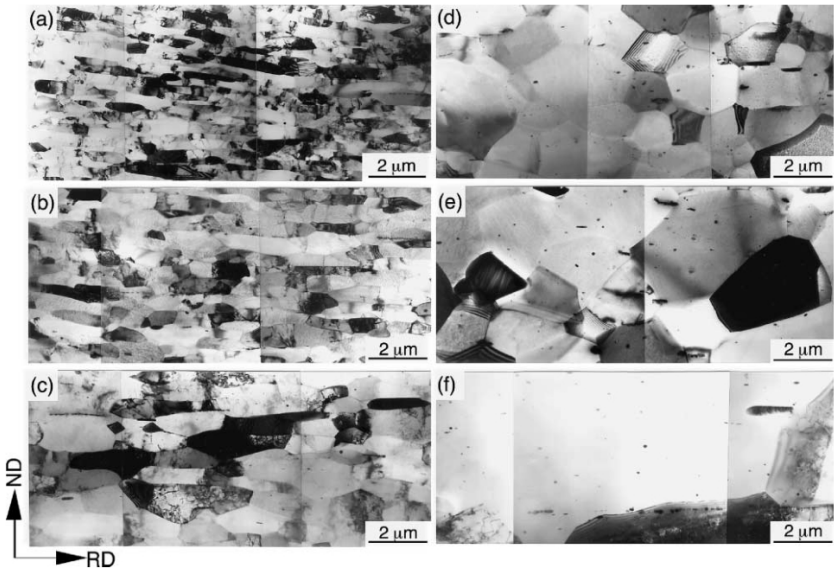

Figure 2.11: *TEM microstructures of the 1100 aluminum annealed for 1.8 ks at (a) 373 K, (b) 423 K, (c) 473 K, (d) 498 K, (e) 523 K and (f) 573 K after 6 cycles of ARB (ϵ=4.8) at 473 K. Observed from TD (Tsuji et al., 2002)*

at 473 K. The samples annealed at 373 K have a microstructure similar to the as-ARB processed sheet, although the grain size slightly increased and recovery occurred in the grain interior. The grain size increases gradually with increasing annealing temperature when the annealing temperature is above 523 K, the grains reveal an equiaxed morphology and also no dislocation substructures are seen inside. The microstructures above 523 K are close to the conventionally recrystallized material.

The effect of the annealing on the mechanical properties of ARB processed 99.2% Al is shown in Fig. 2.12.

The mechanical behavior of the as-deformed sample and annealed samples can be characterized into 4 types (Huang et al., 2009; Yu et al., 2005):

1. An as-deformed sample reaches a maximum stress at a relatively small

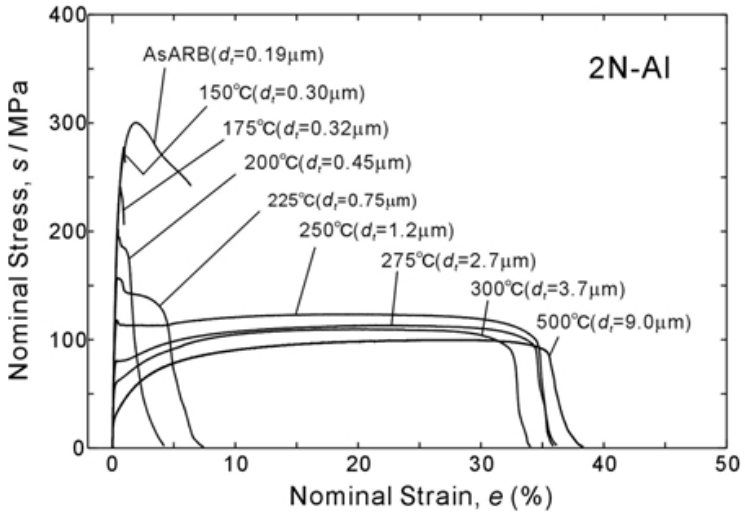

Figure 2.12: *Engineering stress-strain curves of Al1100 6-cycle ARB processed and then annealed for 30 minutes at various temperatures (Kamikawa, 2006).*

strain (1-3%) and shows a relatively large post-UTS elongation.

2. Low temperature annealed samples show enhanced localized deformation and a decrease in elongation as compared with the as-processed sample (<225°C).
3. Medium temperature (225°C) annealed samples show a yield point and Lüders band propagation where the plastic flow proceeds at nearly constant stress followed by work-hardening.
4. High temperature (≥275-500°C) annealed samples show parabolic hardening that is normally observed in coarse grained metals.

The elongation is significantly restored and at the same time the strength is still much higher than the starting material.

2.4.2 Deformation

Post-process deformation, e.g., cold rolling after ARB has also been explored by Huang et al. Several studies have been made to investigate the effect of post-process deformation on the microstructure and mechanical properties for the ARB-processed Al and IF steel. (Huang et al., 2006a, 2008a,b, 2010).

In (Huang et al., 2006a), a commercial purity Al (99.2 %) was processed by 6 cycles of ARB and it was found that an additional 15% rolling after 6 cycles of ARB increased the total elongation with a slight decrease in yield strength. More interestingly the additional cold rolling changed the necking behavior from a rapid decrease in the stress-strain curve to a nearly flat decay. This was suggested to be caused by an increase in the amount of mobile dislocations due to the post-process rolling.

In (Huang et al., 2008a,b) the same material is used but here the additional cold rolling was done to samples that were produced by 6 cycles of ARB and subsequently annealed at a low temperature. The tensile stress-strain curve of this annealed material is shown as curve 2 in Fig. 2.13. It is seen that this sample has a high strength (above 300 MPa) but a total elongation of less than 1%. By applying additional rolling up to 15% the total elongation is increased to 8% that is accompanied with a slight softening.

Increasing the post-process rolling to 50 % the total elongation decreases again (around 3.5%) but the strength is higher than the annealed material (curve 2). The mean dislocation density and lamellar boundary spacing were measured for all the conditions showing an increase in dislocation density and a decrease in lamellar boundary with increasing post-process rolling reduction. This observation supports the suggestion that introduction of a certain density of free dislocations in nanostructured metals can

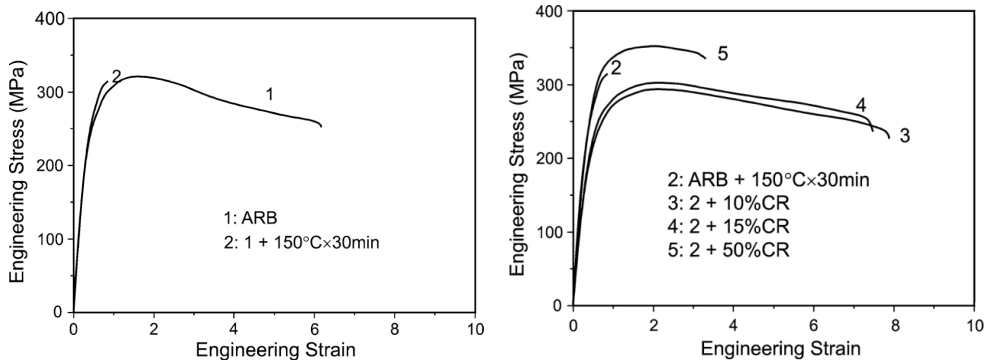

Figure 2.13: *Tensile stress-strain curves for a commercial purity Al (99.2 %) processed by 6 cycles of ARB (1) and subsequently annealed. The figure includes the samples post-process annealed at* $150^\circ C$ *for 30 minutes (2) and the three samples annealed and then cold rolled to 10, 15 and 50% thickness reduction (3-5) (Huang et al., 2008a).*

enhance the tensile elongation. However when the amount of dislocations is too large, work hardening occurs again, as seen in the 50% cold rolled sample.

In (Huang et al., 2010) the effect of post-process deformation is investigated on an interstitial free (IF) steel which has been ARB processed for 6 cycles and subsequently annealed. Here cold rolling was carried out to 0, 5, 10, 15, 30, and 50% thickness reductions to get a more detailed picture of the effect of post-process rolling (Fig. 2.14). It is seen that cold rolling from 5 to 15% has similar curves in the stress-strain plot. There is a significant increase in the elongation (from 2 to 7%) compared to the annealed sample. The 30% cold rolled sample has a slightly increased strength but keeps the total elongations of about 7% while 50% rolling reduction increases the strength more significant but decreases the total elongation to around 4%. These observations are in agreement with that for Al (Fig. 2.13) and more clearly show that an optimum cold rolling reduction can be established.

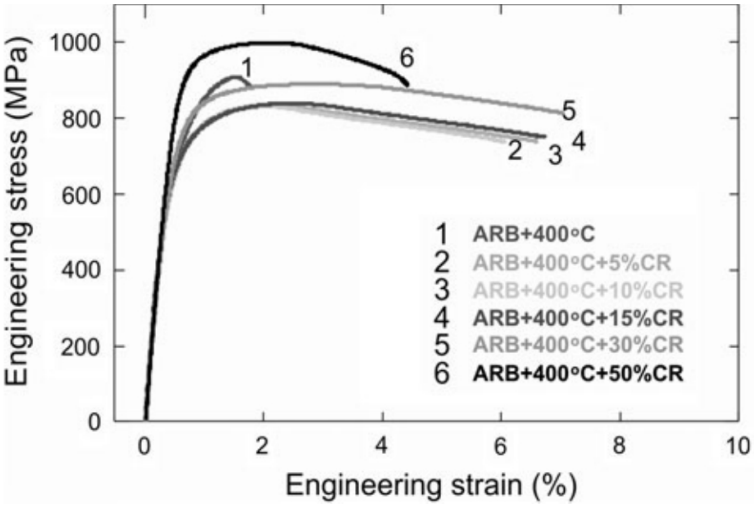

Figure 2.14: *Engineering stress-strain curves for a nanostructured IF steel. Curve 1: processed by 6-cycle ARB and annealed at* $150°C$ *for 30 minutes. Curve 2: same material as 1, plus 5% cold rolling. Curve 3: same material as 1, plus 10% cold rolling. Curve 4: same material as 1, plus 15% cold rolling. Curve 5: same material as 1, plus 30% cold rolling. Curve 6: same material as 1, plus 50% cold rolling (Huang et al., 2010).*

2.5 Formability of nanometals

As mentioned earlier a lot of work has gone into characterizing the strength and elongation of nanometals even though nanometals show poor elongation in uniaxial tension. Several attempts have been made to enhance this low elongation often by changing the strain rate or as described above by post-process annealing or by post-process deformation. However, most metal forming operations are performed in multiaxial modes but not in uniaxial tension. So far only limited studies have been conducted on the formability of nanostructured metals (Merklein and Vogt, 2009; Molotnikov et al., 2012; Ma et al., 2009; Moreno-Valle et al., 2012; Höppel et al., 2008a; Yoda et al., 2011; Höppel et al., 2008b; Hausöl et al., 2012). In doing formability tests of nanostructured metals a major difficulty has been the limited size of

samples. This issue has been dealt with in two ways. One is to increase sample sizes. The other is to miniaturize test equipments (Molotnikov et al., 2012; Ma et al., 2009; Moreno-Valle et al., 2012; Yoda et al., 2011). The first way by increasing sample sizes has been achieved by joining two test pieces by friction stir welding (Höppel et al., 2008b) or post-process cross rolling to increase sample width (Höppel et al., 2008a). The second way by miniaturizing equipment has been explored for miniaturized versions of an Erichsen test. Fig. 2.15 shows a sketch of an Erichsen test.

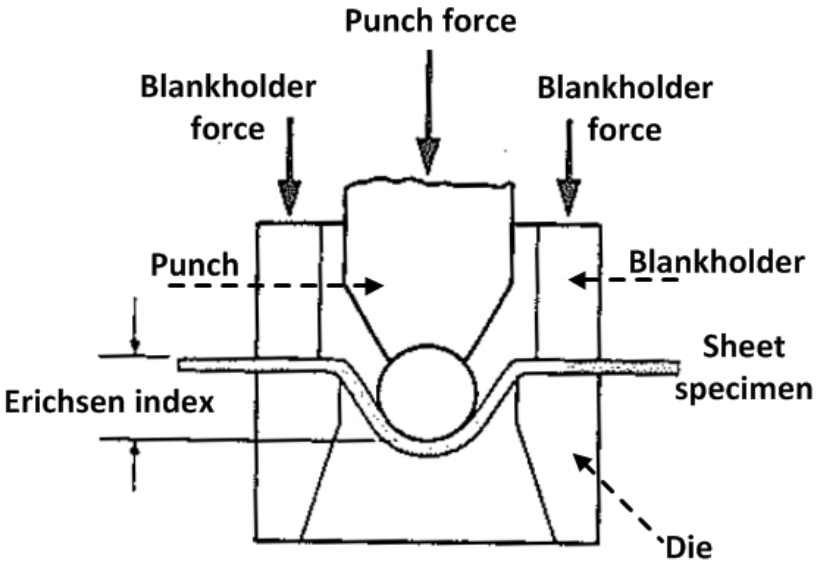

Figure 2.15: *Sketch of an Erichsen test.*

In the Erichsen test the punch is spherical and the sample is clamped between the blankholder and the die. The punched is moved until fracture is initiated and the punch movement is named the Erichsen index or Erichsen value which describes the sheets ability to be formed in biaxial stretching. For a more detailed description of the Erichsen test, which is used in the present study, see Section 4.2.1.

In (Yoda et al., 2011) an ultra-low carbon IF steel was tested in a miniaturized Erichsen test and the Erichsen Index (EI), also named Erichsen value (see Fig. 2.15) was plotted versus the average grain size which can be seen in Fig. 2.16. The starting material has a grain size of 16 μm and has an Erichsen index of 5.6 mm while the 7 cycles of ARB processed material has an EI of 3.7 mm. Comparing this difference to the difference in uniform (27% and 1-2%) or total elongation which for the starting material is over 58% and the ARB processed is 3% the ARB processed materials performs better in biaxial stretching than in uniaxial tension.

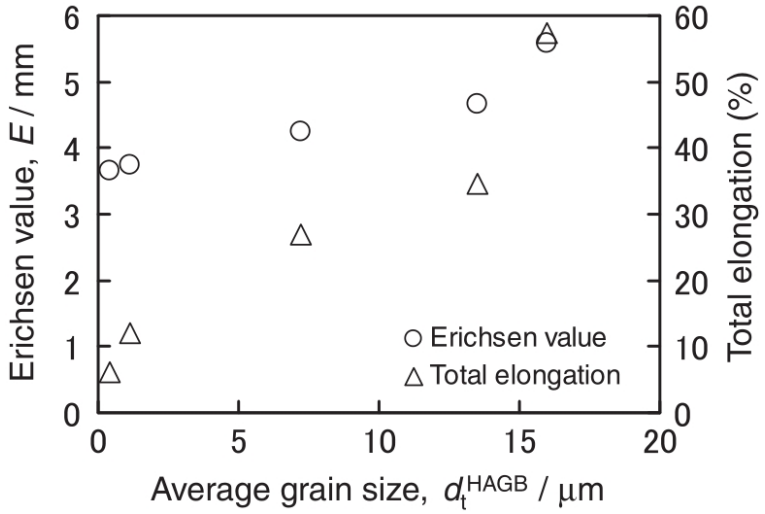

Figure 2.16: *Relationship between grain size and Erichsen value or total elongation of the specimens with various mean grain sizes fabricated by ARB processing for seven cycles with lubrication and annealing at various temperatures for 0.5 or 20 h (Yoda et al., 2011)*

In (Höppel et al., 2008a) they look at the burst pressure and pole height (Erichsen Index) of samples processed by zero to 8 ARB cycles. They show that the burst pressure saturates after two cycles of ARB while the pole height saturates after four. They also show that both burst pressure and pole height are higher for the ARB processed materials than the as-received

deformed material thereby indicating an improved formability of the ARB processed materials compared with the as-received. Similar results have been reported by (Moreno-Valle et al., 2012) indicating that nanostructured metals perform better in these miniaturized versions of biaxial tension than uniaxial tension.

2.6 Objective and overview of the thesis

The objective of the present study is fourthfold. In order to introduce nanostructured metals in industry they have to be well documented so that all mechanical parameters and suitable material models for finite element analysis are available. To obtain trustworthy material parameters it is essential to produce samples with dimensions that are sufficiently large to be tested in standard equipment. The first objective is therefore to optimize the processing of the selected commercially pure aluminium to produce nanostructured metal sheets of a suitable size. The second objective is to investigate the effect of applying post-process treatments in the form of thermal annealing and deformation on the structure and overall tensile properties of the sheets to identify processing conditions leading to a promising balance of strength and elongation. The third objective is a detailed experimental characterization of strain localization during tension, including detection of the onset of localization and the subsequent evolution of the strain heterogeneity. Finally, as the fourth objective, the performance of selected sheets is investigated by means of two typical standard formability tests. The first objective of scaling-up the sample size is pursued in Chapter 3. Chapters 5 and 6 address the second and third objectives to characterize the structure and mechanical properties of the sheets produced by ARB (Ch. 5) and of

the post-processed sheets (Ch. 6). Chapter 7 presents the evaluation of the formability of the sheets (fourth objective).

The thesis is structured as follows: Chapter 3 presents the material and optimization of the ARB technique used in the present study. Nanostructured aluminium of a commercial purity was chosen in view of its possible application in the industry and the ability to produce large nanostructured sheets in good quality. ARB processing was chosen due to its potential of being scaled-up in size which is necessary to obtain the required sample sizes. A saturation was observed in hardness and UTS after 6 cycles of ARB. Therefore this was the number of cycles used in this study. To optimize the mechanical properties post-process treatments by annealing and cold rolling were chosen based on previous studies. Chapter 4 introduces the mechanical, formability and microstructural characterization techniques employed in this study. In particular the ARAMIS system which is a digital image correlation system that is used to measure the onset and evolution of strain during a tensile test is presented and data analysis in ARAMIS is also explained. Chapter 5 characterizes the microstructure of the as-processed sheet by measuring the key parameters such as boundary spacing, dislocation density and misorientation angle distribution. The texture is analyzed by pole figures, EBSD maps and the fraction of the dominant shear and rolling components. The mechanical strength, elongation and in-plane anisotropy are extracted from tensile tests. By means of ARAMIS the onset of localized deformation and the necking behavior of the sample are characterized in detail. Chapter 6 reports the effects of post-process treatments on the microstructure and mechanical properties. The studies of the annealed sample will focus on the observation of Lüders band formation

and propagation and removal of this, while the focus for the post-process deformed sample will be on the tensile behavior. Chapter 7 investigates the formability of the sheets produced both with bulge and Erichsen tests. Chapter 8 gives conclusions and outlook.

Chapter 3

Material and processing

3.1 Starting material

A fully recrystallized 1050 Al (state O) which is 99.5% pure and has an average grain size of 30 μm was used as a starting material. The as-received coarse grain (CG1050) sheet has a thickness of 1 mm.

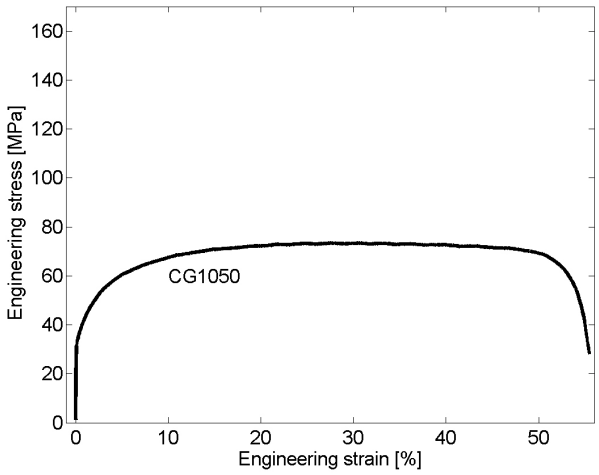

Figure 3.1: *Engineering stress-strain curve of the starting material CG1050.*

Fig. 3.1 shows a stress-strain curve for the starting material CG1050,

showing a typical behavior of a coarse grained fcc metal, namely a low yield strength (0.2% offset), large uniform and total elongation, and continuous work-hardening. The elastic region for these samples is very small due to the very limited strength. Therefore it is practically not possible to measure the Young's modulus (E) for these samples without a large scatter. Since the present study does not include any comparison of the E-modulus it was not measured and the theoretical E-modulus (70 GPa) for aluminium is used out of consistency. Comparing the theoretical E-modulus and the tensile curves shows that the slope is consistent and validates that the theoretical E-modulus can be used to estimate the 0.2% offset. From the nominal stress-strain curve for all samples tensile tested the yield stress, the ultimate tensile strength (UTS), uniform elongation and total elongation were determined. The yield stress is 39 MPa and the UTS is 75 MPa. Only a small and insignificant variation in the strength was observed in the 5 samples tested while a total elongation between 35 and 50% was observed.

3.2 Optimization of ARB processing

Sheets of the starting material 1 mm in thickness were prepared for ARB processing. The principle of ARB processing was described in Section 2.2.1. In the present study, great efforts were made to optimize the ARB processing so as to scale-up the capability of producing sheets with large dimensions and of good quality.

A two-high mill with rollers 340 mm in diameter was used for the roll-bonding and the rolling speed was set to 2 m/minute. The roll-bonding was carried out under dry surface conditions (non-lubricated). The ra-

tio between the contact length and the specimen thickness was 8.7, which ensured good bonding but caused shear generation (described in Section 3.4.2). Nearly all the deformation energy is converted into heat and to avoid recovery the roll-bonded sheet was therefore immediately cooled in cold water. In this study, 6 cycle ARB processing was performed, generating a total thickness reduction of 98.4% of the original sheet or a total equivalent strain of 4.8. The rolling direction (RD) of the sheet was maintained in between the ARB cycles but the sheet was turned from top to bottom after each pass.

Two processing parameters, wire brushing and stacking have been carefully improved to ensure better bonding and thereby better sheets. The importance of the wire brushing is illustrated in Fig. 3.2 (Jamaati and Toroghinejad, 2011). An oxidation layer on the sheet surface constitutes the contaminant film. During roll bonding this oxidation layer cracks exposing virgin aluminium at the surface of the sample. When this virgin aluminium from both sides of the bonding achieves contact a weld between them is made.

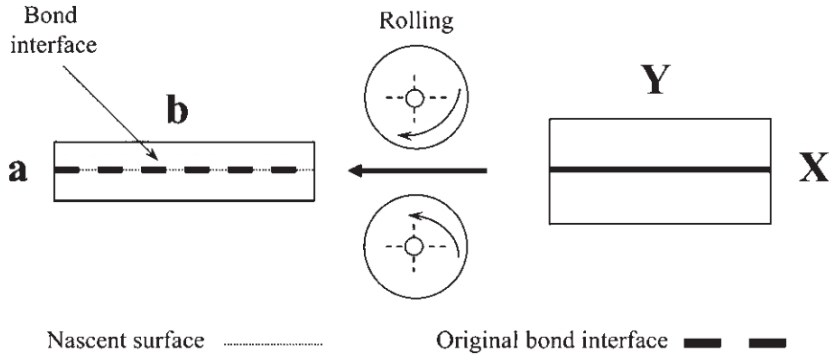

Figure 3.2: *The principle behind roll bonding (Jamaati and Toroghinejad, 2011)*

Bay (1979, 2010) showed that the best results with this weld was observed when the samples were wire-brused less than 10 minutes before the roll bonding.

It was very important to stack the two sheets with the sheet edges well-aligned. To achieve the perfect alignment, 4 holes were drilled at the corners of the stacked sheets and tightly fixed the sheets with stainless steel wire. This could reduce edge cracking and minimize trimming in between ARB cycles.

3.2.1 Edge cracking

Along the edges of the sheet, small cracks form during the ARB processing. Fig. 3.3 shows an example of this. The edge cracking may also increase because of the turning of the sheets to reduce the banana shape. To remove the edge cracks the sheets were trimmed by cutting between each ARB cycle, leading to a reduction in the final width of the ARB sheet. It was also observed that there was a thinning right at the edges of the sheets which was also removed by the trimming. Between zero and 15 mm was removed after each pass however often only a few millimeters was trimmed away.

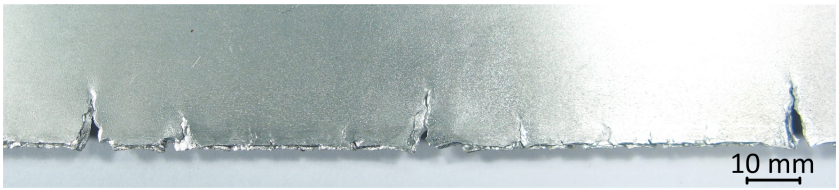

Figure 3.3: *Edge cracking on a 6 cycle ARB sheet.*

3.3 Scaling up of sample dimensions

The ARB sheets seen in the literature (often less than 100 mm in width) may be large compared to nanostructured samples produced by other SPD methods but they were still too small to carry out formability tests using standard methods. In this study an industrial test method, a bulge test, is used where the maximum sheet width required was 180 mm (see Section 4.2.2 for details). Therefore the sample width has to be 180 mm or wider. This is done by increasing the starting width to 193-195 mm. This width was very close to the capacity for processing this aluminium grade using the laboratory rolling mill (see Section 3.2). Some of the samples with a width of 195 mm got stuck half way through the rolling mill. Therefore most of the final wide sheets had a starting width of 193 mm. After 6 cycles of ARB and trimming in between the final width lies between 184 to 190 mm. Not being able to use the edges of the sheet due to the thickness issue a final width of 180 mm had to be accepted with only a small trim of the edges. In this case this was not a problem because the sides were not deformed but only clamped by the equipment. This will also be described in more detail in Section 4.2.2.

3.3.1 Homogeneity of the sheet

To investigate the homogeneity of the 6C-ARB processed sheet thickness measurements have been done along the sheet length and width. The measurements have been done every 10 mm along both directions in the center of the sheet. Not taking the thickness variation of the edges into account there was only ± 0.01 mm from the mean value which was believed to be insignificant. In the width direction hardness measurements were also done

twice to improve statistics. The mean value of 46.5 kgf/mm^2 and a standard deviation of ± 0.56 was found which is also believed to be an insignificant variation. It was therefore concluded that the sheet is nearly mechanically homogenous in the plane if the edges were not taken into account. During the present study a total of 17 ARB sheets with the previous described dimensions were produced. There can be significant variation of the mechanical strength between the ARB processed sheets. UTS values between between 154 and 187 MPa have been observed and the mechanical properties of a specific sheet will be shown in Section 5.3. The uniform elongation is nearly constant at 1.7% ± 0.1 while the total elongation measured as the total elongation of the extensometer varies between 6 and 8%. Early in the study new raw material was purchased. This can explain why there is quite a large variation in strength. The tensile results shown in Chapter 5 and Chapter 6 came from the same initial starting material sheet while the ARAMIS study (Chapter 5 and Chapter 6) and the formability test (Chapter 7) came from another initial starting material sheet. After ARB processing the entire sheet was machined for the desired purpose and the specimens were stored at room temperature which can result in recovery (Yu et al., 2011) which could also explain some of the variation in strength. To remove the variation in strength from sheet to sheet due to ARB processing the specimens for a certain test were machined from a single sheet so that the mechanical response can be compared.

3.4 Post-process treatments

Post-process treatments by annealing and by deformation were explored. The specimens for a defined post-process experiment are taken from a single

ARB processed sheet.

3.4.1 Annealing

The dimensions of specimens for tensile testing and blanks for formability testing were very different and therefore they were annealed in two different furnaces. It has been verified by annealing of tensile specimens in both ovens that the mechanical stress-strain response is the same. Three different annealing temperatures were chosen which were:

- 175°C
- 200°C
- 225°C

All samples were annealed for 30 minutes after the furnace was closed. Three tensile specimens were annealed at each temperature.

3.4.2 Deformation

The post-process deformation was done by cold rolling. The amount of rolling per pass was controlled by the l/h index which is defined as follows (Truszkowski et al., 1982):

$$l/h = \frac{2\sqrt{r(d_0 - d)}}{(d_0 + d)} \tag{3.1}$$

where r is the radius of the roller, d_0 and d are the initial and final thickness of the sheet, respectively, and h is the mean thickness given by $h = (d_0 + d)/2$.

l/h index values between 0.5 and 5 are required to achieve homogeneous rolling (Mishin et al., 2004). Therefore in the present study all post-ARB deformation was carried out under the condition of a l/h index of 2-3 to

ensure good through thickness homogeneity. In the present study four post-process rolling reductions, 5%, 15%, 30% and 50%, were investigated.
The rolling of the tensile specimens was done on a rolling mill with a diameter of 74.5 mm and the blanks were rolled on the same rolling mill used for the ARB processing.

The post-process rolling of specimens that are required to deform to different reductions was carried out in one rolling experiment. For the tensile specimens two dummy specimens were used to position the rolls before each rolling pass to ensure that the l/h ratio was kept between 2-3. All samples were first rolled 5%. Then three samples were taken from the batch for future tensile testing and the rest of the samples were further rolled to a thickness reduction of 15%. Then again three samples were taken from the batch and the rest were further rolled to a higher reduction and so on. Each post-processing rolling experiments were completed with three samples at each of the 4 chosen rolling reductions. It was noted that the tensile specimens after 15% post-process rolling were S-shaped. This S-shape was straightened with further rolling and was therefore not seen in the 30% and 50% reductions. Therefore the 15% post-process rolling was repeated but the results were similar. Before tensile testing these specimens were carefully straightened.

The blanks for the formability testing were prepared in the following way: ARB sheets were post-process cold rolled right after 6 cycles ARB processing and cut into the final geometry of blanks. Also here a dummy sample was used to ensure precise rolling reductions.

Chapter 4

Mechanical and structural characterization

4.1 Mechanical testing

4.1.1 Conventional tensile tests

The mechanical properties were characterized by tensile testing. Two testing machines were used in the present study.

- Instron Electro Puls E3000 machine with a 5kN load cell
- Tytron 250 microforce testing system

The Instron machine was the one primarily used and the Tytron was only used in connection with the ARAMIS system described in Section 4.1.3. Tensile dog-bone specimens with 16 mm long and 5 mm wide gauge dimensions were machined with the tensile direction parallel to the RD of the ARB process. Fig. 4.1 shows the dimensions of the tensile specimen.

When a test series was planed all the tensile specimens were taken from a single ARB sheet, so the strength variation between ARB sheets did not

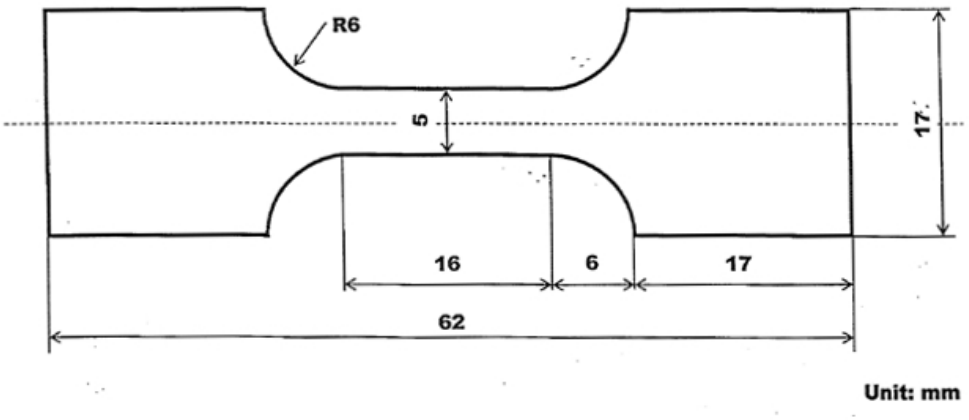

Figure 4.1: *Dimensions of the tensile specimen.*

influence the analysis of the results obtained for a given test. All tensile tests were performed at room temperature and the strain rate was controlled by the motion of the cross-head which was set to 1 mm/minute corresponding to an initial strain rate of $10^{-3}s^{-1}$. Data collection was done at 50 Hz controlled by the wave matrix software which also operates the tensile machine. Strain data were measured using an extensometer with an extension gauge of 12.5 mm and a scale range of ± 5 mm which can measure the elongation up to 40%. Some variation was observed in the elongation data due to the fraction outside or at the extensometer contact point with the sample. In both cases the data were excluded and the test was repeated. To reduce the influence of the contact point of the extensometer small pieces of double sided adhesive tape were put on the sample. Small 90° angle tools were used to align the tensile samples with the grips of the tensile machine making the tensile direction of the tensile machine and sample coincident. A vernier caliper was used to measure the initial thickness and width of each sample to convert the load measurements from the tensile machine to engineering stresses.

4.1.2 Strain rate jump tests

A variety of experimental techniques can be used to assess the thermodynamic and kinetic aspects of the plastic deformation of metals such as the strain rate sensitivity. Strain rate jump tests at a constant temperature are amongst the most widely used methods. The imposed rate of deformation of the specimen is changed by changing the speed of the cross-head of the testing system. A basic assumption in such an experiment is that the internal structure, such as the mobile dislocation density, is not changed by changing the rate of plastic deformation (Wei, 2007). The strain rate sensitivity exponent (m) can be determined by the following equation (Meyers and Chawla, 1984):

$$m = \frac{ln(\sigma_2/\sigma_1)}{ln(\dot{\epsilon}_2/\dot{\epsilon}_1)} \tag{4.1}$$

where 1 and 2 refers to the stress and strain rate before and after the change (jump) in cross-head speed. These experiments were conducted with jumps every 1% tensile strain. The jumps were between 1 and 10 mm/minute in cross head speed corresponding to an initial strain rate $10^{-3}s^{-1}$ and $10^{-2}s^{-1}$. Fig. 4.2 shows the stress-strain curve for the as ARB processed sample where clear jumps in the stress can be observed.

4.1.3 The ARAMIS system

4.1.3.1 Tensile tests

Digital Image Correlation (DIC) is an optical measurement technique to track changes in images. These experiments were done to obtain the strain distribution and evolution of the samples during tensile testing. All the

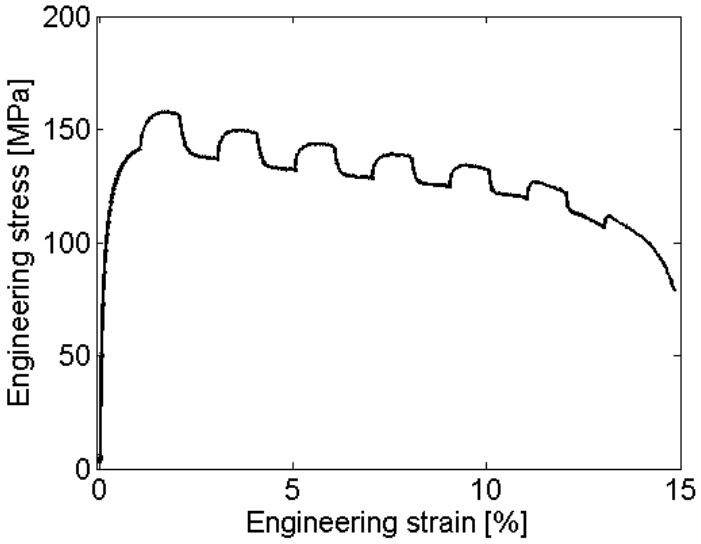

Figure 4.2: *Stress-strain curve for the as ARB processed sample for a strain rate jump test.*

samples tested with ARAMIS were also taken from a single ARB sheet which is a different sheet from that used to machine the samples tested by conventional tensile testing.

The ARAMIS software from GOM mbH was used for the tensile experiments and the principle of the setup is illustrated in Fig. 4.3.

This ARAMIS setup consists of two camera systems each with a high resolution CCD-camera and an external controller that records the force data from the tensile machine. The CCD-cameras record images of the tensile specimen at every specified time interval (Hoffmann and Vogl, 2003; Hoffmann and Hong, 2006). For this particular setup the front camera has a view of 70*90 mm^2 when the focus was at its optimum while the side camera has a view of 7*9 mm^2.

To have a contrast on the samples that the DIC system can recognize the samples were first painted matt white so that light was not reflected. Subsequently they were covered with a stochastic dot pattern which can

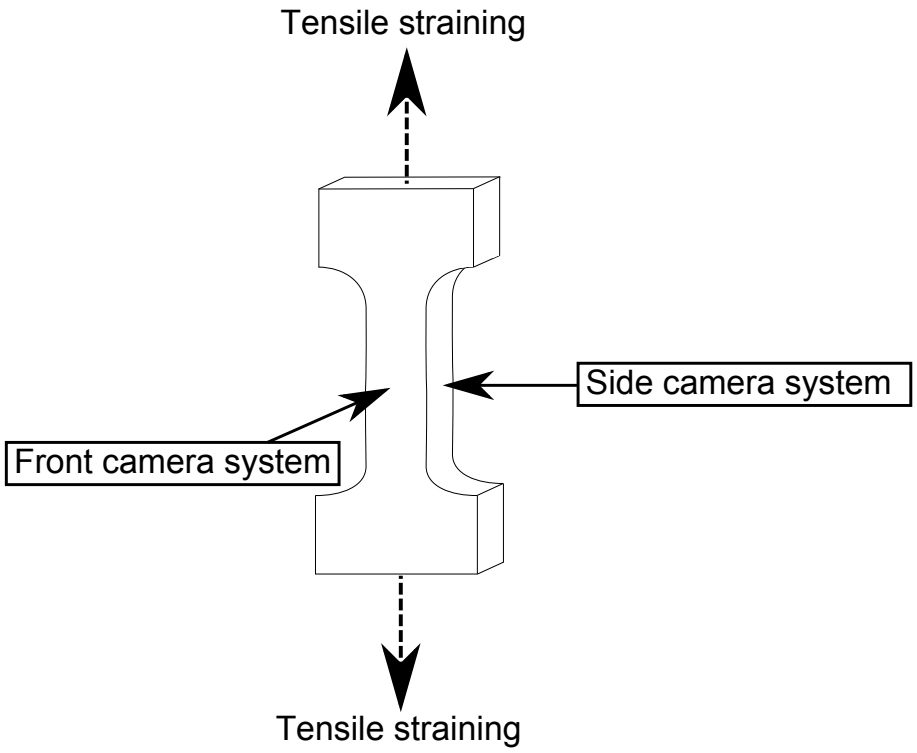

Figure 4.3: *ARAMIS setup with two high resolution CCD-cameras named front and side. Tensile straining is indicated with arrows.*

be seen in Fig. 4.4. It took several iterations to achieve a good stochastic pattern with an evenness in dot size and distribution.

The DIC system compares two images taken successively and calculates the difference in dot movement. Based on these images, the ARAMIS system can identify points on the specimen surface. The system divides the image into many small squares, called facets. The distortion of these facets is monitored throughout a test in three-dimensional space (Hogström et al., 2009).

A random pattern on the surface of the specimen was used to follow the deformation as well as the fracture behavior of the specimen material. The distortion is converted into engineering strain by dividing the change in length from the previous image with the length from the previous image.

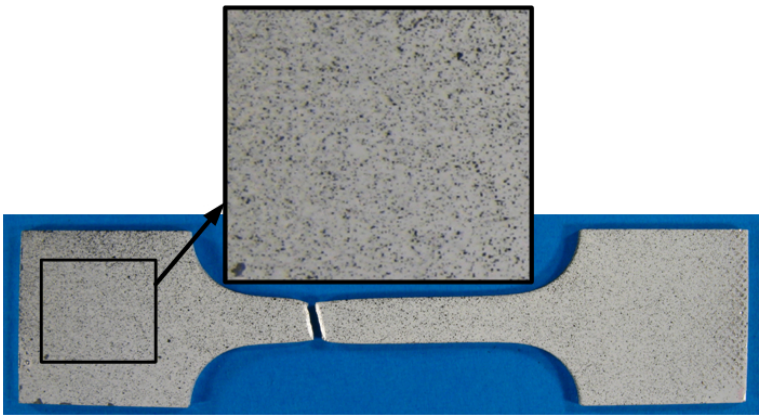

Figure 4.4: *Tensile specimen with a gauge of 16 times 5 mm. The specimen is painted matt white and subsequently covered with a stochastic dot pattern. This specimen is shown after testing so the necking and fracture can be seen.*

The manufacturer claims the accuracy of displacement measurement to be in the interval 0.01-0.1 pixels (Hogström et al., 2009) with a pixel size of 30 μm that gives a maximum error of 3 μm. An increase in the number of facets and images will increase the computation time. The facet size is user controlled and in the present study a facet size of 15 or 25 pixels is used where 15 is the software minimum.

Before testing the optical measurement system was calibrated. This was a very sensitive process which was repeated several times to achieve a high precision. The calibration was done with a special calibration plate with predefined dots so that ARAMIS could calculate and take small angles and distance deviations into account when adjusting the system. For every sample eight images were taken without any movement in the tensile machine to check if the dot pattern could be recognized by the ARAMIS system. If not the paint was chemically removed and the sample was repainted again until a good recognition was achieved. Initiating the test was done by turning on the camera system and when it was ensured that it was running

(small time delay) the tensile machine was activated. The force from the tensile machine was saved simultaneously with every image taken.

Three repetitions were done for all material conditions tested. The tensile elongation in the experiments using ARAMIS was measured by ARAMIS using the line analysis function which corresponds to an extensometer in traditional tensile test. The length of the line used to measure the tensile elongation is approximately 16 mm which is equivalent to the gauge length. Conventionally an extensometer cannot be the same size as the gauge length but in ARAMIS it was done out of consistency to make sure that the measuring distance was the same in all experiments for a better comparison between experiments. The simplest way was to measure the entire gauge length because it could be recognized relatively simply in the strain field in ARAMIS due to a color change at both ends of the gauge (see Fig. 4.5).

The frequency of the images from the camera system is user controlled and several settings have been tried to find a good correlation between total elongation (here meaning total time for the experiment) and the numbers of images required to obtain a good recognition by the ARAMIS system. Experiments with images raging from 300 to 1000 have been investigated. 1000 images are too many for this strain evolution and only resulted in a very slow computation time. No problems have been observed with only 300 images which suggests that even fewer images could be satisfactory. This has not been investigated. In all the experiments recognition failed when the distortions became too large. If a more detailed analysis of the very end of the test is of interest more investigations have to be done on

accommodating the large local strain values.

The ARAMIS system was used for two investigations. First a strain onset and evolution investigation and second an investigation to measure the anisotropy of the sheets. The first investigation only used the front camera system while the second investigation used both the front and the side camera system and is desribed later.
To verify the set-up of the ARAMIS system of the front camera, pre-tests were done for the CG1050 sample which is described in the following.

4.1.3.1.1 Tensile behavior The following subsection will analyze and compare the width contraction strains from a large region over the sample front. The width strain is measured with a line analysis, and is the total strain over the width of the sample. The results measured at several positions along the gauge length of the sample are shown in Fig. 4.5, where the local width strain is plotted as a function of the engineering tensile strain and the locations for measurements are indicated by numbered horizontal straight lines (black and red) across the sample width. The black line (line 1) marks the position that eventually ends up being the necking region, i.e. which shows the maximum strain in the final stage of the tensile test. Graphical presentations of the detailed strain distribution are shown in the figure to illustrate the position of the different lines. The tensile engineering strain corresponding to the UTS is indicated by a dotted line (marked UTS).

The CG1050 is a well-documented sample that should exhibit uniform elongation up to the UTS which can also be indentified from Fig. 3.1. As expected, there are only small (less than one percent) heterogeneities in

the strain distribution over the sample gauge length, which can be seen in Fig. 4.5(a) and in an enlarged form shown in Fig. 4.5(b) for a tensile strain of 7%. The distribution has been studied with different color scales to enhance the visibility of the small variations. The conclusion of this analysis is that the strain variations revealed on the sample front face are small and fluctuate randomly at all tensile strains up to the UTS.

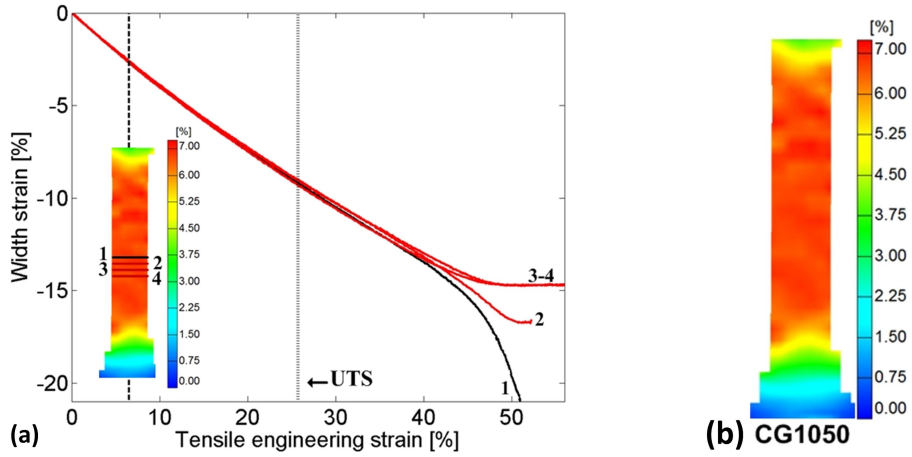

Figure 4.5: *(a) CG1050 showing homogeneous deformation, as expected, up to 40%. Variations in the strain distribution are below 1% strain. (b) Strain distribution map for a tensile strain of 7%. The CG1050 sample showing homogenous strains with local fluctuations below 1% strain.*

4.1.3.2 Anisotropy

The mechanical anisotropy can be evaluated with the same ARAMIS setup but here both the front and side camera systems were used to follow the width and thickness strains simultaneously. The idea with these experiments was to measure the anisotropy and at the same time have the possibility to construct a true stress-strain curve from the actual cross section area. The true stress-strain curve is of most interest in the post-UTS region therefore the necking behavior is important. This gave some practical

challenges due to the difference in camera view of the side and front camera systems. The previously used tensile sample had a gauge length of 16 mm. This makes it difficult to capture necking with only a 7 mm view. Therefore new tensile specimens for the anisotropy experiments was made with a gauge only being 8*4 mm which can be seen in Fig. 4.6.

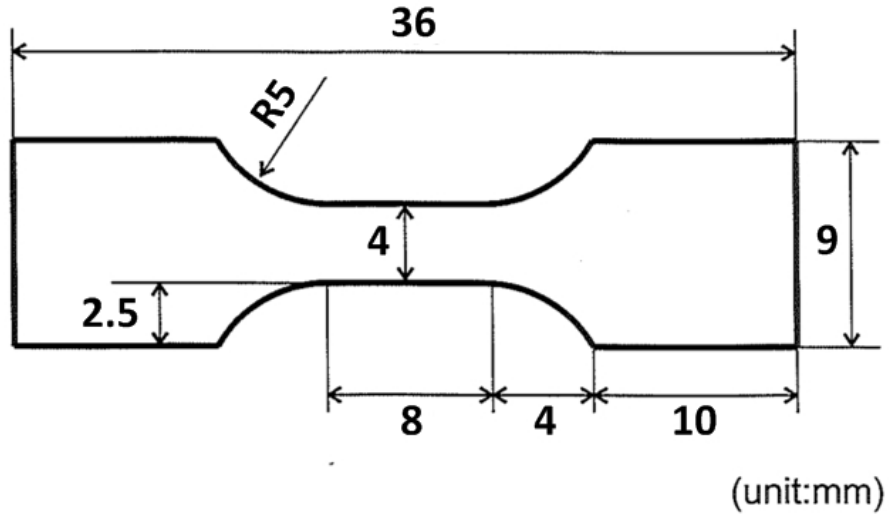

Figure 4.6: *Dimensions of the tensile specimen used for anisotropy experiments.*

Due to the smaller sample the maximum error from the front view camera system increases to 3.3 μm which is a minor detail but the small camera view from the side gives a much better maximum error of only $0.4\mu m$. However, the ARAMIS data obtained were not as good as before because of the small gauge section. This shows how important the match between sample and camera view was. It was experienced that the edge of the sample had to be disregarded in the ARAMIS analysis. One reason for this could be if a dot was placed right at the edge it could turn or rotate with even small deformations leaving rather big artificial edge strains. Therefore the facets closes to the edge could only come close to the edge but not entirely covers

the edge.

Painting the sample required some iterations for the front of the sample. Painting both the side and the front at the same time took some additionally iterations. The experiment was initiated similar to before. The front and side cameras was connected through ARAMIS so they took images at the same time.

The Lankford parameter (R) (Lankford et al., 1950) is defined as:

$$R = \frac{\epsilon_{width}}{\epsilon_{thickness}} \tag{4.2}$$

where ϵ_{width} and $\epsilon_{thickness}$ are the logarithmic width and thickness strains that are determined with the previously mentioned line analysis on the front and side camera systems of ARAMIS. The width and thickness strains were measured at 1% tensile strain for all experiments. This relatively low strain was chosen because it is in the uniform strain region of all the samples tested. The Lankford parameter is determined for tensile tests along directions 0, 45 and 90 degrees relative to the RD direction. Through them the following parameters can be calculated (Kalpakjian and Schmid, 2004):

$$R_{normal} = \frac{R_0 + 2 * R_{45} + R_{90}}{4} \tag{4.3}$$

$$\Delta R = \frac{R_0 - 2 * R_{45} + R_{90}}{2} \tag{4.4}$$

The parameter ΔR is used to quantify the planar anisotropy and R_{normal} is used later in Chapter 7 for forming limit diagrams. If R_{normal} is larger

than 1 it reduces wall thinning during forming operations. Earing in for example deep drawing is minimized if ΔR is close to zero.

4.1.4 True stress-strain curves

Measuring true stress-strain is in theory relatively simple but in practice it can be quite difficult due to the complexity of measuring the small sheet thickness. Therefore specially designed equipment is often used to test and measure for true stress-strain data. The anisotropy experiments should also have been used to construct a true stress-strain curve but due to the poor match between camera systems and samples there was quite some scatter in the results. Especially at larger strain (necking) the results were unusable therefore a simplification to minimize the scatter could be beneficial where the thickness measurements are not taken into account.

To measure the true stress-strain curve requires the actual cross section area in the necking zone. This can be very difficult to achieve due to the small thickness of the sheets in general. ARAMIS measures the two principal strains from the front camera system. These data can also calculate the strain in the thickness direction with a small simplification.

As mentioned above the ARAMIS system divides the sample into small squares called facets and calculates the horizontal and vertical (major and minor) strain of these facets. Since the facets have a small volume it is assumed that the volume constancy can be stated without any significant error. Thereby giving:

$$\epsilon_{tensile} + \epsilon_{width} + \epsilon_{thickness} = 0 \Longrightarrow \epsilon_{thickness} = -\epsilon_{tensile} - \epsilon_{width} \tag{4.5}$$

Using this equation gives all the three strain components for all facets without a direct measurement on the thickness.

Finding the true stress-strain data up to the UTS is relatively easy because it can be converted from the engineering stress-strain data under the assumption of uniform elongation (Callister and Rethwisch, 2007).

$$\sigma_T = \sigma_E * (1 + \epsilon_E) \tag{4.6}$$

$$\epsilon_T = ln(1 + \epsilon_E) \tag{4.7}$$

where T and E are for true and engineering stress and strain respectively.

These equations are quite useful if only the uniform part of the curve is of interest. In the present study where the necking region is of interest these equations fall short. Therefore the cross-sectional area must be monitored under the entire tensile test which is exactly what ARAMIS does. The cross-sectional area can be divided into width and thickness. Using Eq. 4.5 the thickness strain can be estimated. The width strain can be found with the line analysis from the front data and by knowing the initial width and thickness of the sample the actual dimension can be found through:

$$\epsilon_E = \frac{\Delta t}{t_0} \Longrightarrow t_{actual} = \epsilon_E * t_0 + t_0 \tag{4.8}$$

ARAMIS has data on all the facets on the sample but only the facets in the necking region are of interest. ARAMIS has a function that can export all the facets over an user input line; thereby achieving only the strain values for the necking region. In the present experiments there were 7 facets over the width of the sample. Taking the mean of these thickness strains and using Eq. 4.8 gives a good approximation of the actual thickness of the

sample. Fig. 4.7 shows the evolution of the actual thickness and width dimensions during the tensile test.

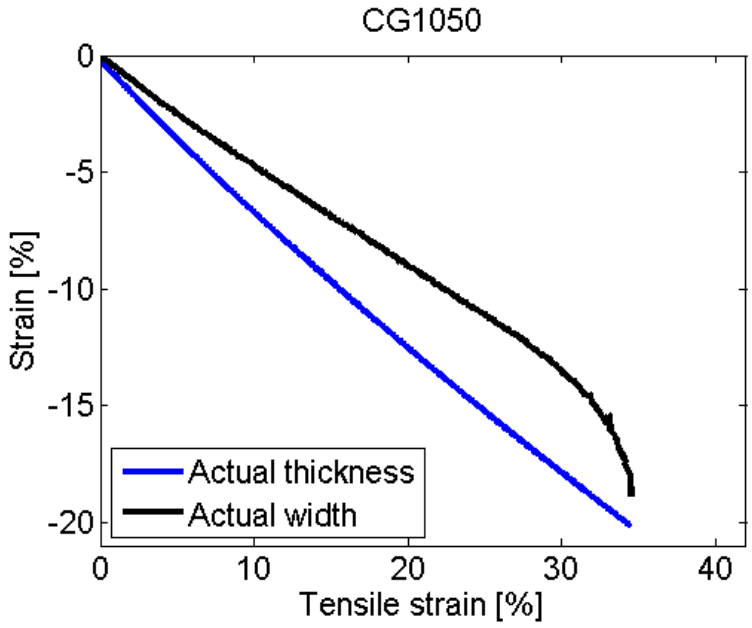

Figure 4.7: *The evolution of the actual thickness and width dimensions during the tensile test.*

Having both the actual width and thickness of the sample the true stress-strain data can be found and an example for CG1050 is shown in Fig. 4.8.

The blue curve is the engineering stress-strain curve while the black curve is the converted true stress-strain curve from Eq. 4.6 and Eq. 4.7. The red curve is the ones found through the actual cross-sectional area from ARAMIS. The CG1050 is a well studied sample and therefore the converted true stress-strain curve was extended beyond UTS because the decay after the UTS is more or less flat so there is no rapid necking behavior before the end of the test which was also found by studying the ARAMIS data of the post necking region. The black and red curves coincide up to around 15% strain. After that a difference develops with increasing strain. This

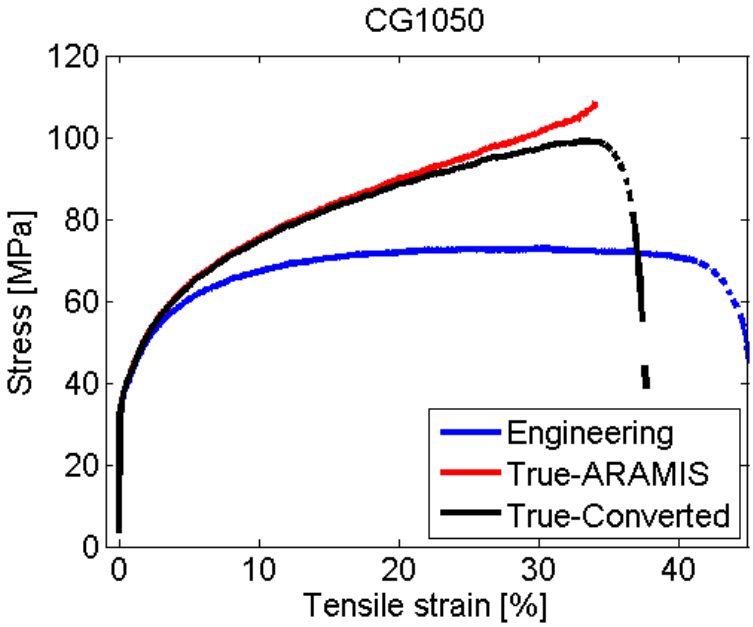

Figure 4.8: *Stress-strain curves for one CG1050 sample. The blue is the engineering curve with the strains found with line analysis in ARAMIS. The black curve is the converted true stress-strain curve converted through Eq. 4.6 and Eq. 4.7. The red curve is the true stress-strain curve found by using the actual areal from ARAMIS.*

is believed to be caused by small measurement errors that probably could be avoided if the match between camera view and tensile sample had been better. The red line ends around 35% because the width strain no longer can be recognized by ARAMIS due to a large distortion in the stochastic dot pattern on the sample.

4.2 Formability testing

4.2.1 Erichsen test

The Erichsen test is a standard cupping test to evaluate the formability of a sheet in balanced biaxial stretching (ISO20482). In the present study

a Roell and Korthaus BP612 machine was used. The Erichsen tests were done in two batches which will be described later. In the first batch all the blanks came from the same initial ARB sheet while in the second batch the blanks came from different sheets but the ARB processing of these sheets were done together to mimimize mechanical variations. In the Erichsen test a square blank of 55 by 55 mm is clamped in between the die and blankholder with a force of 10 [kN]. A sketch of the Erichsen test setup is shown in Fig. 4.9. The punch has a diameter of 20 mm and die with a diameter of 27 mm. The blank is lubricated with a thick lubricant to reduce the dependency of friction between the blank and the punch which can be a disadvantage of the Erichsen test.

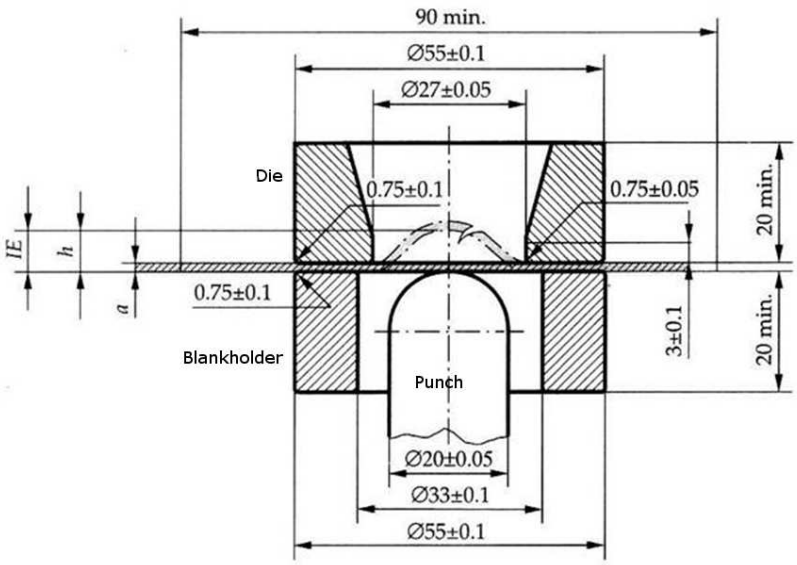

Key:

a = Thickness of the test piece
h = Depth of the indentation during the test
IE = Erichsen cupping index

Figure 4.9: *A sketch showing the dimensions in the Erichsen test (ISO 20482)*

The blanks were manually placed over the die and the test was started. After the force in the blankholder is achieved the punch will move upward at an user controlled speed. In the present study the punch had a speed of 5 mm/minute. When the punch reaches the blank the punch force will increase and the deformation of the blank will begin. The maximum force was recorded by the machine. The maximum force occurs just before necking. As the deformation of the blank increases, the blank will deform in the shape of the punch leaving a buckle in the blank. Just before the punch causes fracture in the blank seen by a necking zone (visually observed), the test was stopped manually. The height of the buckle or punch movement was measured which is called the Erichsen Index (EI) with a unit of mm.

4.2.2 Bulge test

To measure more of the in-plane mechanical properties, bulge tests were performed. The blanks were individually placed in a BCS-30 universal sheet forming property testing machine with a 100 mm punch and a die with a diameter of 103 mm. The press operated in the same manner as described in Section 4.2.1 for the Erichsen test. The blank was clamped in-between the die and blank holder before the punch was set into motion. The diameter of the blank holder was 133 mm. The blank holder force was varied from 30 to 70 kN with increasing blank width. The punch had a speed of 10 mm/minutes and the punch force was monitored during the test. The punch was stopped when a rapidly decreased force by 500 N (indicating fracture) occurs. The die and blank had draw beads that deform the flange of the blank when the blank holder force was high enough and thereby reducing the blank flow resulting in a near pure stretching operation. The flange deformation is illustrated in Fig. 4.10(a).

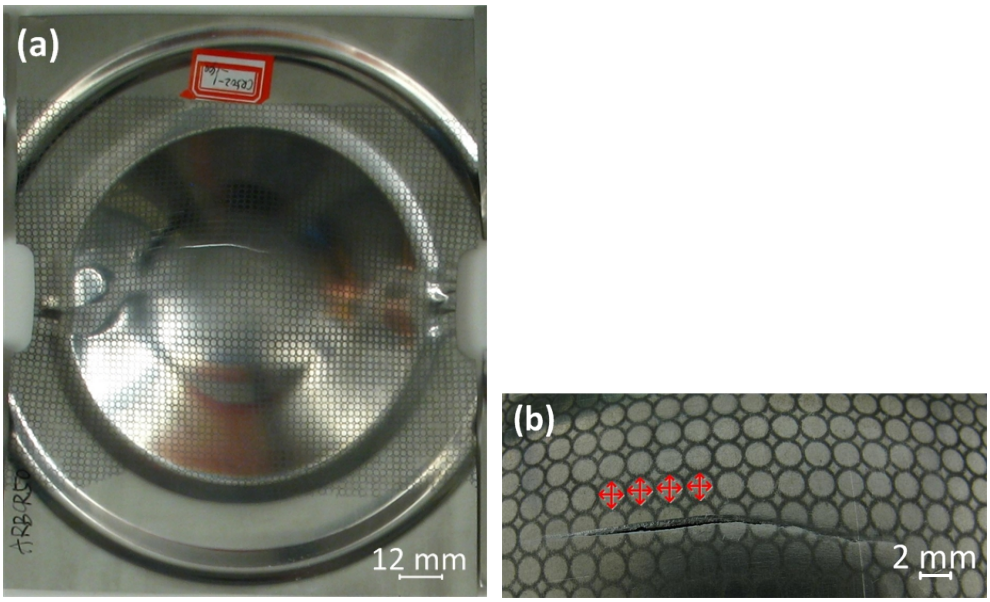

Figure 4.10: *(a) The 160 mm wide sample where the final deformation can be seen after testing both from the punch and the draw beads (b) A zoom of the same sample around the fracture. The 2 mm circle grid can be seen for strain measurement the circles that have a crack inside are not used but the circles next to them were used to determine the major and minor strains, as indicated with red arrows.*

By varying the specimen width, the lateral constraint (i.e., the amount of material allowed to draw into the die cavity in the width direction) can be varied to achieve failure in modes ranging from nearly uniaxial tension through plane strain to balanced biaxial tension (Raghavan, 1995). Therefore specimens with a fixed length of 176 mm and different widths of 20, 40, 60, 80, 90, 100, 120, 140 to 160 mm were cut. Fig. 4.11 shows the sample geometry. The samples were cut into squares and spark cut into the final shape. Additionally a square of 180 by 180 mm was also tested. Due to the larger size the samples came from 3 different ARB sheets but the ARB processing was done together to minimize mechanical variations.

The length direction of the specimens and the rolling direction in the ARB process were kept the same as given in the standard (ISO/DIS12004-

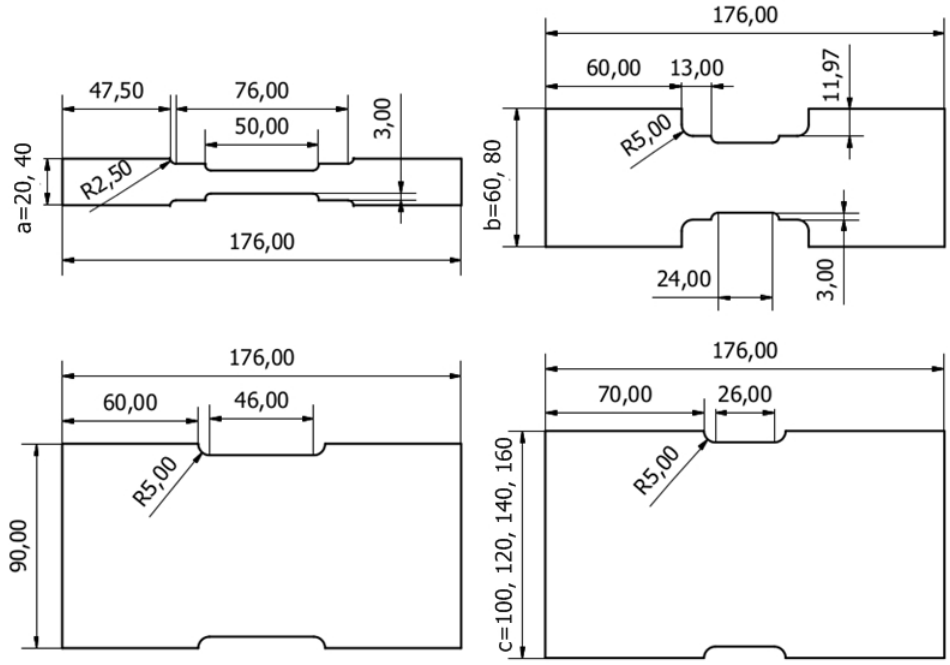

Figure 4.11: *Sample geometry for the bulging test from the technical manual of the BCS-30 sheet forming universal test machine*

2). To reduce friction between the blank and punch, a low density polyethylene (LDPE) film with a thickness of 0.04 mm was placed on the blank before testing.

4.2.2.1 Strain measurement

On the sample surface a 2 mm circle grid was made by chemical etching with a KCl(80g) + $NaCl$(90g) + HCl(100ml) + H_2NO_3(100ml) + H_2O(4.5l) solution. After the test a CCD camera measures the distortion due to deformation of the circular grids on the sample after the test was finished. The vertical and horizontal distortions were measured and converted into major and minor strain respectively. As seen in Fig. 4.10(b) the circles that have a crack inside were not chosen but the circles behind them were, as indicated

with red arrows. Three to five circles were measured on each sample and the mean of there values was plotted in the forming limit diagram.

4.2.2.2 Forming limit diagram

The forming limit diagram (FLD) was derived by (Keeler, 1968; Goodwin, 1968). The FLD defines the maximum allowable strain levels during sheet metal forming and one example can be seen in Fig. 4.12. These diagrams show the magnitude of the major strain before the onset of a localized neck as a function of the minor strain in the sheet surface. Usually, strain paths during one step forming operations are nearly proportional, i.e. they maintain a nearly constant ratio of major to minor strain (Laukonis and Ghosh, 1978).

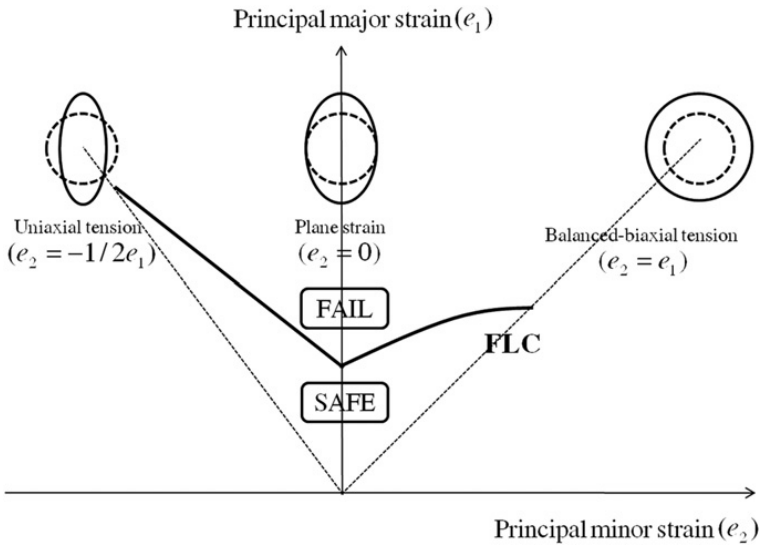

Figure 4.12: *Sketch of a forming limit diagram (FLD). The forming limit curve (FLC) separates the safe region from the failed region. The three special cases uniaxial tension, plane strain and balanced-biaxial tension can be identified by the deformation of the circle grid (Jong Bong et al., 2012).*

In Fig. 4.12 the circle grid from Section 4.2.2.1 can be seen before and after deformation revealing the areas of uniaxial tension, plane strain and

balanced biaxial tension. The forming limit curve (FLC) can also be seen in the figure dividing the FLD into a safe and fail region.

4.3 Microstructural investigation

The microstructural characterization was carried out by transmission electron microscopy (TEM) and electron backscatter diffraction (EBSD). The longitudinal section that contained the normal direction (ND) and the RD of the deformed sheet was selected as the observation plane, as it is the best section to reveal the detailed microstructural features for rolled samples (Winther et al., 2004).

4.3.1 Electron backscatter diffraction (EBSD)

Scanning electron microscopy (SEM), which images by scanning with a high energy electron beam, is one of the most commonly used methods to observe materials. Compared to light optical microscopy (LOM), SEM has a much higher spatial resolution which is around 100 times better. Several signals are generated when the electron beam hits and interacts the surface of the sample. Two commonly used signals are the secondary electrons (SE) that through contrast primarily reveals the sample topography and backscattered electrons (BSE) of which contrast strongly depends on the atomic number and the crystallographic orientation of the sample. In the last two decades electron backscattered diffraction (EBSD) has matured into a frequently used method to study structural evolution of crystalline materials. A schematic diagram of a typical EBSD installation is shown in Fig. 4.13.

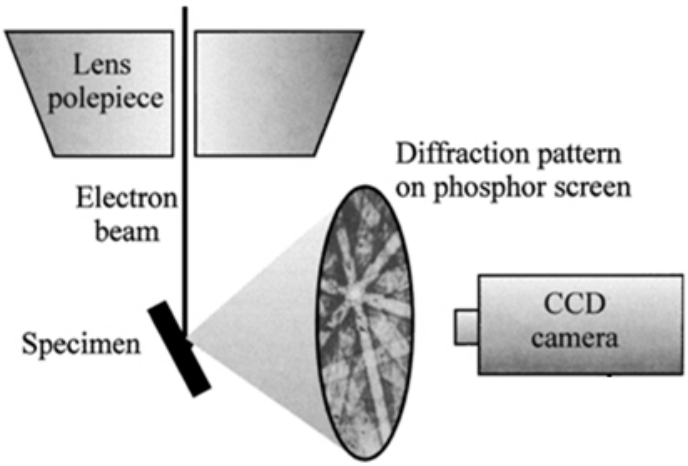

Figure 4.13: *A schematic diagram of a typical EBSD installation, where the specimens is typically* 70° *tilted (Yu et al., 2011).*

The electron beam hits a titled crystalline sample, generating a Kikuchi diffration pattern, which is fully automatized by a computer to determine the crystallographic orientation of the scanned point (Yu et al., 2011). In EBSD the spatial and angular resolution can be down to 20 nm and 1° respectively (Humphreys, 2004).

A Zeiss Supra-35 FEG scanning electron microscope, equipped with an HKL Channel 5 EBSD system, was used in the present study. The microscope was operated at 15 kV. Samples for EBSD analysis were mechanically polished followed by electropolishing in a solution of ethanol (70%), water (12%), 2-butoxy-ethanol (10%), and perchloric acid (8%) at about 2°C for 45 seconds. The scans were made through the thickness of the sample times approximately 1 mm using a step size of 5 μm to determined the texture of the sample. The scan was started in the top-right corner stepping downwards one column at a time. The 45° rotated cube, copper, brass and S texture components were considered in the present study, and the texture

components were defined using a maximum 15° deviation from the ideal orientation. All orientations beyond the 15° deviation to these components were grouped as other texture components.

4.3.1.1 Texture of CG1050

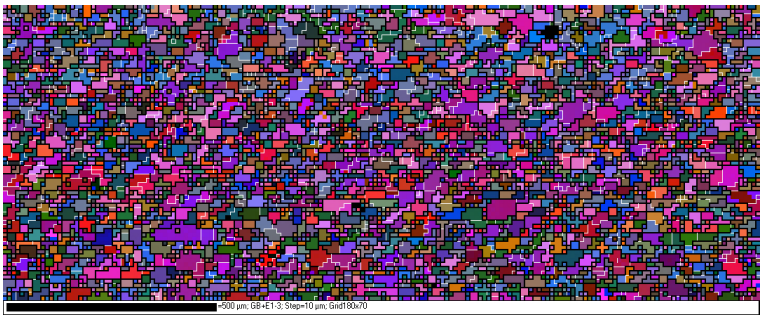

Figure 4.14: *EBSD map of the coarse grained starting material.*

Fig. 4.14 shows that the texture of the CG1050 sample is homogeneous through the thickness of the sample. Table 4.1 shows the fraction of the dominant rolling texture components (Brass, Copper and S) and cube texture (Cube). These texture components are illustrated in the principle {111} pole figure shown in Fig. 4.15. Comparing Fig. 4.15 with Fig. 4.16 shows a clear rolling and Cube texture dominated by S and Cube which is also confirmed in Table 4.1.

Additionally the 45° ND rotated cube component (45ND RTCube) was added in Table 4.1 to make a later comparison even though the amount of 45ND RTCube is limited.

Table 4.1: Dominant texture components for the coarse grained starting material.

Components	Other	Cube	Brass	Copper	S	45ND RTCube
CG1050	34.54%	20.19%	4.02%	9.96%	31.26%	0.13%

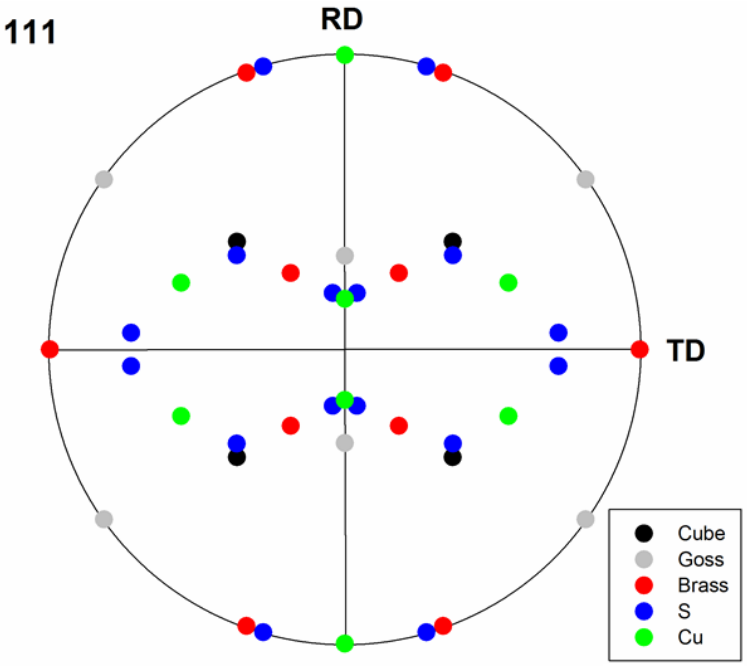

Figure 4.15: *Principle* {111} *pole figure showing the different texture components.*

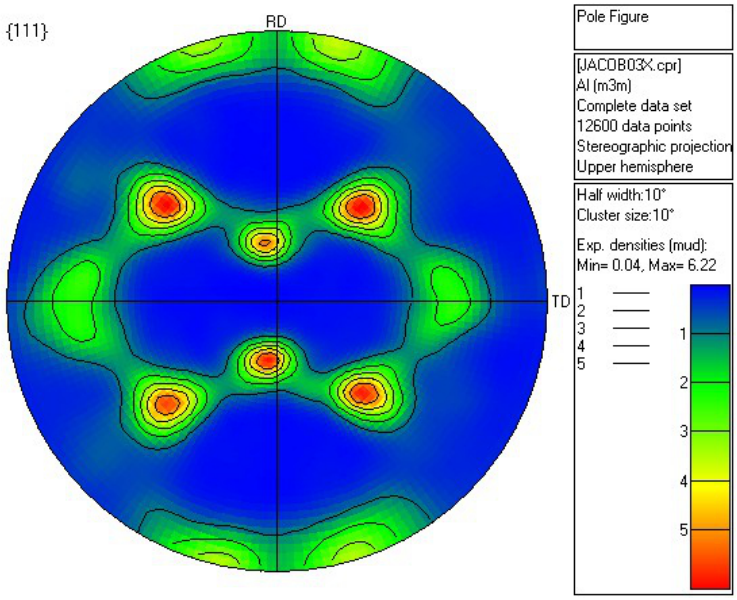

Figure 4.16: {111} *Pole figure for the coarse grained starting material.*

4.3.2 Transmission electron microscopy (TEM)

Compared with SEM, transmission electron microscopy (TEM) has an even higher resolution, which can be below 0.1 nm for the best instruments. The transmission electron microscope is versatile, producing a number of different signals which can be used for various operation modes. For example, it can be operated in an imaging mode where it can produce both a bright field image and a dark field image. Similarly it can be operated in diffraction mode used for generating a Kikuchi diffration pattern. Thin TEM foils were prepared by electropolishing typically 0.1-0.5 μm in thickness and with a large area of around 400 μm^2. The examinations were made with a JEOL 2000FX electron microscope operating at 200 kV. Orientations and misorientations were measured using a semi-automatic Kikuchi diffraction method (Liu et al., 1998). The dislocation density in several samples was measured using a linear intercept method on TEM images of individual grains taken under multi-beam diffraction conditions to reveal the dislocation content within the grains (Norfleet et al., 2008). This was done by drawning test lines randomly within the given cell in the micrograph and the dislocation density (ρ_d) was thereafter calculated (Hirsch et al., 1965) as:

$$\rho_d = \frac{2 \cdot N_l}{t_{foil}} \tag{4.9}$$

where N_l is the number of interceptions at dislocations per unit test line and t_{foil} is the foil thickness which was measured by convergent beam electron diffraction.

Chapter 5

Structure and tensile behavior of nanostructured Al

The nanostructured sample produced by 6 cycles ARB is the base material in the present project. In this chapter, the structure and tensile behavior of this base material will be described.

5.1 Structure

Fig. 5.1 shows a TEM image of the structure in the 6C-ARB sample, showing a typical lamellar structure that is characterized by lamellar boundaries and short interconnecting boundaries. The lamellar boundaries were parallel to the rolling plane, with an average spacing of 0.4 μm. The presence of individual dislocations or loose dislocation tangles was observed within the lamellae that were subjected to strong diffraction conditions (see Fig. 5.2). Sample tilting in the TEM confirmed that almost all lamellae contained dislocations in the interior. The dislocation density was measured to $1.0x10^{14}m^{-2}$.

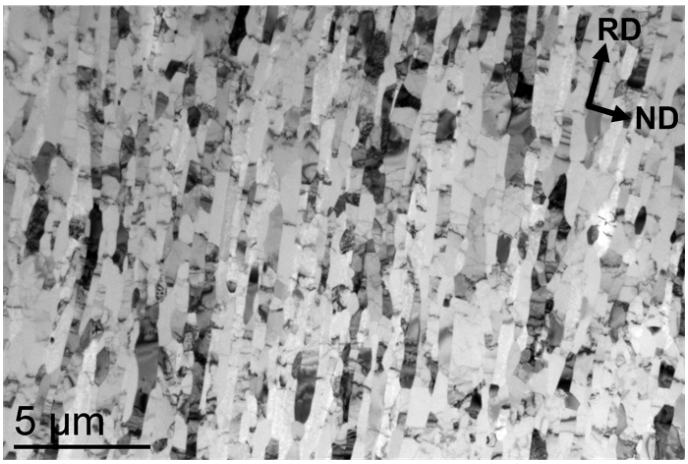

Figure 5.1: *TEM image showing lamellar structural morphology for the sample processed by 6 ARB cycles.*

Fig. 5.3 shows the misorientation distribution across boundaries for the 6 cycle ARB processed sample which has many high angle boundaries (60.7%) with misorientations above 15°.

Furthermore there is a large fraction of low angle boundaries especially with a misorientation below 2° (15.2%). This gives a bi-model misorientation profile with one peak around 50° and the other in the small misorientation angle range.

Fig. 5.4 shows the bonding layer from a roll bonding interface which lies parallel to the RD. The bonding layer is not continuous but breaks up which is seen here by large thinning. This is in accordance with the principles of roll bonding shown in Fig. 3.2. The bonding layer consists of a fine lamellar structure mixed with fine oxide particles which is not visible in Fig. 5.4.

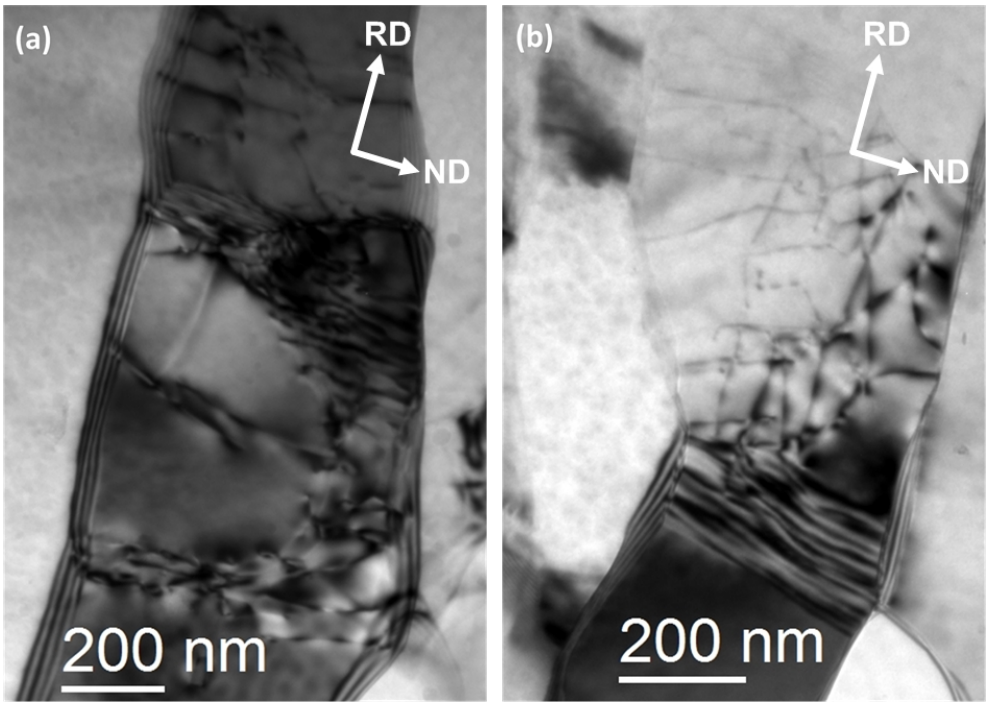

Figure 5.2: *TEM image showing interior dislocation configurations for the 1050 Al sample processed by 6 ARB cycles.*

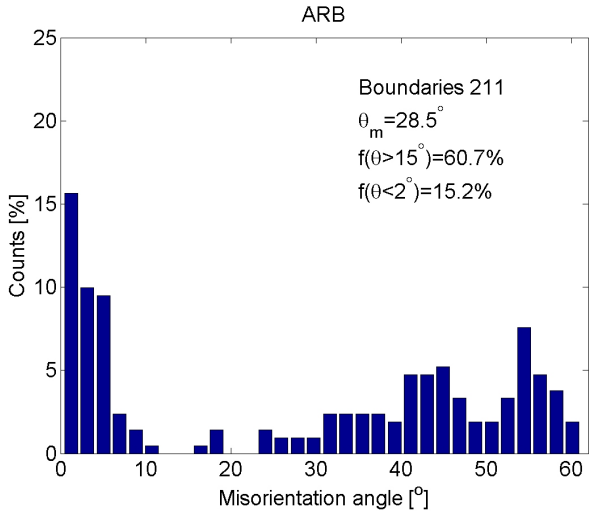

Figure 5.3: *Misorientation angles across lamellar boundaries and interconnecting boundaries for the ARB sample.*

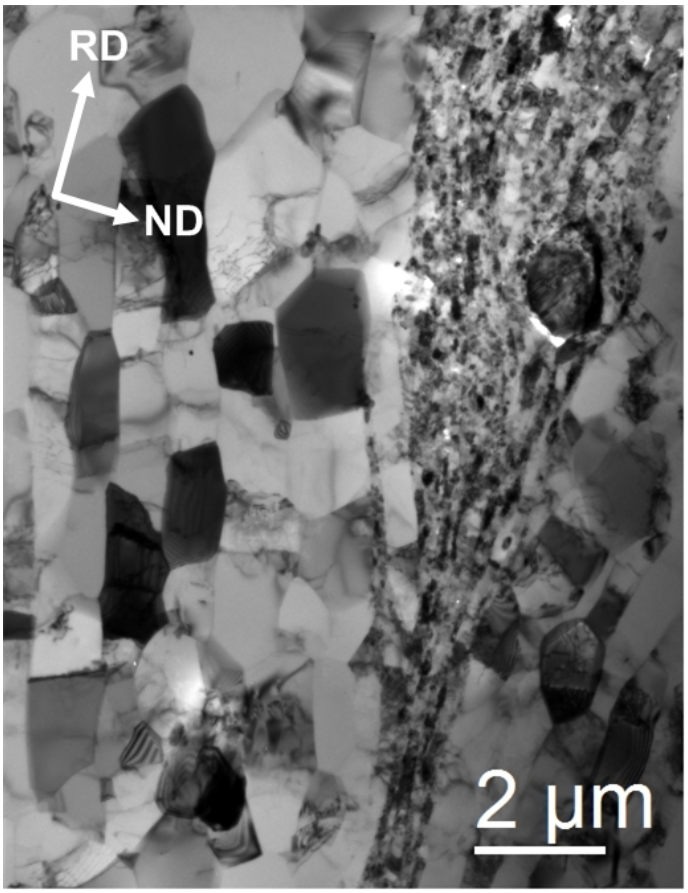

Figure 5.4: *TEM image showing a bonding layer from a roll bonded interface from a sample produced by 6 cycles of ARB and subsequently annealed for 30 minutes at 175°C. This sample will be further introduced in the next chapter.*

5.2 Texture

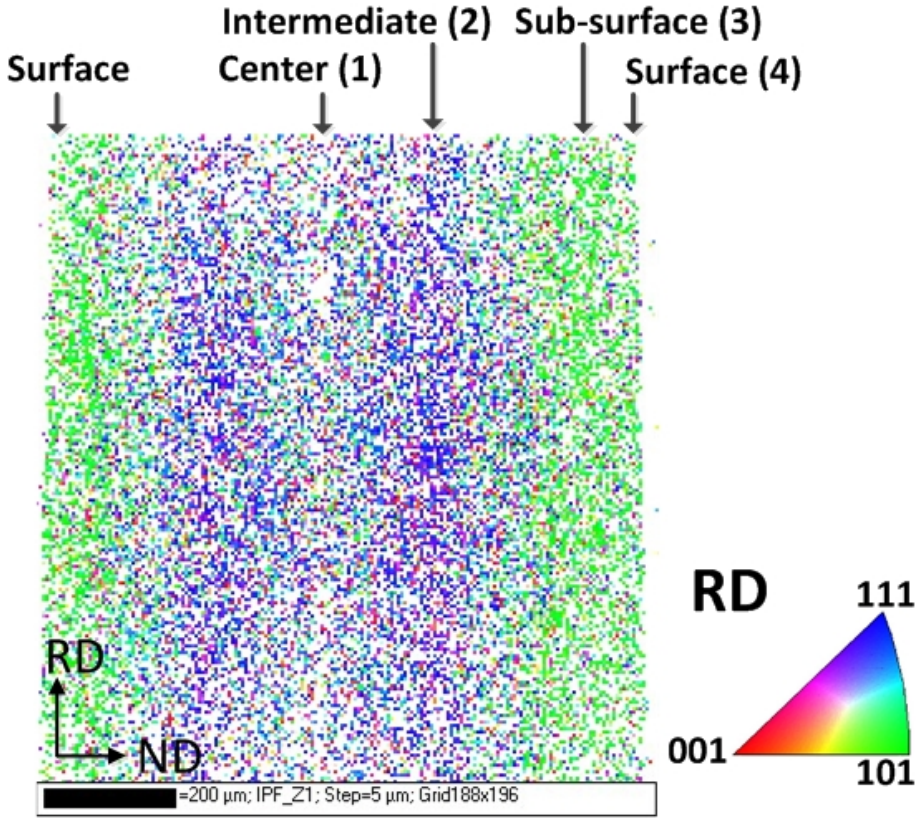

Figure 5.5: *EBSD map of the 6 cycle ARB sample.*

Fig. 5.5 shows the development of through-thickness texture gradients characterized by the formation of a rolling texture with RD|||[111] in the inner layers and shear texture with RD|||[101] in the outer layers. The EBSD map is indicated with the numbers one to four which refer to: the center region (1), the intermediate region (2), the sub-surface region (3) and the surface region (4). Table 5.1 shows the fraction of the dominant rolling texture components (Brass, Copper and S) and shear texture components (45ND RTCube) for the different regions. Each texture component was defined using a maximum 15° deviation from the ideal orientation. Note

that the strongest rolling texture and shear texture are formed in the intermediate and sub-surface regions, respectively. The {111} pole figures corresponding to these two regions are shown in Fig. 5.6.

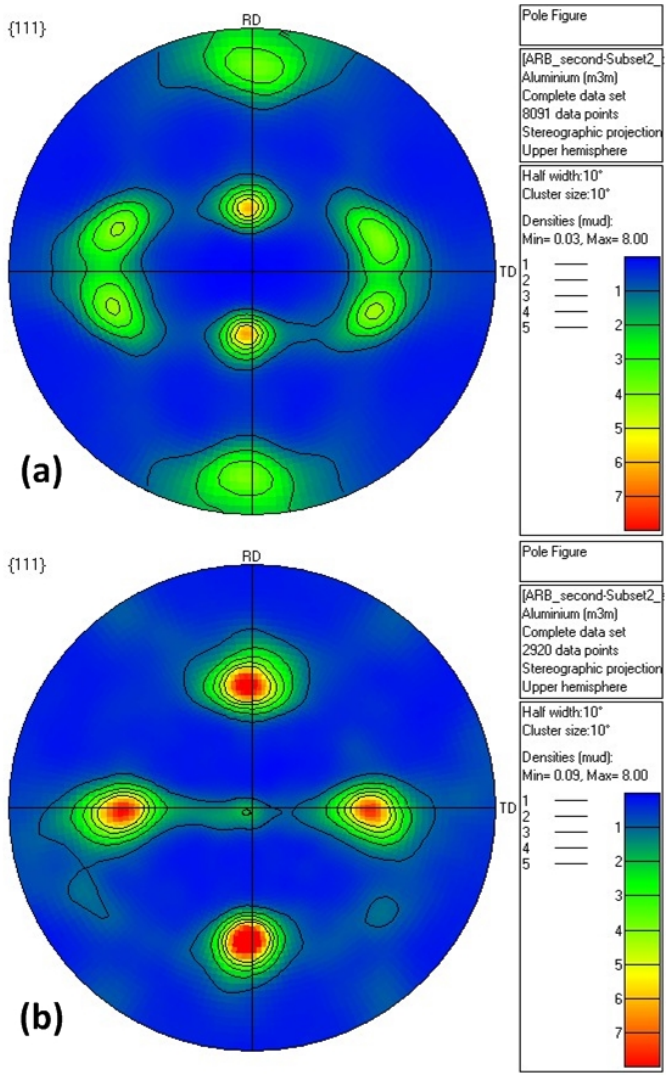

Figure 5.6: {111} *Pole figures for the ARB sample at (a) the intermediate region (2) (b) the sub-surface region (3).*

Fig. 5.6(a) shows a clear rolling texture composed of copper, brass and S components, which are shown in Fig. 4.15, and Table 5.1 shows that copper is dominant.

Table 5.1: Dominant shear and rolling texture components for the 6 cycle ARB sample at the center region (1), the intermediate region (2), the sub-surface region (3) and the surface region (4). The regions (1-4) are indicated in Fig. 5.5.

Components	Other	Brass	Copper	S	45ND RTCube
Center region (1)	54.74%	5.68%	18.48%	12.90%	5.00%
Intermediate region (2)	44.21%	4.75%	25.91%	18.60%	4.23%
Sub-surface region (3)	56.54%	0.72%	1.85%	1.68%	38.08%
The surface region (4)	75.73%	0.29%	1.61%	1.17%	19.88%

Fig. 5.6(b) shows a clear shear texture composed of the $\{001\}\langle 110\rangle$ rotated cube (45° rotated) component.

The texture was also measured after 2% tensile strain but no significant difference was observed.

5.3 Tensile properties

All the tensile specimens tested were taken from a single 6 cycle ARB sheet and 3 repetitions were done. In the following, the mean values for both strength and uniform elongation are reported, as well as the maximum value for the total elongation. As mentioned earlier the material after several cycles of ARB becomes 2-4 times stronger than the coarse-grained counterpart. Fig. 5.7 shows the tensile stress-strain curve of the 6 cycle ARB-processed material (ARB). For comparison, the stress-strain curve of the coarse grained (CG1050) sample used as the starting material for the ARB processing is also included in the figure.

The 6 cycle ARB sample has a yield stress (0.2 % offset) of 135 MPa and an UTS of 187 MPa. The tensile ductility of the ARB sample is, however, low. The uniform elongation is 1.7 % and the total elongation is 7.5%. The necking behavior right after the UTS exhibits a very steep stress decay

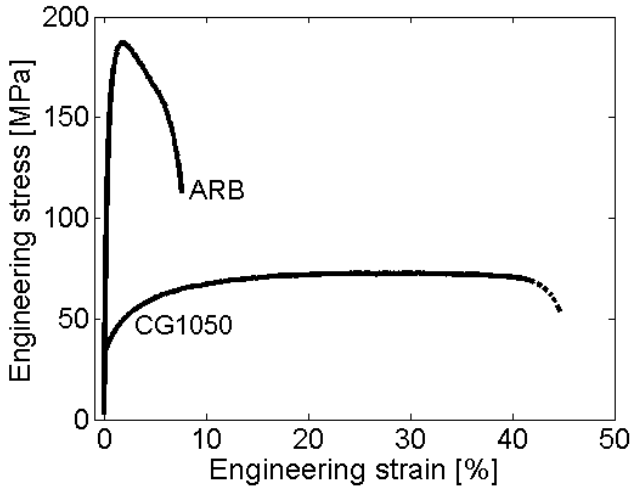

Figure 5.7: *Tensile engineering stress-strain curves for the starting material (CG1050) and a sample processed by 6 cycles of ARB*

while the CG1050 sample has a nearly flat decay after UTS.

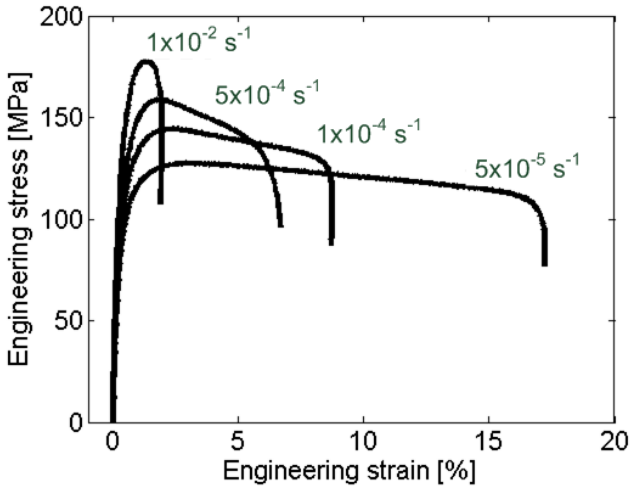

Figure 5.8: *Engineering stress-strain curves for 6 cycle ARB samples tested with initial strain rate ranging from* $1x10^{-2}$ *to* $1x10^{-5}s^{-1}$.

The strain rate sensitivity was pronounced for nanostructured metals. Fig. 5.8 shows the engineering stress-strain curves of samples tested with different initial strain rates ranging from $1x10^{-2}$ to $1x10^{-5}s^{-1}$ for the 6 cycle

ARB sample. It can be observed that the samples exhibit a strong strain rate dependency. At a high strain rate ($1x10^{-2}s^{-1}$) the tensile stress shows a steep decrease immediately after the UTS with both the uniform and post-UTS elongation being around 1%. By decreasing the strain rate the uniform elongation increases while the post-UTS elongation increases quite substantially and reaches around 15% at the slowest strain rate ($1x10^{-5}s^{-1}$). To obtain the strain rate sensitivity exponent (m), strain rate jump tests were performed as described in Section 4.1.2. Fig. 5.9 shows the m-exponent as a function of tensile strain. It is seen that the m-exponent gradually decreases from 0.048 at a strain of 2% to 0.036 at a strain of 10%.

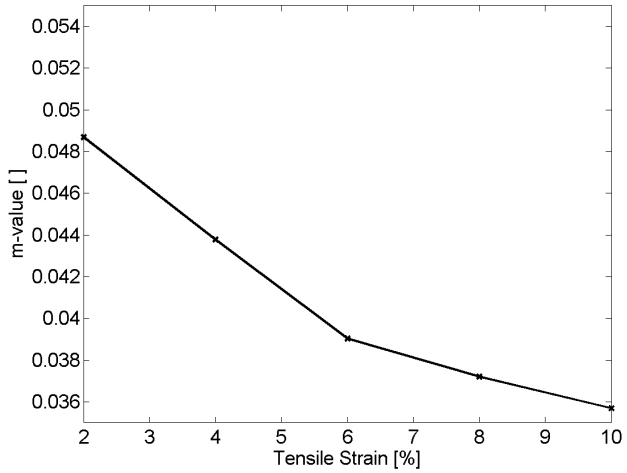

Figure 5.9: *Strain rate sensitivity exponent (m) from strain rate jump tests calculated for different tensile strain values.*

5.3.1 Anisotropy

To evaluate the anisotropy as described in Section 4.1.3.2, five samples were tested in all three directions (0°, 45° and 90° to the RD) and the results (R-values) are shown in Table 5.2 for the CG1050 and the 6 cycle ARB sheets.

Some experiments failed due to poor recognition in the ARAMIS system and these results have been exempted. The mean R-value and standard deviation (std) in all three directions were calculated. The strains used to find the R-values (see Eq. 4.2) were at a 1% tensile strain.

Table 5.2: Anisotropy values for the 0°, 45° and 90° orientations to the rolling direction for CG1050 and 6 cycle ARB samples

CG1050			
Sample no	0°	45°	90°
1	1.08	1.04	1.14
2	1.05	0.99	1.13
3	1.09	0.90	0.90
4		0.95	1.27
5		1.01	
R-value	1.08	0.98	1.11
std	0.01	0.05	0.15

6 cycle ARB			
Sample no	0°	45°	90°
1	0.76	2.29	0.38
2	0.47	1.71	0.65
3	0.60	1.61	0.49
4		1.28	0.66
5		1.51	0.83
R-value	0.61	1.68	0.60
std	0.14	0.37	0.17

The R-value for the ARB sample was higher than one in the 45° direction and lower than one in 0° and 90° directions, while the R-values for the coarse grained sample were about one in all directions, i.e. near isotropic. The ΔR value calculated from Eq. 4.4 for the CG1050 is close to zero, which is an advantage in deep-drawing.

5.4 ARAMIS analysis of strain evolution during tensile testing

The strain evolution during tensile testing was investigated using the DIC system described in Section 4.1.3. To the author's knowledge, this technique has not been used to study the local strain distribution of nanostructured metals in tension before.

The samples tested in this investigation were prepared from a 6 cycle ARB sheet different from the samples used for conventional tensile tests (see Fig. 5.3). It was noted that the strength level is lower than that seen in Fig. 5.3. However, all the analyses done with ARAMIS were cut from a single ARB sheet, making the results directly comparable.

In the following, the analysis of the tensile strain behavior was divided into two regions; split at the UTS into a pre- and post-UTS region, i.e. the pre-UTS behavior evaluating the strain evolution before the UTS and the post-UTS behavior investigating the necking behavior of the sample. After the overall behaviors of these two regions have been presented a more quantitative analysis of the width strain over the entire test will be shown.

5.4.1 Pre-UTS behavior

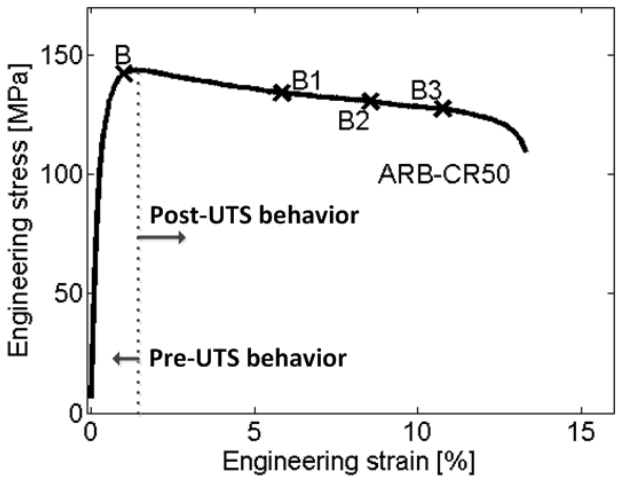

Figure 5.10: *Zoom of the stress-strain curve where the crosses indicate the positions at which the strain distributions over the sample gauge length were analyzed.*

Fig. 5.10 is a zoom of the stress-strain curve and shows the locations

where the strain distributions were made to understand the pre- and post-UTS behavior.

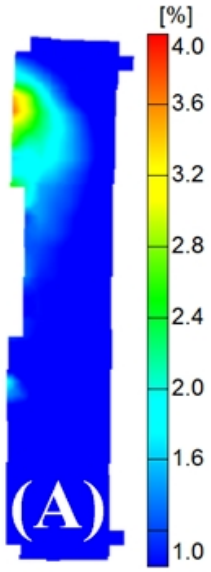

Figure 5.11: *Strain distribution map of the localized strains of the ARB tensile samples showing strong localization after 1% tensile strain. The colors represent the amount of strain and can be read in the scalebar.*

Fig. 5.11 shows the distribution of tensile strain over the sample gauge at a nominal tensile strain of 1% (position A), which is considerably earlier than the UTS at 1.7% (see Fig. 5.10). The strain distribution maps were plotted showing tensile strain. This show that the localized deformation at the top of the gauge, already has a local tensile strain of as high as 4% which is approximately 4 times larger than that of the nominal tensile strain (Kidmose et al., 2012a). Similar localization behavior has been seen in all the ARB samples tested with ARAMIS. Such a strain localization, as here observed before the UTS point, was unexpected.

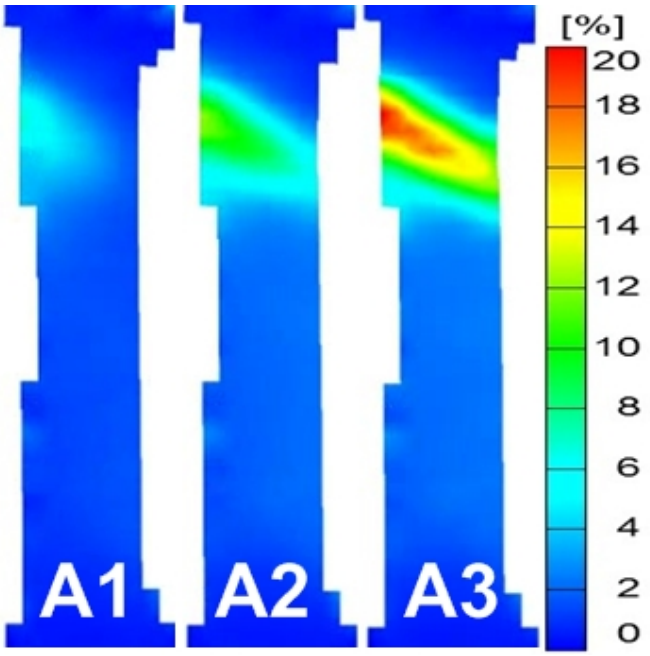

Figure 5.12: *Snapshots taken from the ARAMIS movies showing the strain distributions at three different strain levels A1 (1.7 %), A2 (3.0 %), and A3 (4.1 %) for a 6 cycle ARB sample. Note that the scale bar for the images are different from that used in Fig. 5.11.*

5.4.2 Post-UTS behavior

As described above, the ARB sample develops localized deformation at low strains before the UTS point. At the UTS (A1) a clear inhomogeneity can be seen even with the coarser scale bar used in Fig. 5.12. The maximum localized strain at (A1) has increased to approximately 6%. Upon further straining to a total strain of 3% this localized deformation develops into a shear band (A2) and the strain in this localized shear band has been doubled to approximately 12%. Straining the sample to a total strain of 4.1% the localized strain in the shear band is further increased to about 20%. Tensile deformation in the gauge region that was not influenced by the shear band reaches a strain of 2-3% before fracture, which was estimated by varying

the strain scale bar. One example of such a practice is shown in Fig. 5.13 (marked gauge with a strain scale spanning from 1 to 4%) at a tensile strain of 6%. Deformation in the shear band reaches local strain values above 40% before the dot pattern becomes so distorted that ARAMIS cannot follow the evolution. This is also shown in Fig. 5.13 (marked shear band) where the scale bar was set relatively high.

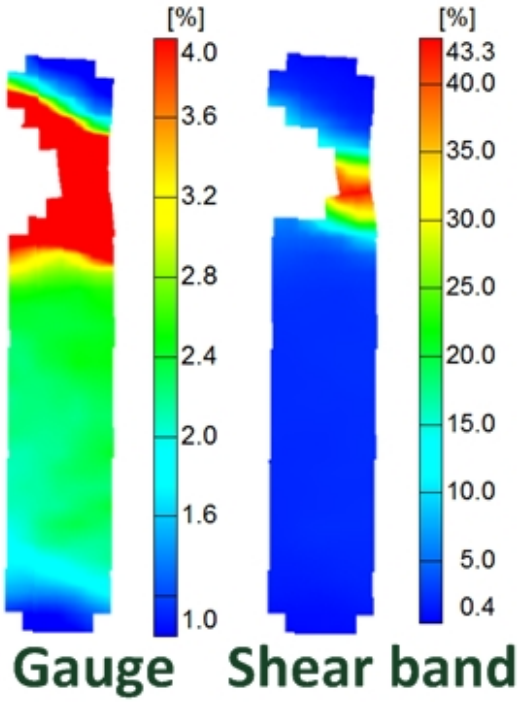

Figure 5.13: *Snapshots taken from the ARAMIS movies showing the strain distributions at two different strain levels gauge (6 %) and shear band (6.2%) for the ARB sample. Note that the scale bars for the snapshots in the figures are not the same.*

5.4.3 Width strain

Fig. 5.14 shows the analysis of the evolution of width strain versus tensile strain. The width strain was analyzed for eight locations marked by lines 1-8, as shown in the inserted strain distribution maps. It was seen that the

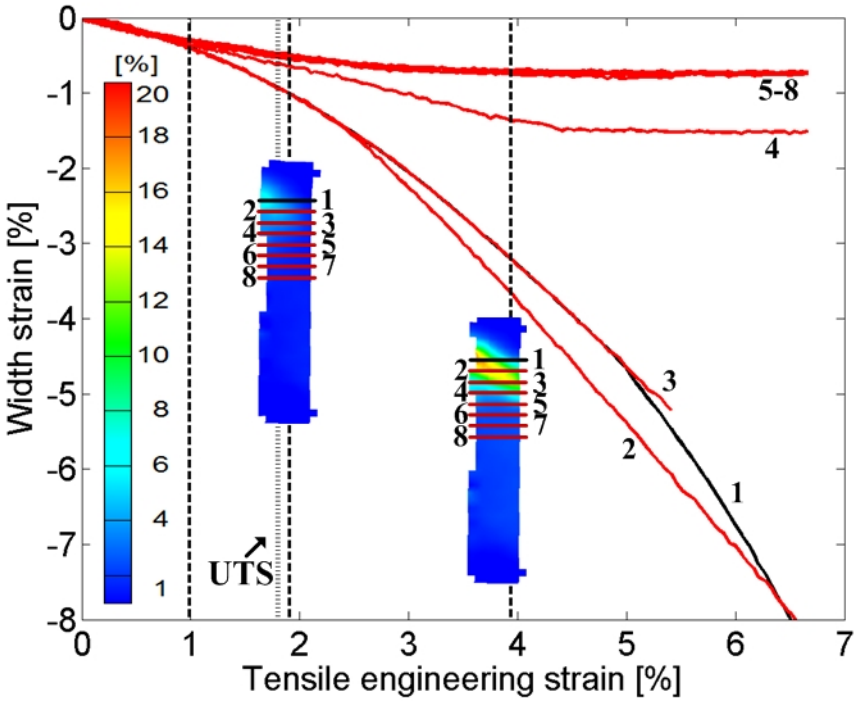

Figure 5.14: *Analysis of width strain versus tensile strain for locations marked by lines 1-8 in the inserted strain distribution maps.*

first strain inhomogeneities appear before the UTS. This reveals the onset of localized contraction already at 1% tensile strain, which was considerably before the UTS at 1.7%. The region affected by strong and continuously increasing localization was covered by lines 1, 2 and 3. Line 4 covers the region next to the localized band. It is seen that the width strain in this position increases much slower and levels-off at a tensile strain of about 4%. The region marked by lines 5-8 is outside of the localized shear band and the width strain shows minimum values over the entire tensile strain range.

Fig. 5.14 also clearly shows the development in the shear band (lines 1-3) while the remaining part of the gauge saturates (lines 4-8). Line 1 was placed right at the center of the final necking region and there was approximately 1 mm between lines which means that the shear band affects

around 6 mm of the gauge part due to its angle. The shear band crosses the sample width at an angle of about 65° to the tensile direction most clearly seen in (A2) and (A3) (see Fig. 5.12).

5.5 Discussion

5.5.1 Structure and strength

The essential structural parameters characterizing nanostructured metals produced by high strain deformation are structural morphology, spacing between boundaries, misorientation across boundaries, and the density of dislocations present in the volumes between the boundaries. The present 6 cycle ARB processed Al (99.5% pure) shows a typical lamellar structure, a bimodal misorientation distribution and a certain density of interior dislocations. Similar structural characteristics have been reported by (Huang et al., 2008b; Huang, 2009) for a 99.2% pure Al processed by 6 cycles ARB. The main difference seen is in the lamellar boundary spacing, which is about 400 nm for the present 6 cycle ARB Al and it is about 200 nm for 6 cycle ARB 99.2% pure Al. Höppel et al. (2008a, 2004) observed a lamellar boundary spacing of 320 nm for a 6 cycle ARB processed Al with similar purity to the present alloy, however the starting material they used for ARB processing was in a warm rolled state, rather than in a recrystallized state as in the present study. Their results suggest that the impurity has a rather large effect on the structural refinement.

The tensile behavior of the present 6 cycle ARB processed sample also exhibits the typical behavior of nanostructured metals produced by high strain deformation, namely a significantly increased strength but a limited

tensile ductility, particularly at a rather low uniform tensile elongation. The tensile strength of the present ARB sample is lower than those reported by Huang et al. (2008b) for ARB processed 99.2% Al and by Höppel et al. (2004) for ARB processed (but probably higher total deformation strain) 99.5% Al (see Table 5.3), which can be easily related to the difference in the structural scale.

Table 5.3: Structural and mechanical comparison of the ARB sample from the present study and literature values.

	Present study	(Höppel et al., 2004)	(Höppel et al., 2008a)
ARB cycles	6	5	6
Boundary spacing	400 nm	320 nm (at 8 cycles)	324 nm
Yield stress	135 MPa	-	150 MPa
UTS	187 MPa	225 MPa	175 MPa
Uniform elongation	1.7%	2.5%	1.7%
Total elongation	7.5%	8%	7%
Strain rate	1e-3s^{-1}	7e-4s^{-1}	1e-4s^{-1}
m-exponent	0.036-0.049	0.03	-

5.5.2 Texture

The development of shear versus rolling textures during cold rolling are dependent on the l/h ratio which was described earlier. If the l/h ratio is less than 0.5 the shape change effect dominates and leads to a large shear component at the sample surface, while if the l/h ratio is kept between 0.5 and 5, a near-homogeneous rolling texture will form (Mishin et al., 2000). If the l/h ratio is increased to over 5, a friction-induced effect at the surface of the contact length will dominate and lead to surface shear (Verlinden, 2007). This knowledge can be used to explain the formation of the different texture components in the ARB sheet. The texture showed the development of through-thickness texture gradients characterized by the formation of a rolling texture in the inner layers and a shear texture in the outer layers

due to the inhomogeneous rolling (l/h=8.7) with a large friction between the sample and rolls due to the fact that ARB processing was carried out without lubrication. Similar results were observed by Huang et al. (2006b) for a 99.99% pure aluminium, processed by ARB. Note that a weak rolling texture was formed in the center region which indicates that the plane strain deformation imposed in the center region in the last ARB cycle destroys the shear texture formed in the preceding cycles. Before roll bonding when the sheets are stacked, the two surfaces that have to be welded together exhibit a shear texture but after the roll bonding they become the center layer where the shear texture was rotated toward a rolling texture. In Heason and Prangnell (2002) it was found that the shear texture which was dominated by 45° rotated cube can be rotated to a copper orientation by plane strain deformation such as rolling.

5.5.3 Anisotropy

The anisotropy values obtained for the present 6 cycle ARB Al are typical for rolling texture, i.e. a high value at 45 degree direction and smaller values at zero and 90 degree direction. Beausir et al. (2010) has found anisotropy values for a similar material purity and the values are summarized with the present mean values in Table 5.4 both for an aluminium with the same purity.

Table 5.4: Comparison of R-values obtained in this study and reported previously (Beausir et al., 2010) for similar material conditions.

In sheet direction	CG1050	CG1050 from (Beausir et al., 2010)	ARB	6C-ARB from (Beausir et al., 2010)
0	1.08	0.9	0.61	0.43
45	0.98	0.33	1.68	1.2
90	1.11	0.93	0.6	0.5

Table 5.4 shows that the R-values of the present CG1050 are close to the values in all directions making it nearly isotropic, while this was not the case for the initial material of Beausir et al. (2010). Their starting material probably has a recrystallization texture with a strong cube component, which gives a low R-value in the 45 degree direction.

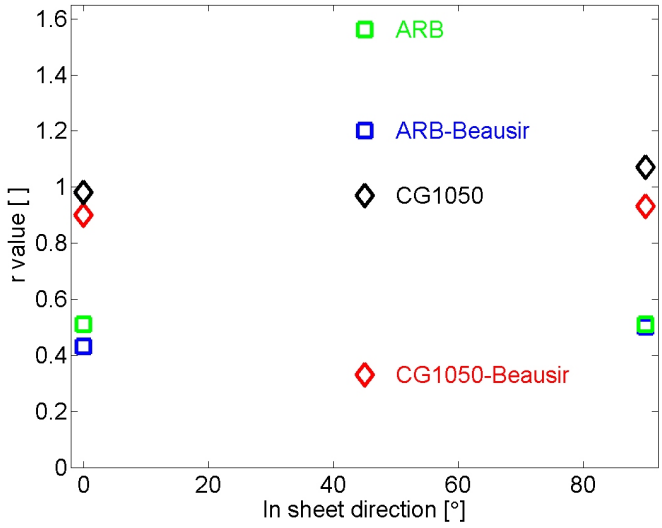

Figure 5.15: *Visualization of the values in Fig. 5.4 of the in-plane anisotropy of the CG1050 and ARB sheets from the present study and values from (Beausir et al., 2010).*

In Fig. 5.15, R-values from the current study and various literature have been plotted to give a better visualization of the differences in data. The variation in the initial material could also play a role in the difference in the final R-values but it was believed that the tendencies after ARB processing were the same. In Höppel et al. (2008a) tensile testing in both zero and 90 degree directions were conducted and similar results obtained to the present study. This indicates that the R-value in these two directions should be similar which is also seen in the current study.

5.5.4 Tensile instability

It has not been fully understood why the onset of localized strain develops so early in the ARB sample. What is surprising is that the ARAMIS analysis shows that the strain localization already occurs before the UTS. In general, the tensile instability is given as (Considere, 1885; Meyers and Chawla, 1984):

$$\frac{d\sigma_T}{d\epsilon_T} = \sigma_T \tag{5.1}$$

where σ_T and ϵ_T are the true stress and strain, respectively, and $\frac{d\sigma_T}{d\epsilon_T}$ is the work-hardening rate. Using the simplifications and advanced data analysis approach explained in Section 4.1.4, the true stress-strain curve can be determined. Fig. 5.16 shows the tensile curves for the ARB sample derived in three different ways.

The engineering stress is the load divided by the initial area and the engineering strain is the change in length divided by the initial specimen length. The true stress and strain can be calculated using Eq. 4.6 and Eq. 4.7 and is applicable in the homogeneous tensile strain region. The true stress-strain curve measured by ARAMIS uses the actual area. A thorough description can be found in Section 4.1.4. In this special case the necking cross section was not perpendicular to the tensile axis but inclined at 65° to the tensile axis similar to the shear band. The ARAMIS measured true stress-strain curve does not extend as long as the engineering stress-strain curve due to a lack of recognition of the strain when the shear band develops very high local strains which are partly shown in Fig. 5.13.

The slope of the true stress-strain curve in Fig. 5.16 represents the work-hardening rate which is plotted in Fig. 5.17. The thin black line in the plot

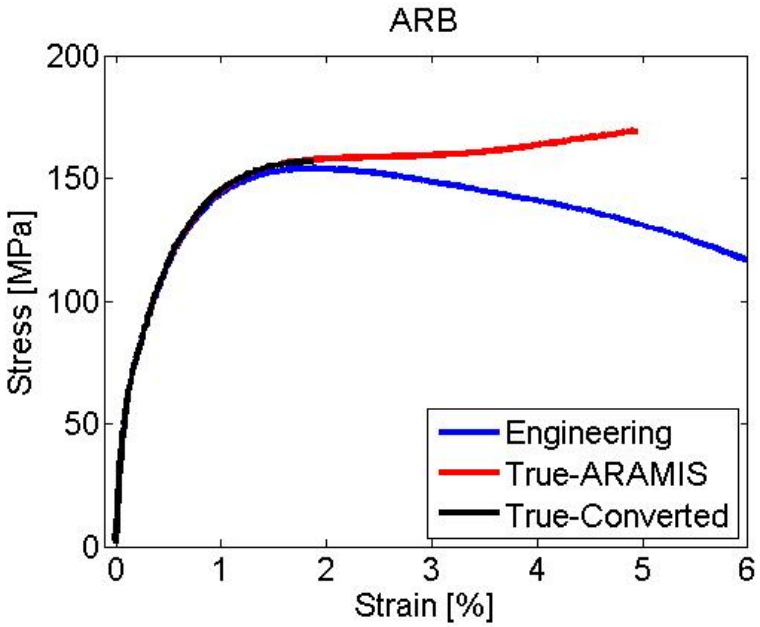

Figure 5.16: *Tensile curves for the ARB sample in engineering and two true stress-strain curves.*

is where work-hardening is equal to the true stress, hence the intersection between the two lines is where the Considère criterion is reached. This was close to 110 MPa in true stress, corresponding to a nominal strain of 0.45%. At this tensile strain level, the strain distribution map is shown in Fig. 5.18 where the onset of localization is clearly seen at the upper left corner of the specimen. Â´

This observation indicates that the classical interpretations of necking from both uniform elongation and Considère are not totally valid for the early necking exhibited in the ARB sample, which was not fully understood.

The gauge part which was not affected by the shear band only experienced low tensile strains (2-3%) which was around 20 times less than what was observed in the shear band. This means that the extension of the shear band was limited and that nearly all the plastic deformation takes place in

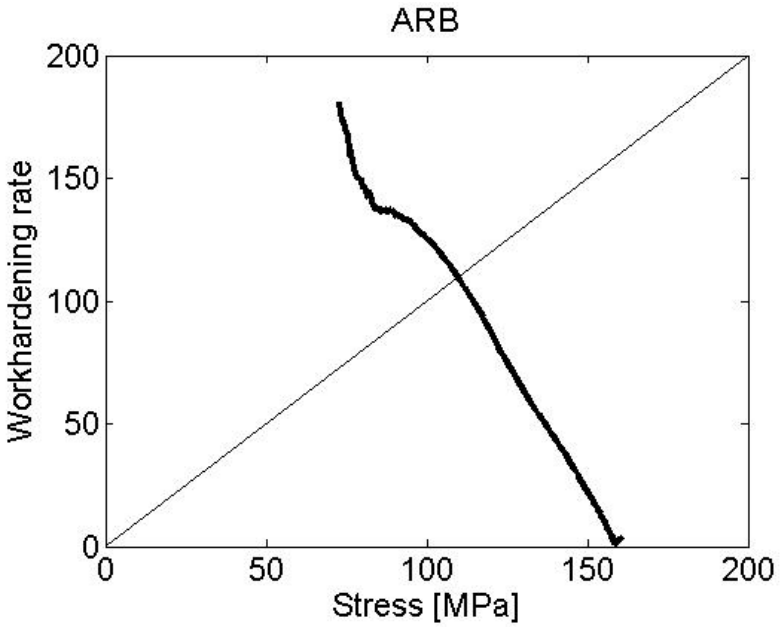

Figure 5.17: *Kocks-Mecking (K-M) plot for the ARB sample where the work-hardening rate was plotted over true stress.*

this band.

5.6 Summary

The 6 cycle ARB processed Al sample shows a well-developed lamellar structure with a lamellar boundary spacing of about 400 nm, a bimodal misorientation distribution (with high angle boundaries of about 60%) and a dislocation density of $1.0x10^{14}m^{-2}$, which forms a good base structure to explore the effects of a post-process annealing and deformation. The tensile behavior shows a significantly enhanced strength but limited tensile ductility, typical of nanostructured metals produced by high strain deformation. The application of ARAMIS analysis to map the evolution of strain distribution over the gauge section of the tensile specimens reveals quantitatively the initiation of localized shear band even before the UTS and the

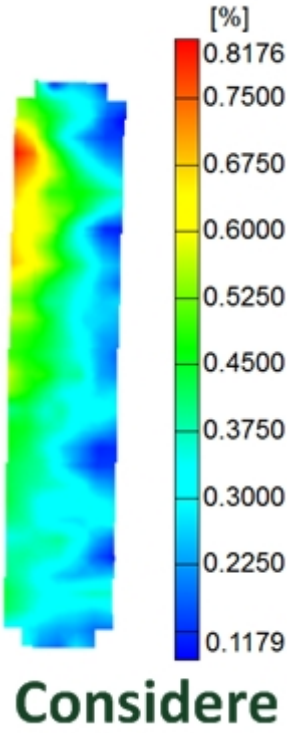

Figure 5.18: *Snapshot taken from the ARAMIS movie showing the strain distributions at a nominal tensile strain of 0.45%.*

concentration of strain in the shear band. This suggests that such a strain distribution analysis technique is well suited for the investigation of tensile instability, which is a central issue in the study of the effect of post-process treatment on the tensile behavior to be described in the next chapter.

Chapter 6

Effects of Post-Process Treatment (P-PT) on structure and tensile behavior

Following the detailed characterization of the structure and mechanical properties of the 6 cycle processed state, in this chapter, post-process annealing or deformation is applied to the 6 cycle processed material to investigate these post-process treatments (P-PT) on the structure and tenstile properties of the nanostructured Al.

6.1 Annealing

Annealing treatments were conducted at three relatively low temperatures, 175°C, 200°C, and 225°C at which the structural change is expected to be dominated by recovery. The samples are hereafter referred to as ARB-175, ARB-200 and ARB-225 to indicate that the annealing was done as a post-process treatment.

6.1.1 Structure

Microstructural characterization was done for two selected samples, namely the samples annealed at 175°C and 225°C.

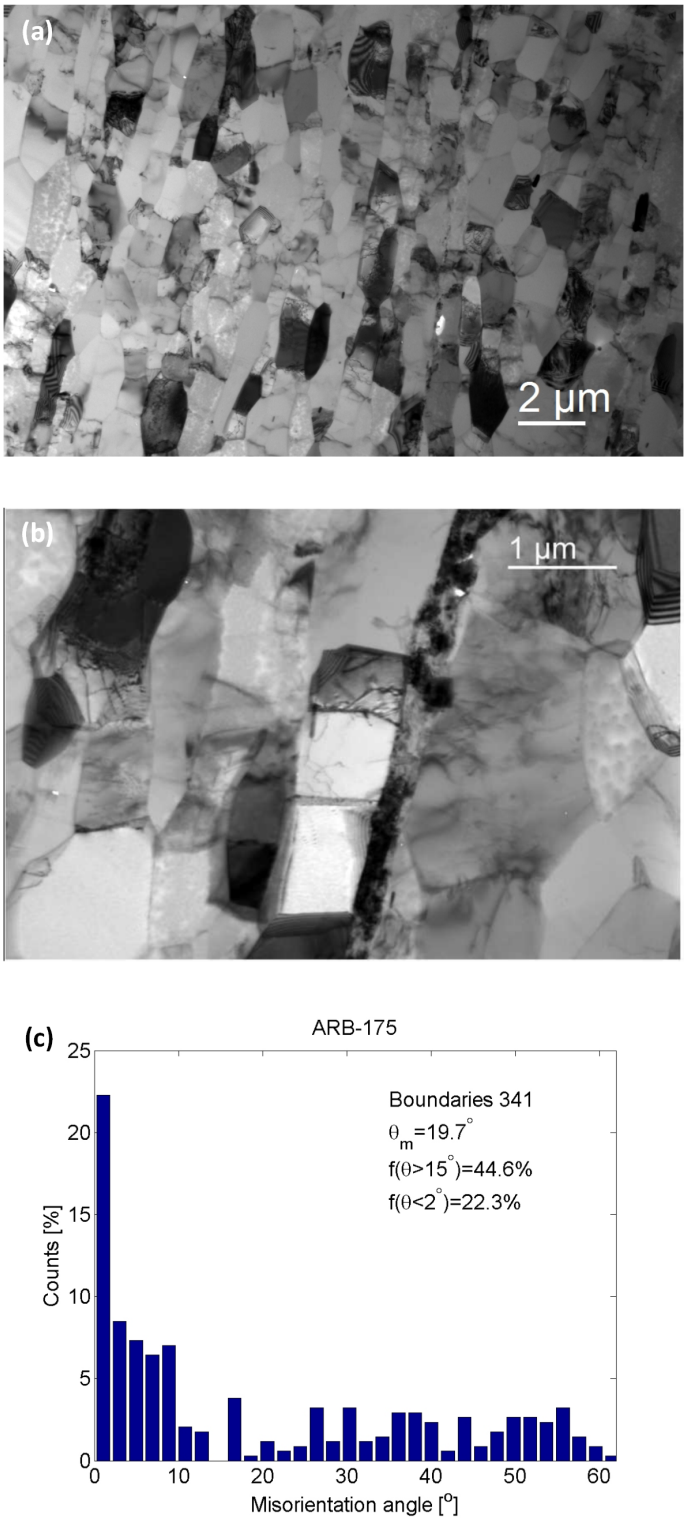

Figure 6.1: *TEM image showing (a) a lamellar morphology (b) interior dislocation configurations (c) misorientation distribution in the ARB-175 sample.*

Table 6.1: Boundary spacing measured for the ARB, ARB-175, and ARB-225 samples where the number indicates the post-process annealing temperature.

Sample	Boundary spacing [nm]
ARB	394
ARB-175	646
ARB-225	1455

Fig. 6.1 shows the TEM observations of the microstructure in the ARB-175 specimen. It is seen that this specimen still exhibits a lamellar structure similar to the ARB sample (Fig. 5.1) but with a coarser lamellar boundary spacing. The spacings were quantified and shown in Table 6.1 for a comparison with the ARB sample. Fig. 6.1(b) shows that the lamellae still contain dislocations in the volume, but the dislocation density is lower than that in the ARB sample shown in Fig. 5.2. Fig. 6.1(c) shows that the misorientation distribution measured by TEM is similar to that of the ARB sample (Fig. 5.3). The ARB-175 sample has a bimodal misorientation with many high-angle boundaries but also a large fraction of low-angle boundaries with a misorientation below 2° (22.3%).

Fig. 6.2(a) shows that increasing the annealing temperature will result in a more equiaxed structure with an average grain size of 1455 nm. Observations in higher magnification, Fig. 6.2(b), shows that there are still dislocations present in some equiaxed grains/subgrains. This suggests that the formation of an equiaxed structure is a result of extended recovery, which is also supported by boundary misorientation measurements, as shown in Fig. 6.2(c). It is seen from this figure that after annealing at 225°C the misorientation distribution is similar to the initial state (Fig. 5.3) and there are still a rather high fraction of low angle boundaries (29%). It is interesting to note that the ARB-175 sample shows an even higher fraction of low angle

boundaries with misorientation $< 2^\circ$ than that seen in the ARB sample.

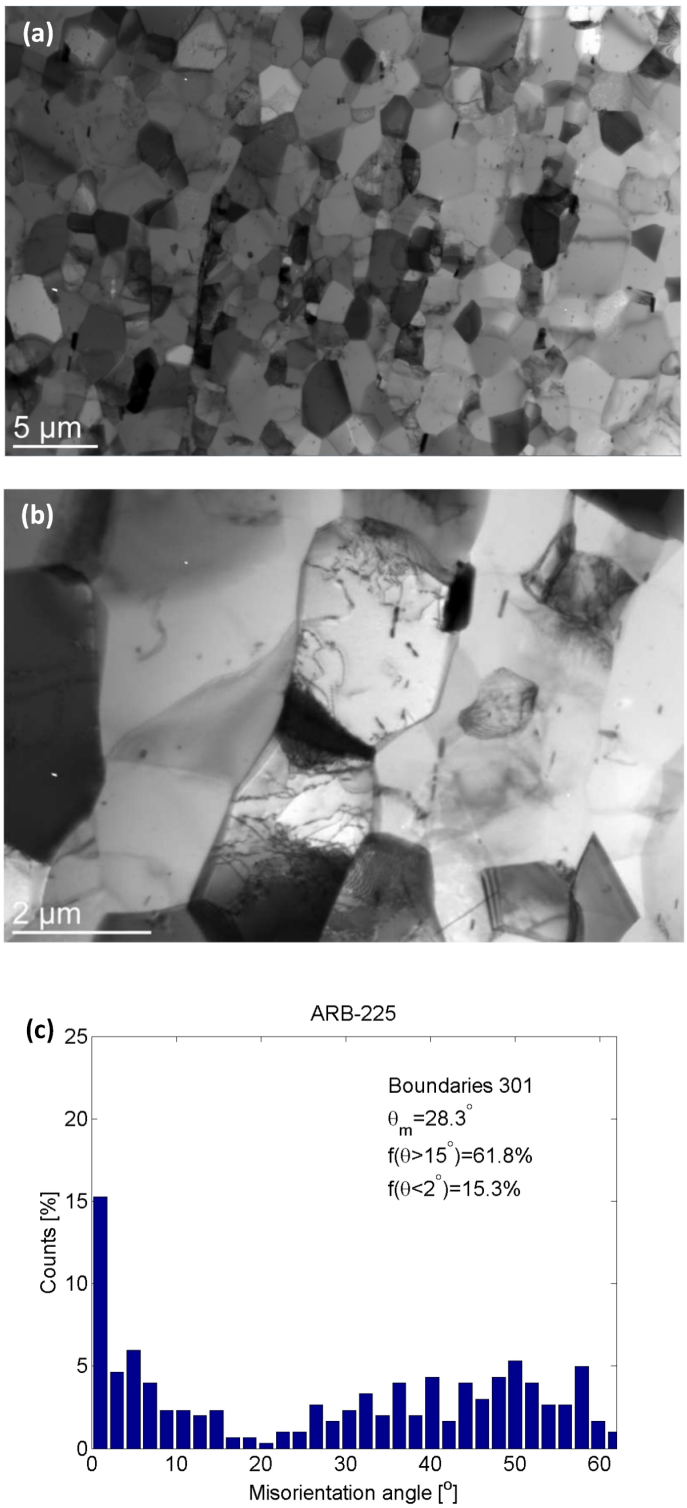

Figure 6.2: *TEM image showing (a) boundary morphology which shows a more equiaxed structure (b) interior dislocation configurations (c) misorientation distribution in the ARB-225 sample.*

6.1.2 Texture

The texture has only been evaluated for the ARB-225 sample and it was very close to the ARB sample, seen in the previous chapter. The ARB-225 sample also shows shear texture at the surface (see Fig. 6.3(a)) and rolling texture in the center (see Fig. 6.3(b)). The pole figure of the center covers the entire center part (purple) while the pole figure for the surface only covers the right side of the sample (green, see Fig. 6.4). There is also a weak shear texture along the roll-bonded layer right at the center as visible in Fig. 6.4.

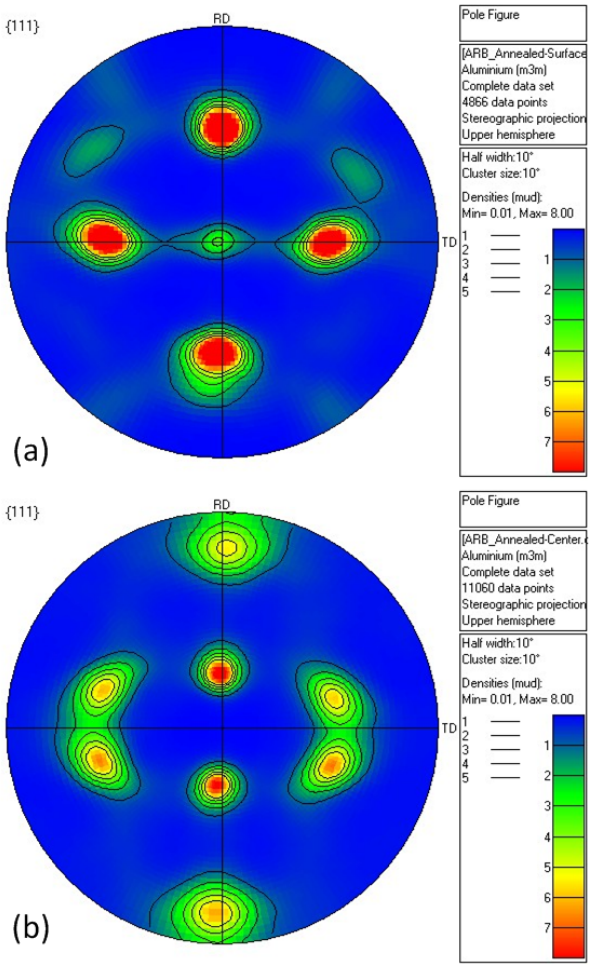

Figure 6.3: {111} *Pole figures for the ARB-225 sample at (a) the surface region (b) the center region.*

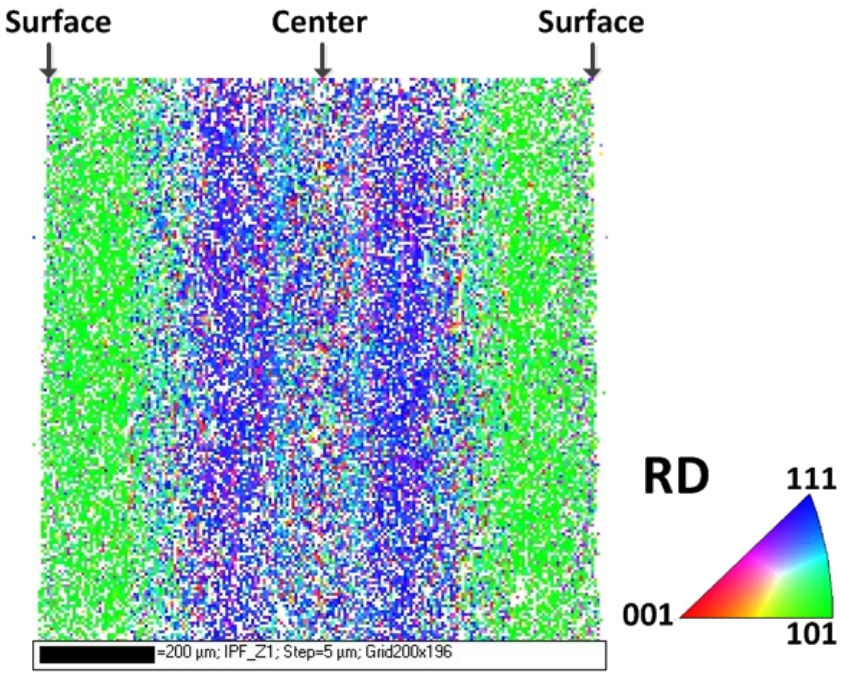

Figure 6.4: *EBSD map of the ARB-225 sample*

The fractions of the dominant texture components are presented in Table 6.2 and were defined using a maximum 15° deviation from the ideal orientation. The ARB-225 sample has a high fraction of copper and 45ND RTCube in the center and surface respectively. Compared with the ARB sample (Table 5.1) the annealing has sharpened the texture. Texture was also measured after 10% tensile strain, and no significant changes was observed.

Table 6.2: Texture components for ARB-225 sample at the center and surface.

Components	Other	Brass	Copper	S	45ND RTCube
ARB-225 surface	44.53%	0.10%	0.49%	0.41%	53.90%
ARB-255 center	36.11%	1.62%	38.15%	17.35%	3.87%

6.1.3 Tensile properties

To minimize the data scatter all the tensile specimens used to investigate annealing effects were taken from a single ARB sheet before the annealing treatment. The stress-strain curves of annealed samples are shown in Fig. 6.5 where the stress-strain curves of CG1050 and ARB samples are also included for comparison. The strength and elongation of these samples are shown in Table 6.3. Annealing is a well-known method used to increase material ductility at the expense of the mechanical strength.

Surprisingly, the flow instabilities were significantly enhanced by annealing at 175°C, where a sharp and deep drop in the flow stress at a very small strain was seen in the curve, causing a rapid fracture of the sample. The sample has a yield stress of 138 MPa and a UTS of 146 MPa. The 175 annealed sample is slightly higher than the yield stress of the ARB sample (Table 6.3) which will be discussed later. When the temperature was in

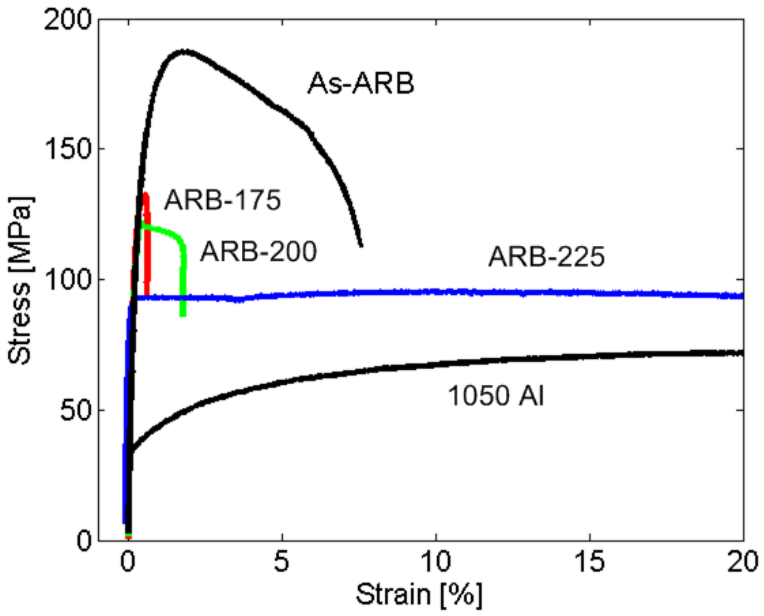

Figure 6.5: *Stress-strain curves for CG1050, ARB and all the post-process annealed samples denoted by the annealing temperatures over a 30 minute period*

the range of $200 - 225$°C, a yield point phenomenon was observed, with the Lüders band deformation being complete at 225°C but incomplete at 200°C. The ARB-200 sample has a steep decay right after the UTS (118 MPa) that goes on a few percent before fracture occurs. The ARB-225 which shows a yield point phenomenon and Lüders band formation and propagation of 5% tensile strain has a yield stress of approximately 98 MPa. Since the work-hardening was very limited the yield stress and UTS at an uniform strain of 10% remain fairly similar (100 MPa). Note that the elongation was restored so that the ARB-225 sample has a total elongation of 28%.

Table 6.3: Tensile data from the nominal stress-strain curves for the ARB and annealed samples.

	Yield stress [MPa]	UTS [MPa]	Uniform elongation [%]	Total elongation [%]
ARB	135	187	1.7	7.5
ARB-175	138	146	0.5	0.7
ARB-200	117	118	0.4	1.4
ARB-225	98	100	10	28

6.1.4 Anisotropy

The anisotropy was determined for the ARB-225 sample and is presented in Table 6.4. In the table it is seen that the R-values are less than one for both the 0° and 90° directions while the R-values for the 45° direction is above 2. Clearly there is no big change as compared with the ARB sample (Table 5.2).

Table 6.4: Anisotropy values for the 0, 45 and 90 degree orientation to the rolling direction for ARB-225 and ARB-225-CR5

ARB-225			
Sample no	0	45	90
1	0.93	2.24	0.47
2	0.36	2.93	0.34
3	0.28	2.91	0.92
4	0.87	1.71	0.34
5			0.34
R-value	0.61	2.45	0.48
std	0.33	0.58	0.25

6.1.5 ARAMIS analysis of strain evolution during tensile testing

The tensile behavior analysis done by ARAMIS for the ARB-225 sample focuses on verifying the Lüders band formation and propagation. Note again this analysis was done on tensile samples from another ARB sheet different from the previous one used for the conventional tensile tests (Fig. 6.5).

6.1.5.1 ARB-225

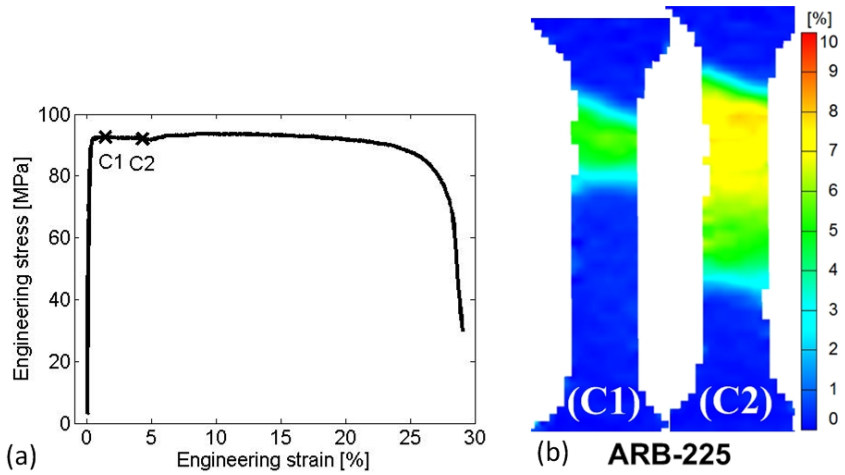

Figure 6.6: *(a) The stress-strain curve where the crosses, C1 and C2, indicate the positions at which the strain distributions were analyzed. (b) Strain distribution maps for the analysis of the ARB-225 sample at C1 and C2 showing the evolution of the Lüders band.*

The tensile stress-strain curve in Fig. 6.6(a) shows that with this particular sample a Lüders band was formed at one end of the sample and then propagated through the gauge length, giving rise to a constant stress up to a tensile strain of 5%. The propagation of the front of the Lüders band is shown in Fig. 6.6(b) by strain distribution maps of 1.4% and 4.3% tensile strain indicated in Fig. 6.6(a). The strain distribution map (C1) shows an early stage of the Lüders band formation and the strain distribution map (C2) shows the state when the Lüders band propagation is nearly complete.

Fig. 6.7 shows a better visualisation of the propagation of the Lüders band as a sequential occurrence of a sudden change in the width strain analyzed for the different locations indicated by (lines 1, 2, 3, 4, and 5 marked on the sample in Fig. 6.7). Note line 5 marks the location where the Lüders band is initiated. Interestingly, there was a small homogenous straining in

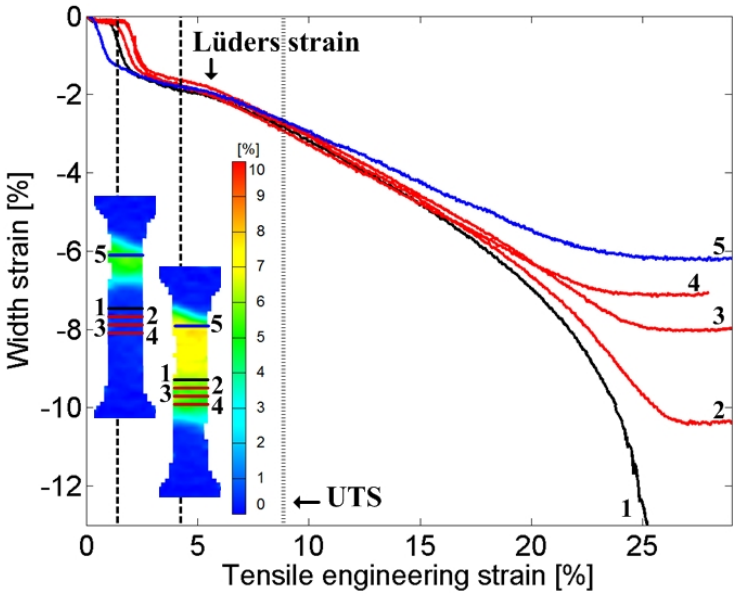

Figure 6.7: *Analysis of width strain as a function of tensile strain for the ARB-225 sample showing Lüders band formation and propagation.*

the band while the front still propagates as evidenced by the constant non-negligible slope of the width strain between the sudden drop and the final spread of the Lüders band over the gauge length at a tensile strain of 5%. The width strains at the five locations develop in a similar manner until the UTS point and then that corresponding to line 5 starts to depart from the general trend. The width strain at lines 1-4 was fairly homogenous up to a tensile strain of approximately 15%. Necking eventually takes place at line 1. The final necking behavior was similar to that seen in CG1050.

6.2 Deformation

To investigate the post-ARB deformation effect the 6 cycle ARB samples were subsequently cold-rolled to 5, 15, 30, and 50% (hereafter the samples produced are named ARB-CR5, ARB-CR15, ARB-CR30, ARB-CR50, respectively).

6.2.1 Structure

The ARB-CR15 and ARB-CR50 have been selected for structural characterization. Typical images for the ARB-CR15 sample (Fig. 6.8(a)) and the ARB-CR50 sample (Fig. 6.8(b)) are shown at two different magnifications, both showing typical lamellar structure with boundaries parallel to the RD, as in the ARB sample (Fig. 5.7).

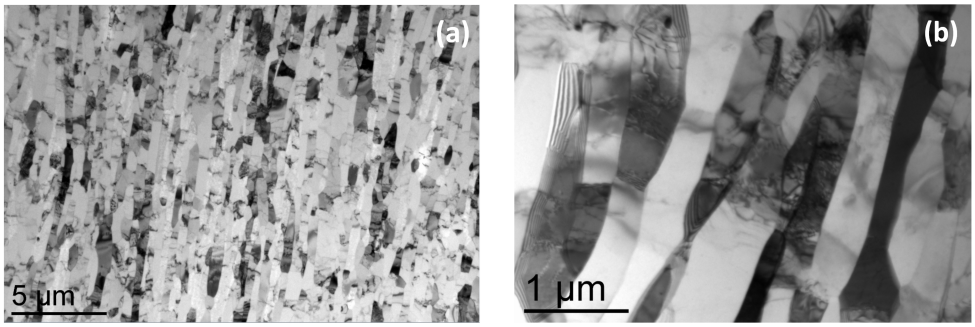

Figure 6.8: *TEM images showing a lamellar structural morphology for (a) the ARB-CR15 sample and (b) the ARB-CR50 sample.*

In Table 6.5 the lamellar boundary spacings and dislocation densities measured for the ARB, ARB-CR15 and ARB-CR50 samples are summarized. With increasing post-ARB rolling it was observed that the lamellar boundary spacing decreases. Compared to the ARB sample, the ARB-CR50 sample shows a decrease of lamellar boundary spacing by about 10 %.

Table 6.5: Lamellar boundary spacings and dislocation densities measured for the ARB, ARB-CR15, and ARB-CR50 samples

Sample	Dislocation density [1/m^2]	Boundary spacing [nm]
ARB	1.0E+14	394
ARB-CR15	1.59E+14	389
ARB-CR50	2.12E+14	352

The presence of individual dislocations or loose dislocation tangles was observed within almost all the lamellae that were oriented to strong diffraction conditions. Examples showing the dislocation structures within the lamellae are given in Fig. 6.9 for the ARB-CR15 sample (see Fig. 6.9(a)) and for the ARB-CR50 sample (see Fig. 6.9(a)). The data in Table 6.5 show that there is an increase in the dislocation density with increasing post-ARB rolling.

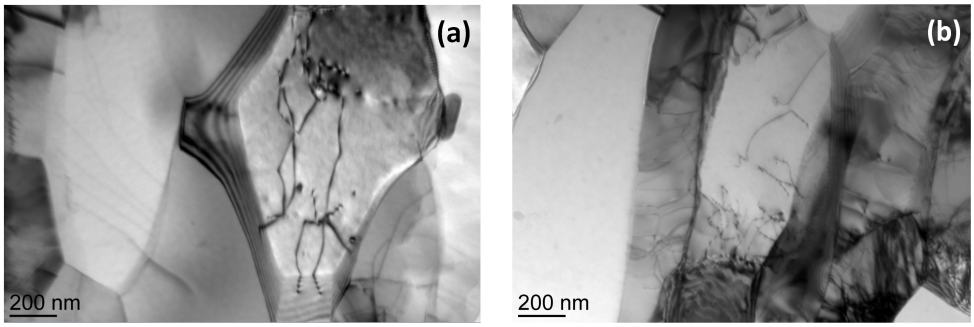

Figure 6.9: *TEM images showing interior dislocation configurations in (a) the ARB-CR15 sample and (b) the ARB-CR50 sample.*

6.2.2 Texture

The ARB-CR50 sample has been chosen for texture analysis for which a change in texture distribution is expected from the initial and ARB states. An EBSD orientation map through the sample thickness, {111} pole figures corresponding to the surface and center region and quantified volume

fraction of different texture components are shown in Fig. 6.10, Fig. 6.11 and Table 6.6 respectively.

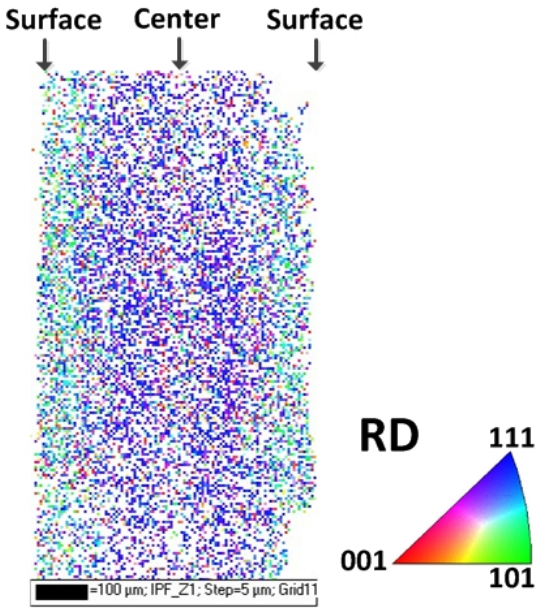

Figure 6.10: *EBSD map of the ARB-CR50 sample*

The EBSD map (Fig. 6.10) shows that the green color at the surface, which is an indication of shear texture as seen in the ARB sample (Fig. 5.5), was only seen vaguely. The pole figure of the center (Fig. 6.11(b)) covers the entire center part while the pole figure for the surface only covers the left side of the sample. The center shows a strong rolling texture, as expected.

Table 6.6: Dominant shear and rolling texture components for the center and surface of the ARB-CR50 sample.

Components	Other	Brass	Copper	S	45ND RTCube
ARB-CR50 surface	56.84%	2.37%	18.25%	6.93%	11.93%
ARB-CR50 center	26.29%	4.50%	40.30%	26.12%	0.97%

For the surface region the pole figure in Fig. 6.11(a) clearly shows that 50% cold rolling has caused that the 45ND RTCube orientation in the surface layer of the ARB sample rotates around TD towards the copper

orientation. Both variants of copper corresponding to rotations in opposite directions were observed, but one variant is however much stronger than the other. Table 6.6 shows that the 45ND RTCube texture is significantly weakened in the ARB-CR50 sample as compared with the ARB sample (Table 5.1).

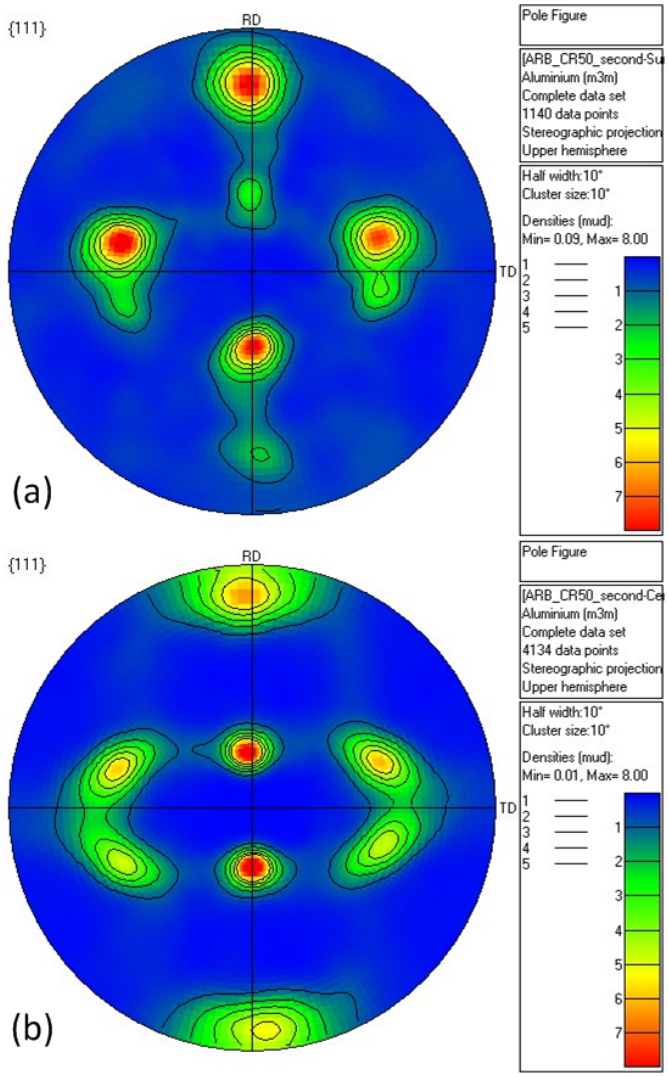

Figure 6.11: {111} *Pole figures for the ARB-CR50 sample at (a) the surface region (b) the center region.*

6.2.3 Tensile properties

The tensile specimens applied different P-P cold rolling were prepared from a single ARB sheet, as for the ARB samples tested in Section 5.3 and Section 6.1.3 for the annealed samples so that the results on the P-P rolling effects can be compared. The stress-strain curves for the ARB and post-ARB rolled samples are shown in Fig. 6.12.

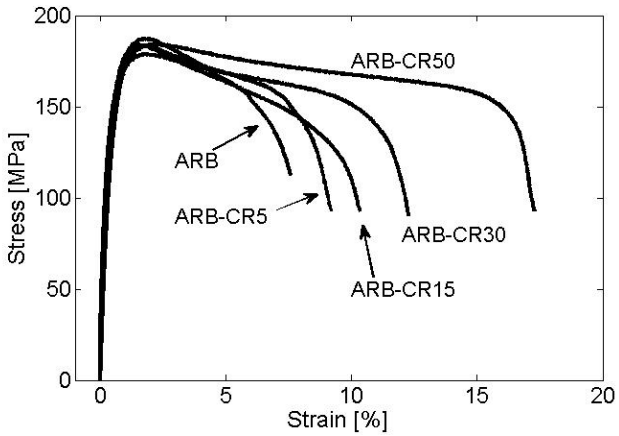

Figure 6.12: *Engineering stress-strain curves for samples post-ARB rolling applied from 0 to 50% in thickness reduction.*

The mechanical properties measured from the tested samples are summarized in Table 6.7. For both the yield stress (0.2% offset) and UTS, no significant effects of P-P rolling are seen within the strain range applied (5-50% thickness reduction). The difference in strength is within about 10 MPa among the samples. However the UTS of all the ARB-CR samples are lower than the ARB sample indicating a softening caused by P-P cold rolling although such a tendency is not seen for the yield stress that may be related to the larger uncertainty in determining the yield stress. A much more significant effect was seen in the tensile ductility. Although the uniform elongation was similar for all samples the post-UTS elongation in-

creased gradually and monotonically when increasing the post-ARB rolling strain up to 50 % (Table 6.7). The total elongation was increased from 7.5 % in the ARB sample to 17 % in the ARB-CR50 sample. Clearly, the tensile stability was significantly increased after post-ARB cold rolling.

Table 6.7: Tensile data from the nominal stress-strain curves for the ARB and ARB-CR samples.

	Yield stress [MPa]	UTS [MPa]	Uniform elongation [%]	Total elongation [%]
ARB	135	187	1.7	7.5
ARB-CR5	130	183	1.6	9.3
ARB-CR15	147	181	1.6	10.3
ARB-CR30	144	179	1.7	12.5
ARB-CR50	138	184	2.0	17.0

6.2.4 Anisotropy

The anisotropy data were very close to the values found for the ARB sample, but the ARB-CR50 showed a slightly lower value in the 45° direction than the ARB.

Table 6.8: Anisotropy values for the 0°, 45° and 90° orientations to the rolling direction for ARB-CR50

ARBCR50			
Sample no	0°	45°	90°
1	0.49	1.06	0.80
2	0.70	0.86	0.60
3	0.79	2.01	0.41
4	0.53	1.26	1.17
5	0.73	1.48	0.72
R-value	0.65	1.33	0.74
std	0.12	0.44	0.28

6.2.5 ARAMIS analysis of strain evolution during tensile testing

The ARB-CR50 sample showed the largest enhancement in the tensile ductility, and was thus selected to do a detailed ARAMIS analysis. It should be pointed out that the samples used for the ARAMIS tests were machined from a different ARB sheet than the ones shown previously in Section 6.2.2, but all the samples tested with ARAMIS (Section 5.4 and Section 6.1.5) were prepared from the same ARB sheet.

As for the ARB sample the strain evolution analysis by ARAMIS was divided into two parts split at the UTS value; A pre-UTS study investigating whether the ARB-CR50 sample has early strain localizations like the ARB sample, followed by a post-UTS study investigating how the post-ARB cold rolling changes the mechanical behavior. In the following, the analysis of the strain evolution of these two regions will be presented. A more quantitative analysis of the width strain over the entire test will be followed.

6.2.5.1 Pre-UTS behavior

Fig. 6.13 shows the stress-strain curve of the ARB-CR50 sample for the ARAMIS test. The locations where the strain distribution maps were obtained for the pre and post-UTS behavior analysis are indicated by crosses (B, B1, B2 and B3).

Fig. 6.14 shows the strain distribution maps at 1% tensile strain, which is before the UTS at 1.4%. The same strain distribution map (B) is shown twice with two different scale bars. The strain distribution map with the maximum of 4% strain (right) which is the same as used in Fig. 5.11 for the ARB sample. Here no hetrogeneities are observed and also no indica-

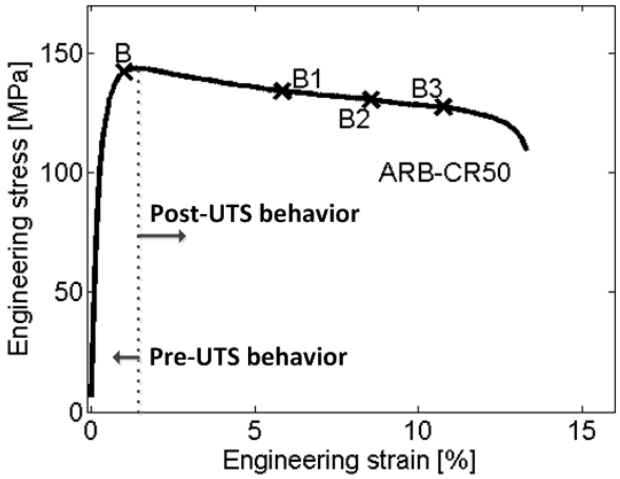

Figure 6.13: *Stress-strain curve from the ARAMIS test of the ARB-CR50 sample. The crosses indicate the positions for the analysis of strain distributions. B refers to the snapshot on the curve in Fig. 6.15.*

tions of localizations in the uniform region of the ARB-CR50 sample. In the strain distribution map in Fig. 5.11(left) of the ARB-CR50 sample with a higher strain resolution small strain localizations around 0.5% above the nominal tensile strain (1%) was observed, indicating that strain localization also occurs. The localizations do not fluctuate under the test so they are assumed to be real localizations and not an artifact of the analysis. The small localizations exist over the entire test, but do not grow until the very end of the test. This will be described in more detail subsequently.

It should be pointed out that the strain distribution maps have been edited to remove an edge effect that was dominant at small tensile strains (below the UTS). The edge effect was an artifact of the analysis, caused by the calculation method at the sample edge.

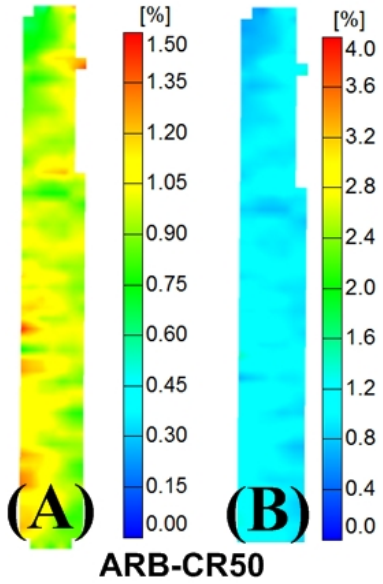

Figure 6.14: *Strain distribution maps of the ARB-CR50 sample showing only small, but no dominant localization up to the UTS.*

6.2.5.2 Post-UTS behavior

To investigate the post-UTS elongation three strain distribution maps in Fig. 6.15 (named B1-B3) where taken from ARAMIS at three specific strain levels as indicated in Fig. 6.13.

In the ARB-CR50 sample there was no indication of shear bands or any strain inhomogeneities of significance below a tensile strain of 6% (B1) even though the UTS occurs at a much lower strain. Local necking with very high local strain was also found, but not until the end of the tensile test (B3). Between the homogeneous part and local necking there was an intermediate region showing some localization (B2). The important observation was that part of the enhanced post-UTS elongation was homogenous (Kidmose et al., 2012b).

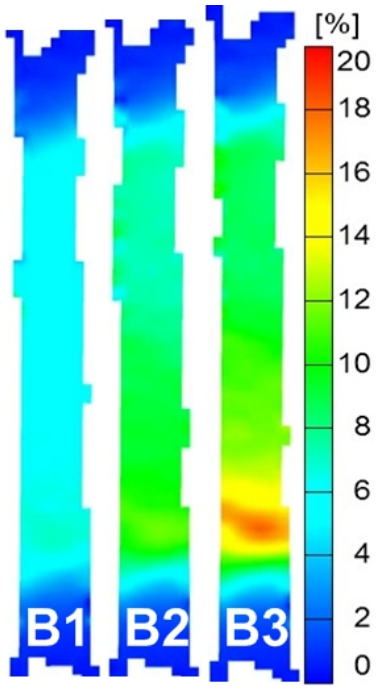

Figure 6.15: *Snapshots taken from the ARAMIS movies showing the strain distributions at three different strain levels B1 (5.8 %), B2 (8.5 %), and B3 (10.8 %) for the ARB-CR50 sample*

6.2.5.3 Width strain

The width strain analysis, Fig. 6.16, clearly shows that the gauge width is nearly homogeneous up to around 6%. By further straining the intermediate region is observed where the entire gauge length still deforms but at different rates. At around 10% tensile strain distinct local necking is observed where lines 1 and 2 rapidly increases while the upper part of the gauge saturates (lines 8-9).

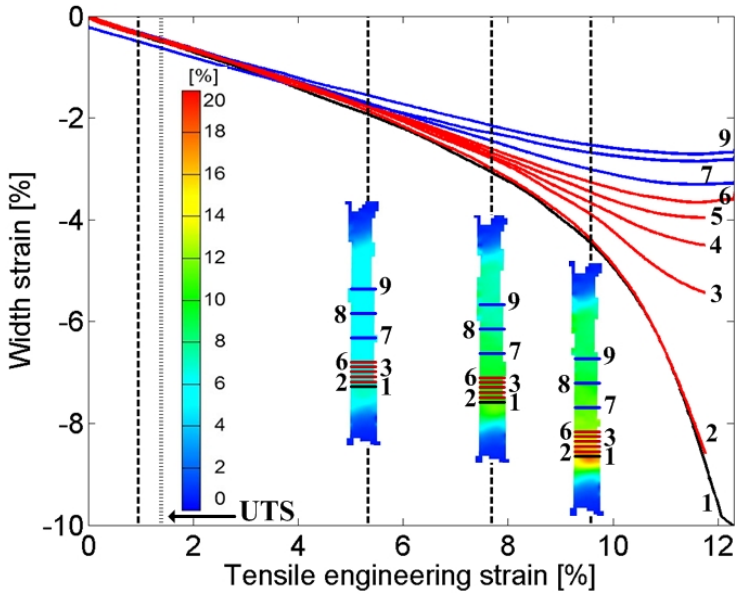

Figure 6.16: *Evolution of width strain as a function of tensile strain for the ARB-CR50 sample showing fairly homogeneous deformation up to several percent after the UTS.*

6.3 Discussion

The practice of applying P-P treatments to the 6 cycle ARB processed Al samples has revealed two unexpected effects on the tensile behaviors. The first effect is related to the P-P annealing, which is seen as an annealing-induced enhancement in the tensile instability. The second effect is related to the P-P deformation, which is observed as a deformation-induced stabilization of the tensile deformation. In the following, these effects will be first discussed based on the observations of changes in microstructure and texture and on the results of the evolution of strain distribution. The positive effect of P-P deformation in stabilizing the tensile deformation is then explored by applying additional cold rolling to low temperature annealed specimens.

6.3.1 Tensile instability enhanced by annealing

The annealing effect on tensile instabilities has been studied by Kamikawa (2006) in nanostructured 99.2% pure 1100Al samples processed by 6 cycle ARB. Similar to the present observations (Fig. 6.5), two different types of enhanced tensile instabilities occur depending on the annealing temperature. When annealed at temperatures below 225°C, a sharp and deep drop in the flow stress takes place at a very small strain, causing a rapid fracture. When the annealing temperature is in the range of 225-275°C, a yield point phenomenon occurs with the Lüders deformation being complete at 250°C. Comparing the present observations (Fig. 6.5) with these previous observations, great similarities are seen in the effect of annealing temperature on the occurrence of two types of enhanced tensile instability. However, it should be pointed out that after similar ARB processing the present material shows a much coarser lamellar boundary spacing (400 nm versus 200 nm) and a lower tensile strength (about 190 MPa versus 300 MPa) than the material used by Kamikawa, which is probably a result of a higher purity of the present material (99.5%). It may thus be concluded that the annealing enhanced tensile instabilities are common behaviors for nanostructured Al over a relatively wide structural range scale and tensile strength level. Fig. 6.17 shows enlarged views of the initial part of the stress-strain curve for the ARB sample and the ARB-175 sample. It is seen that both samples depart from the elastic deformation at a rather low stress (about 60 MPa), but the ARB-175 sample keeps a steeper slope than the ARB sample up to a plastic strain of about 0.2%. It should be pointed out that the higher slope was reproducible and it has also been observed by Kamikawa (2006) and by Huang et al. (2006a) in ARB processed and 150°C annealed 99% Al. The higher slope can be understood as an indicator of a lower mobile dislocation

density and thus a more difficult initiation of macroscopic plastic flow. The 0.2% offset stress determined from the stress-strain curves showed that it is slightly higher for the ARB-175 sample than for the ARB sample. Likewise it should be noticed that the theoretical E-modulus for Aluminium fits well with the initial parts of both the ARB and ARB-175 samples.

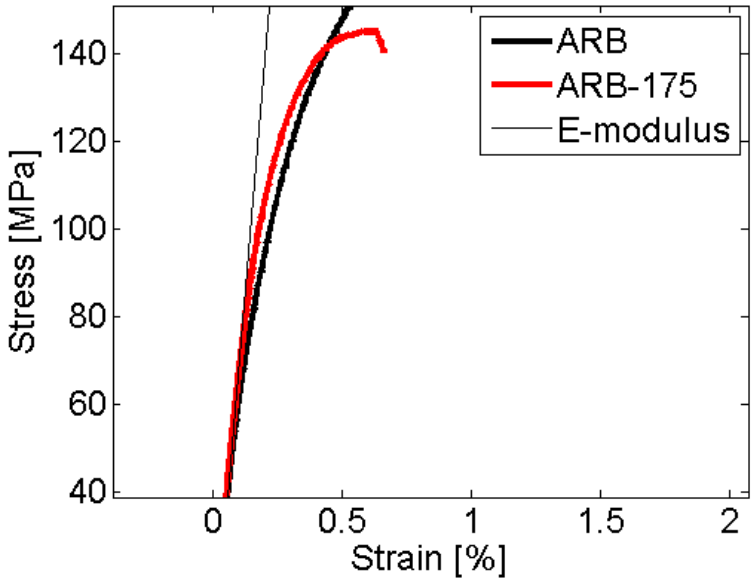

Figure 6.17: *Zoom of the initial region of stress-strain curves for the ARB and ARB-175 samples. The theoretical E-modulus of Al is shown by the slope of a thin straight line.*

The ARB-225 sample has a yield stress of approximately 98 MPa which was over two times higher than the CG1050 sample and below the ARB sample (135 MPa). The total elongation was restored and was almost 4 times larger than the ARB sample with 28% elongation. Similar observations have been reported (Kamikawa et al., 2009; Tsuji et al., 2002). The enhanced flow instability and premature failure in the samples annealed below 225°C was considered to be caused by the remaining high strength and due to the lack of mobile dislocations in the annealed structure (Huang,

2009).

6.3.2 Tensile stability enhanced by deformation

Huang et al. (2006a) has preliminarily investigated the effect of additional cold rolling on the stability of tensile deformation of as-processed nano-structured 99.2% pure Al and the results they obtained have shown that a cold rolling to a 15% thickness reduction made the tensile deformation more stable, generating a small decrease in strength and an increase in the total elongation by about 5%. In this study, a much wider range of P-P rolling reduction (up to 50% thickness reduction) was applied to as-ARB processed 1050 Al (99.5% pure). As mentioned in Section 6.2 in this chapter, the UTS decreased slightly with P-P rolling up to 30%, followed by a slight increase after 50% cold rolling. However the UTS did not reach the level of the ARB sample even after 50% P-P cold rolling. The tensile elongation showed a monotonic increase with increasing rolling strain up to 50%. The strain mapping analysis for the 50% P-P cold rolled sample reveals that the early localization of tensile strain, as observed during a tensile test of the ARB sample, was completely suppressed (Fig. 6.14). Furthermore, a rather large homogeneous deformation even after the UTS was observed (Fig. 6.15). These results suggest that for the present material processed by ARB, the P-P cold rolling up to 50% is an effective approach to stabilize the tensile deformation and to obtain a good combination of strength and tensile ductility.

To investigate if the increased tensile ductility is caused by a change in the strain rate sensitivity, strain rate jump tests were performed to obtain the evolution of strain rate sensitivity during tensile deformation of the ARB sample and the ARB-CR50 sample. The results are shown in Fig. 6.18.

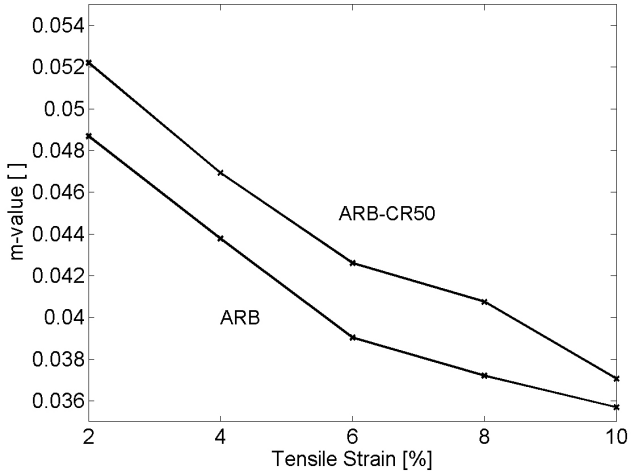

Figure 6.18: *Strain rate sensitivity exponent (m) from strain rate jump test and calculated for different tensile strain values for the ARB and ARB-CR50 samples.*

Fig. 6.18 shows that there was a slight increase in the m exponent after P-P 50% cold rolling, but the increase is not significant enough to state that this could be the only mechanism to lead to the increased tensile elongation.

6.3.2.1 Annealing followed by deformation

Following the observation of a positive effect of P-P cold rolling on the tensile stability, it would be interesting to investigate if such an effect is also applicable to the low temperature annealed samples that show enhanced tensile instability after annealing.

6.3.2.1.1 ARB-175-CR

Using samples annealed at 175°C for 30 minutes as starting material, 0, 5, 15, 30 and 50% cold rolling reductions were applied. These cold rolled samples are named ARB-175, ARB-175-CR5, ARB-175-CR15, ARB-175-CR30 and ARB-175-CR50.

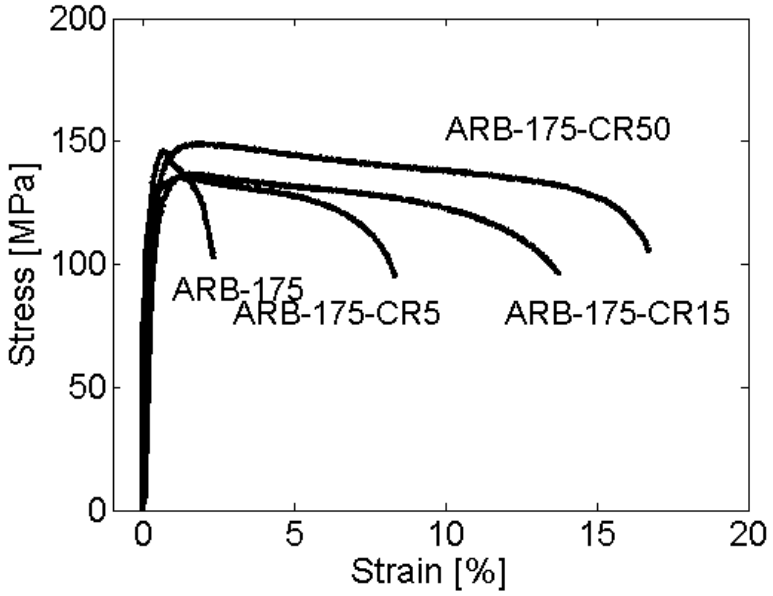

Figure 6.19: *Tensile engineering stress-strain curves for ARB annealed at 175 C for 30 minutes and subsequently post-process rolled from 0 to 50%.*

Fig. 6.19 shows the tensile curves for the ARB annealed at 175°C for 30 minutes and subsequently post-process rolled from 0 to 50% and in Table 6.9 the tensile data are extracted. Three samples were tested for each condition. All three samples of the ARB-175-CR30 experience necking at or outside of the knife of the extensometer. This did not allow the total elongation to be correctly measured and therefore the data for the 30% cold rolled sample are ignored in the following analysis. The results show that the cold rolling applied has a remarkable effect in restoring the tensile stability and ductility.

6.3.2.1.2 ARB-225-CR

It is well known that a Lüders band formation and propagation is detrimental to metal forming. Previous studies on low-carbon steels, which show Lüders banding, have shown that the formation of Lüders bands can

Table 6.9: Tensile data from the nominal stress-strain curves for the ARB annealed at 175°C for 30 minutes and subsequently P-P cold rolled from 0 to 50% reduction samples.

	Yield stress [MPa]	UTS [MPa]	Uniform elong. [%]	Total elong. [%]
ARB-175	135	143	0.7	2.4
ARB-175-CR5	126	135	1.3	8.6
ARB-175-CR15	105	136	1.9	15
ARB-175-CR30	123	143	1.6	-
ARB-175-CR50	125	149	1.8	18

be removed with a slight rolling termed temper rolling or skin pass rolling Kalpakjian and Schmid (2004).

The samples for this investigation were taken from a different batch of ARB sheets that was annealed under the same conditions (225°C, 30 minutes). The new ARB-225 sample showed a slightly different strength and elongation, but the upper and lower yield points were reproduced, as seen by a close examination of Fig. 6.20.

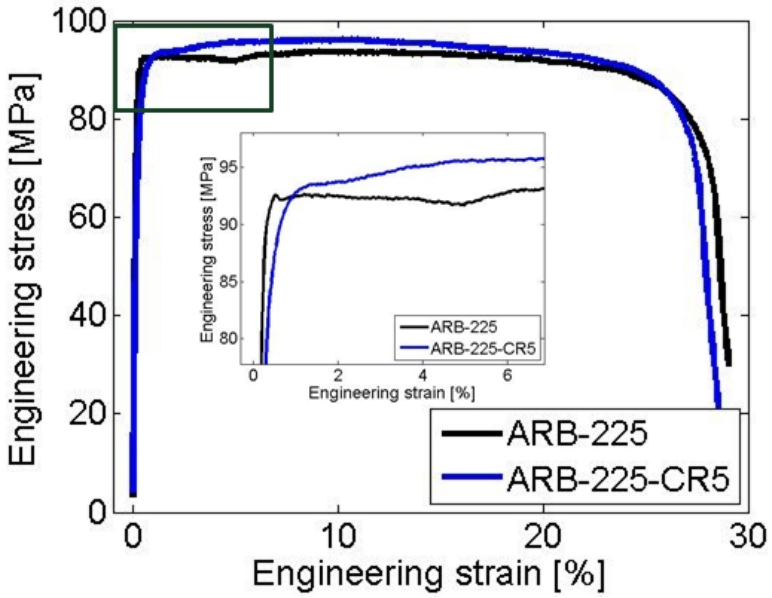

Figure 6.20: *Stress-strain curves for ARB-225 showing Lüders band formation and propagation and the ARB-225-CR5 sample were the Lüders band has been removed by a slight rolling*

Therefore, the present study explored if the Lüders banding phenomenon in the fine structured Al can also be removed by a slight deformation. After the annealing the samples are provided to 5% additional deformation by cold rolling (ARB-225-CR5), the yield point phenomenon disappears in the tensile stress-strain curve, as shown in Fig. 6.20. Finally it should be pointed out that the yield drop in the ARB-225 sample is rather small and no significant effect was noticed of the forming tests, which will be addressed later.

By Huang (2009), the Lüders band was also removed by a slight rolling of 5% for a 99.2% pure aluminium produced by six cycles of ARB and subsequently annealed at 250°C for 30 minutes. Fig. 6.20 showed that the slight rolling removes the Lüders strain but also introduces a slight strengthening which was not seen in Huang (2009). To investigate if the Lüders band was completely removed by the slight rolling a strain evolution analysis by ARAMIS was performed.

Fig. 6.21(a) shows the locations where the strain distribution maps are taken. Fig. 6.21(b) shows the strain distribution map (D1) after 3% tensile strain which is below the Lüders strain found in the ARB-225 sample. This strain distribution shows that there is a small heterogeneity in strain over the gauge length observed as the yellow color in the bottom of the gauge. This small heterogeneity was not seen in any of the other ARB-225-CR5 samples tested with ARAMIS. If this small heterogeneity is ignored the gauge length is nearly homogeneous with only very small changes. The strain distribution (D2) in Fig. 6.21(b) shows the necking behavior of the ARB-225-CR5 sample. It is observed that the entire gauge length deforms with most of the gauge length having a strain around 30% (yellow color) and the local necking region having a strain of over 40% (red color).

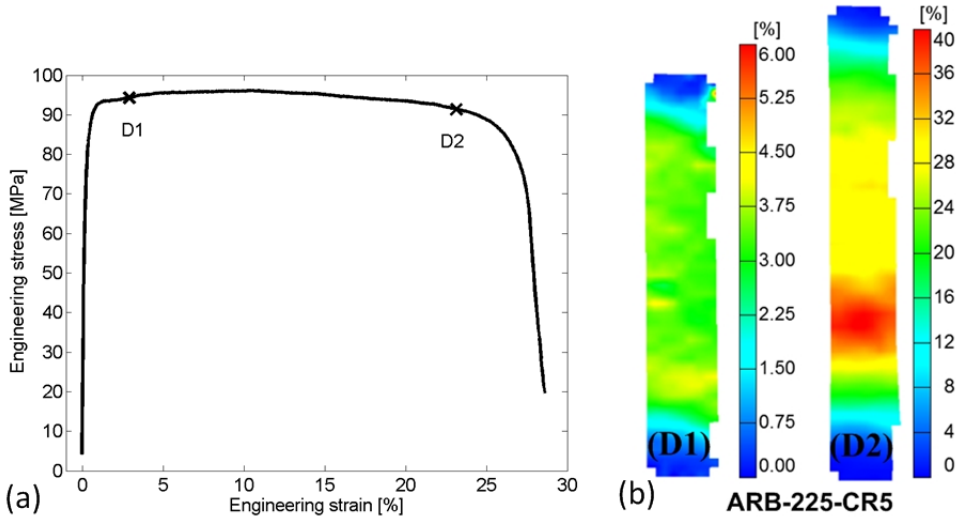

Figure 6.21: *(a) The stress-strain curve where the crosses indicate the positions, D1 and D2, of the strain distributions. (b) Strain distribution maps for analysis of the ARB-225-CR5 sample showing homogeneous strain distribution at 3% tensile strain and necking induced strain concentration at 23% nominal tensile strain.*

Fig. 6.22 shows the width strain analysis done on the ARB-225-CR5 sample and it can clearly be seen that the 5% thickness reduction by cold rolling removes the Lüders strain. The black line (1) which develops into the necking region later had a small offset in strain at a very early stage of the test. This offset did not really increase before the UTS. There are several percent of elongation after the UTS where only small differences in the width strain are observed between the lines analyzed. At the end of the test (around 20% tensile strain) the width strain at line 1 rapidly increases.

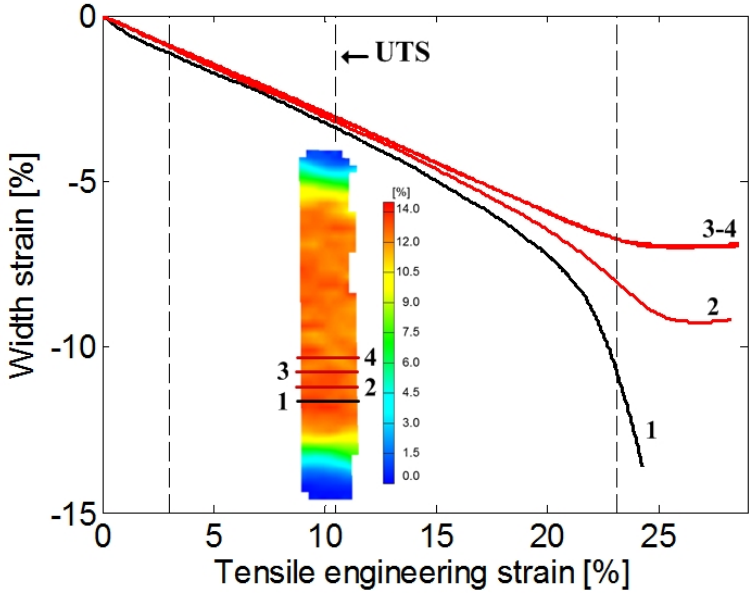

Figure 6.22: *The ARB-225-CR5 sample showing no Lüders band and a nearly homogeneous deformation.*

6.4 Summery

Taking the 6 cycle ARB processed material as an initial material, P-P treatments by either annealing or by deformation have been applied to seek a route to modify the structure and optimize the tensile properties. Several important observations were obtained, and a general approach involving P-P deformation to achieve an improved combination of strength and ductility is identified.

1. The P-P annealing was conducted at temperatures up to 225°C. Two types of annealing enhanced tensile instabilities were observed: samples annealed at lower temperatures (225°C) show a steep drop in flow stress and rapid failure: samples annealed at 225°C exhibit a yield point phenomenon that is associated with a complete tensile deformation process initiated by a small yield drop, followed by Lüders band propagation

(5% Lüders strain) and then a mild work hardening stage.

2. The P-P deformation was carried out by cold rolling up to 50% thickness reduction. Small changes in the strength were observed for all P-P deformed samples but a monotonic increase in the tensile ductility with rolling strain was obtained. The tensile elongation was increased from 7.5% of the as-ARB processed sample to 17% after 50% P-P cold rolling.
3. The positive effect of P-P cold rolling was then explored in the low temperature annealed samples that show enhanced tensile instabilities. For samples annealed at 175°C, P-P cold rolling up to 50% showed a significant effect in restoring the tensile stability and a total elongation of about 17% was also obtained after 50% cold rolling. For the sample annealed at 225°C, after cold rolling 5%, the original yield drop and Lüders straining were completely removed. This annealed and cold rolled sample showed a yield strength three time higher than that of a coarse grained state and at the same time a comparable tensile elongation to the coarse grained sample.

Chapter 7

Effects of post-process treatments on the formability of nanostructured Al

In the previous two chapters the ARB and the three optimized conditions (ARB-225, ARB-225-CR5 and ARB-CR50) have been investigated structurally and mechanically. This chapter will evaluate the formability of these four conditions and also two others which are presented subsequently.

7.1 Bulge test

If nanostructured metals are to be developed from scientific materials and gain industry acceptance, their formability needs to be evaluated. Several studies have been made regarding uniaxial tension tests showing that nanostructured metals perform poorly. Other strain paths like plane strain and biaxial stretching may result in better performance for nanostructured metals. Instead of testing for each operation at a time, forming limit dia-

grams that present the formability for every linear strain path are preferred. To evaluate the formability of nanostructured aluminium, bulge test were performed as described in Section 4.1.1. Six material conditions have been tested.

- CG1050
- ARB
- ARB-225
- ARB-225-CR5
- ARB-CR50
- CG-CR50

CG1050 was the starting material and is added as a reference material to the analysis to see what happens to the formability after ARB processing. ARB was the material processed using 6 cycles of ARB and ARB-225, ARB-225-CR5 and ARB-CR50 were the three materials with improved mechanical properties, believed to increase formability. CG-CR50 was a CG1050 that was homogeneously cold rolled 50% to see if ARB processing has any advantages compared with conventional rolling. The tensile data from the CG-CR50 sample are shown in Table 7.1.

Table 7.1: Tensile data from a CG1050 that was homogeneously cold rolled 50% (subsequently named CG-CR50).

	Yield stress [MPa]	UTS [MPa]	Uniform elongation [%]	Total elongation [%]
CG-CR50	118	122	1.2	8.2

7.1.1 Lüders band observation

Before the raw data from the experiments are discussed, the issue of the Lüders band in the ARB-225 samples is addressed. It is important to evaluate whether this issue has any influence on the formability compared with

the data from ARB-225-CR5.

Fig. 7.1 show the magnitude of the major strain before the onset of a localized neck as a function of the minor strain in the sheet surface. The experimental results from the ARB-225 (black crosses) and ARB-225-CR5 (blue crosses) samples are presented in Fig. 7.1(c). No significant difference between the black and blue data points were seen. There were also no visible signs of any Lüders strain on the samples. Therefore the samples were further regarded as one condition named ARB-225 to improve the statistics.

7.1.1.1 Discussion of the raw data

The raw data from the experiments for all the remaining four conditions can be seen in Fig. 7.1(a-e).

This is the raw-data and the scale was kept the same for easy comparison. At a first glance only the ARB-225 samples have similar forming abilities as the CG1050. All the deformed samples show poor forming abilities. For simplification the plots are discussed in terms of three strain paths: uniaxial tension, plane strain and biaxial stretching. Uniaxial tension has been treated in depth in Chapter 5 and it is clear that the performance is poor in this mode. This chapter therefore focuses on plane strain and biaxial stretching.

Following the plane strain path (shown in Fig. 4.12) in Fig. 7.1 it once again shows that only the ARB-225 sample nearly matches the formability of the CG1050. Following the balanced biaxial strain path is more difficult because the experiments only have small minor strain values and lie some

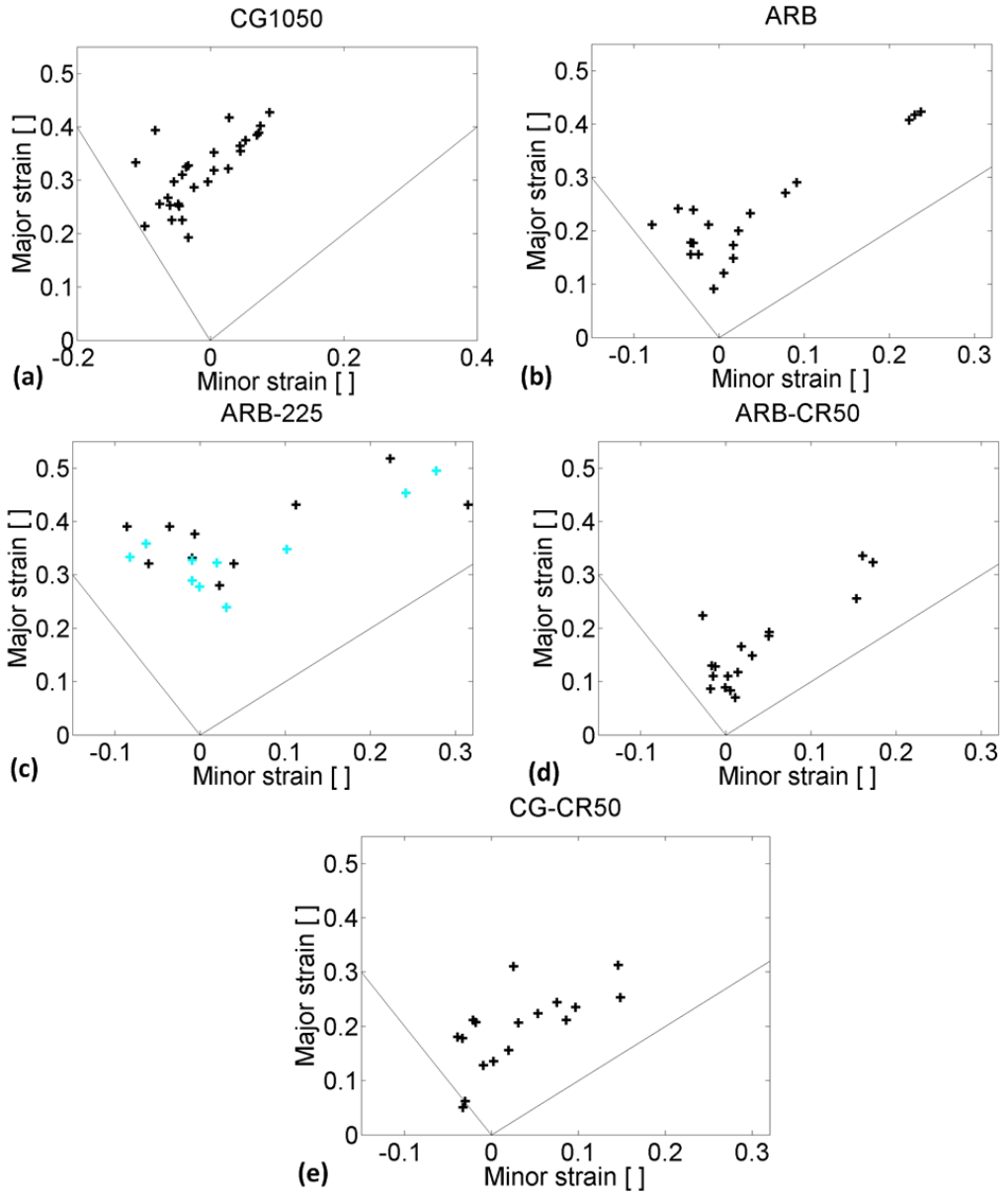

Figure 7.1: *Experimental raw data from the bulge test for (a) CG1050, (b) ARB, (c) ARB-225, (d) ARB-CR50 and (e) CG-CR50.*

distance away from the balanced-biaxial line (shown in Fig. 4.12). In the ARB condition there may be indications that the biaxial region exhibits better formability than seen in uniaxial tension and plane strain. To make

the comparison easier, a computation of the FLC by means of the Swift theory was explored.

7.1.2 Swift theory

Swift theory is a formulation of a plastic instability criteria and was presented by (Swift, 1952). This theory has been used to characterize various metals and alloys. In the present study it will be used to construct forming limit curves (FLC).

The value x seen in Eq. 7.1 is the proportionality factor between the principal stresses σ_x and σ_y in biaxial tension and is given as a function of the experimental strains and the planar anisotropy in Danckert (1989).

$$x = \frac{\sigma_y}{\sigma_x} = \frac{R * \epsilon_x + (1 + R) * \epsilon_y}{(1 + R) * \epsilon_x + R * \epsilon_y} \tag{7.1}$$

The effective flow stress (σ) can be expressed using a power law function dependent of the equivalent strain (ϵ) which is given by:

$$\sigma = C * (b + \epsilon)^n \tag{7.2}$$

where C is the strength coefficient, n is the strain hardening exponent and b is the pre-strain. If x is assumed to be constant under the entire test, the major and minor strains as a function of anisotropy (R) can be given by (Rees and Power, 1994; Hwang et al., 2009):

$$\epsilon_{Minor} = \frac{(1 + R) - R * x}{\sqrt{1 + R} * \sqrt{1 + R - 2 * R * x + x^2 + R * x^2}} * \bar{\epsilon}^P \tag{7.3}$$

$$\epsilon_{Major} = \frac{(1 + R) * x - R}{\sqrt{1 + R} * \sqrt{1 + R - 2 * R * x + x^2 + R * x^2}} * \bar{\epsilon}^P \tag{7.4}$$

$$\bar{\epsilon}^P = Z * n - B \tag{7.5}$$

where Z is the sub-tangent expressed as:

$$Z = \frac{\sqrt{1+R} * [1 + R - 2 * R * x + x^2 + R * x^2]^{3/2}}{(1+R)^2 - (2+R) * R * x^2 + (1+R)^2 * x^3} \tag{7.6}$$

Additionally to the experimental data there are three special cases which are:

- Uniaxial tension
- Plane strain
- Biaxial stretching

Using the generally taken stress or strain assumptions for these three cases the values in Table 7.2 are found and visualized in Fig. 7.2 under the assumption that R=1 and b=0.

Table 7.2: The Swift theory applied to the three special cases, uniaxial tension, plane strain, balanced biaxial stretching under the assumption that R=1 and b=0.

	Uniaxial tension	Plane strain	Balanced biaxial stretching
Stress/strain state	$\sigma_1 \neq 0, \sigma_2 = 0, \sigma_3 = 0$	$\epsilon_y = 0$	$\sigma_1 \neq 0, \sigma_2 \neq 0, \sigma_3 = 0$
x	0	$\frac{R}{(1+R)}$	1
Z	1	1.15	2
ϵ_{Minor}	$-\frac{n}{2}$	0	n
ϵ_{Major}	n	n	n

This theory and special cases will be used to calculate the forming limit curve starting with the CG1050.

7.1.3 Applying Swift

The fitted n, b and k values from the power law in Eq. 7.2 where b and n are using in the Swift theory are found used the plug-in, Ezyfit, for MATLAB. Fig. 7.3(a) shows this fit for the CG1050 sample which coincides very well with the experimental data. Fig. 7.3(b) shows the fit of the ARB sample which gives a very bad representation of the experimental data for strains

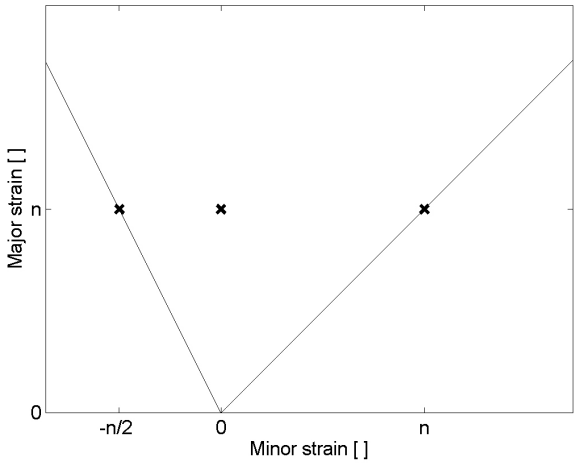

Figure 7.2: *A visualization of the theory applied on the three special cases, uniaxial tension, plane strain, balanced biaxial stretching under the assumption that R=1 and b=0.*

larger than 0.5%. Note that the necking behavior from the true stress-strain curves have been removed before fitting.

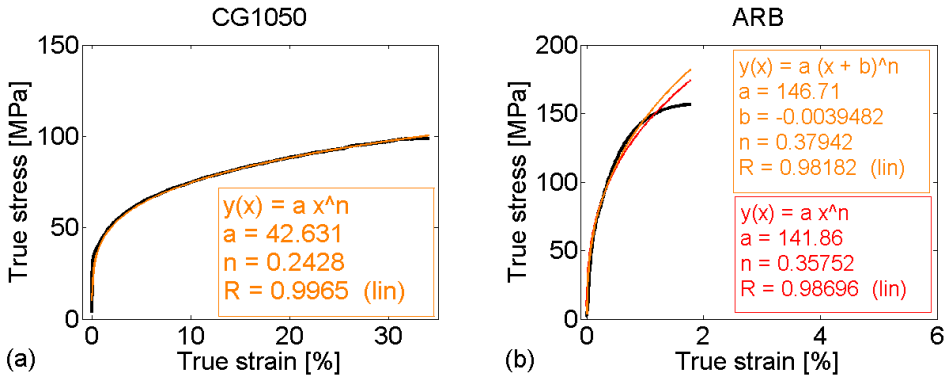

Figure 7.3: *True stress-strain from the experimental data and power law fitted curves. (a) for the CG1050 sample and (b) for the ARB sample. Note that the scales are not alike.*

The mean R-value for the CG1050 is close to 1 (1.08) and fitting the power law in Eq. 7.2 for the true stress-strain curve of the CG1050 gives a n value of 0.24 and a b value of zero. Using these values and the Swift theory

a FLC for the CG1050 can be computed which matches the negative minor strains reasonably well, but not the biaxial region as shown in Fig. 7.4. The black points are the original experimental data while the green points are the computed values. The red points are the three special cases, i.e, uniaxial tension, plane strain, balanced biaxial stretching from the computation. Since the biaxial region is the only area that shows any indication of noticeable formability for the nanostructured materials, the Swift theory cannot be used directly to compute the FLC. The Swift theory has also been computed for the other conditions with the same poor representation of the biaxial region which were expected due to the bad representation seen in Fig. 7.3(b).

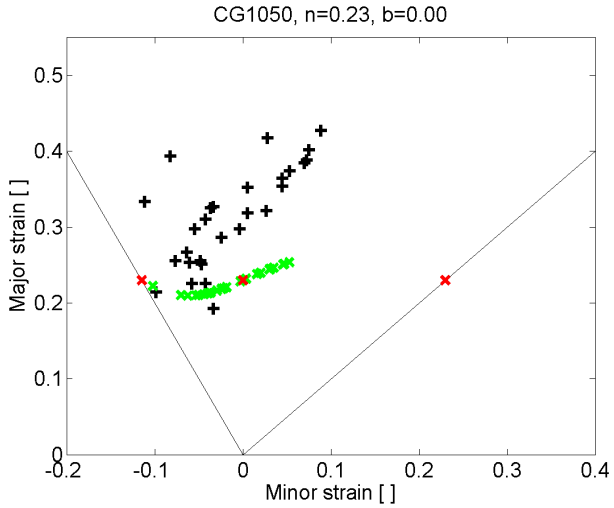

Figure 7.4: *The Swift theory applied on the CG1050 raw data where it can be seen that the forming limit curves gives a poor representation of the biaxial stretching region*

Other methods do exist to calculate the FLC but due to the complexity and limited time, the Swift theory will be used to fit the best possible FLC using n and b as fitting parameters. The fitting was carried out by trial and error with focuses on the positive minor strain region. In this way the

data are extrapolated in a systematic manner from the plane strain region and all the way to the balanced biaxial region. The fitted curve lies near the minimal major strain values of the experimental data (lower envelope) so that the curve will separate the failure and safe regions.

7.1.4 Fitting

The result of the fittings for all conditions can be seen in Fig. 7.5(a-e).

The n and b values for each condition can be seen in the title of the plots. These values no longer have any physical meaning but are only fitting parameters.

7.1.5 Forming limit diagram

Even though experimental acquisition of the full FLC was not possible as initially expected, the FLC fitted as described above based on the Swift approach appear to be in good agreement with the lower envelope of the full range of available experimental data for all five conditions. These are presented in Fig. 7.6. The crosses seen in Fig. 7.6 represent the experimental minor strain values plotted against the fitted major strain values. As an indication of how far into the biaxial region the experimental data reach, the crosses mark the fitted major strain values corresponding to the experimental minor strain data.

Again here for simplification the discussion of the plot is divided into two strain paths: plane strain and biaxial stretching. Following the strain path of plane strain along the y-axis shows the conditions can be divided into two groups: 1050 Al and ARB-225 showing good plane strain forming capabilities ($\epsilon_{major} > 0.25$) and ARB, ARB-CR50 and CG-CR50 only showing poor plane strain forming capabilities ($\epsilon_{major} < 0.2$). Following the balanced bi-

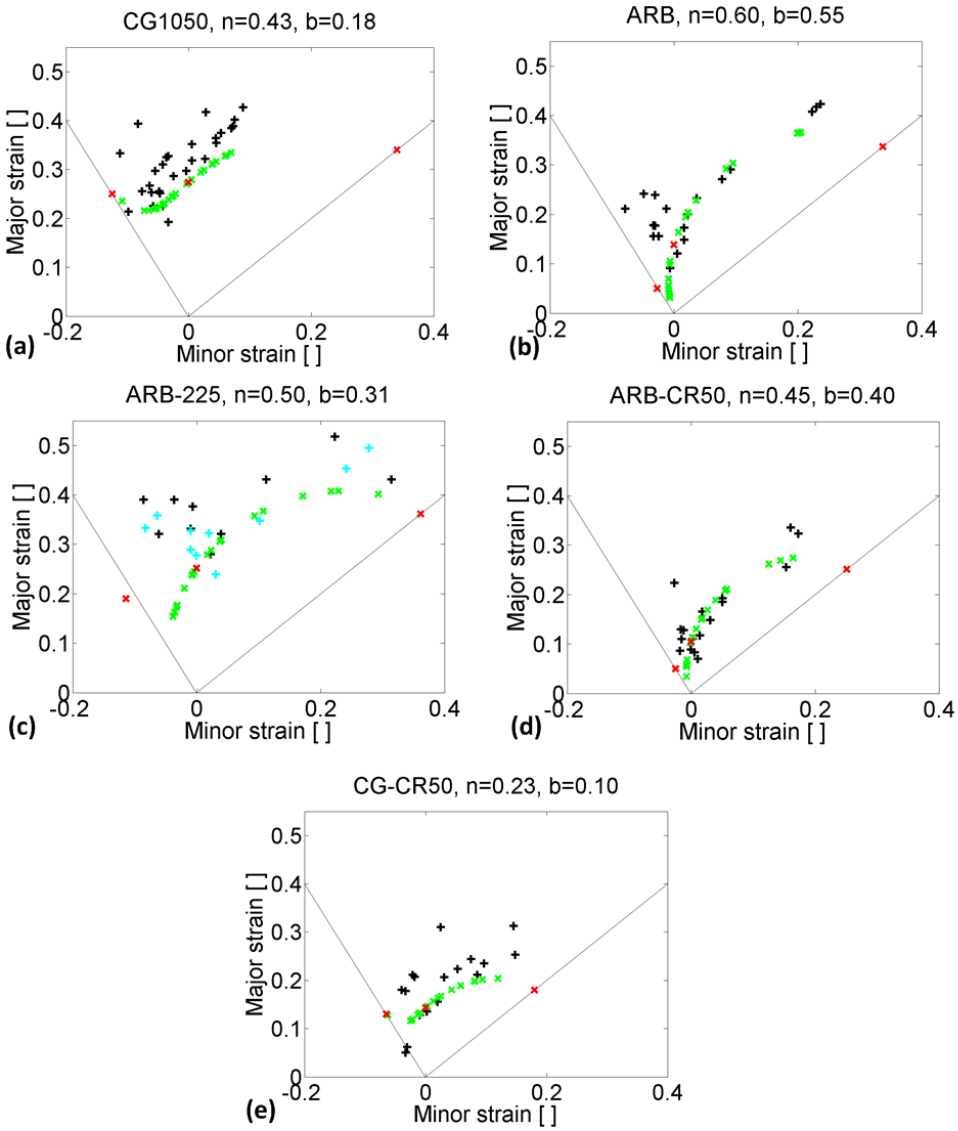

Figure 7.5: *Experimental raw data from the bulging test where the Swift theory for the FLC has been fitted to match the biaxial stretching region as good as possible for (a) CG1050, (b) ARB, (c) ARB-225, (d) ARB-CR50 and (e) CG-CR50. The fitting parameters n and b are given in the title.*

axial strain path reveals several surprising observations. The ARB condition shows nearly the same formability ($\epsilon \approx 0.35$) as the CG1050 and ARB-225 conditions while both ARB-CR50 and especially CG-CR50 only show poor formability ($\epsilon \leq 0.25$). The crosses on the black line (balanced biaxial) are

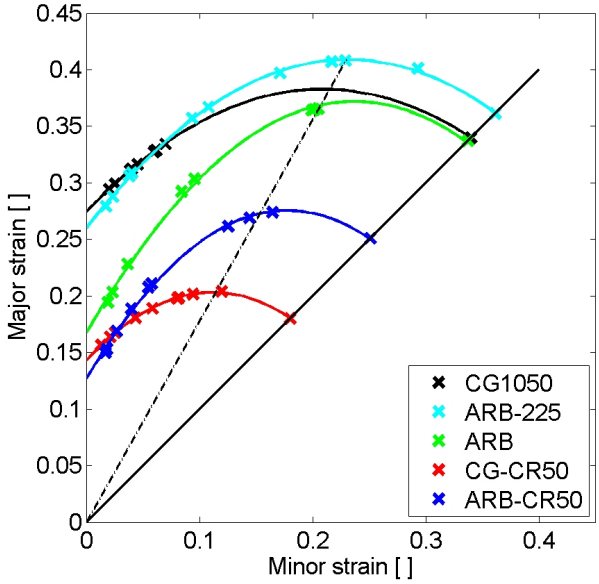

Figure 7.6: *Forming limit diagram of the positive minor strain values with the forming limit curves fitted with the Swift theory for all the conditions. The crosses on the black line (balanced biaxial) are the theoretical special case points found in Table 7.2. The dotted black line shows the empirical limit to the obtained data point from the experiments.*

the ones calculated as the special case of balanced biaxial stretching. For all conditions except for the CG1050 condition the experimental data reach well into the biaxial region but equibiaxial stretching was not achieved in any of the experiments. The dotted black line marks the approximate end of the experimental region. It is seen that the conclusions made for the extrapolated equibiaxial case are also valid for $\epsilon_{major} \approx \frac{1}{2}\epsilon_{minor}$.

7.2 Discussion of the forming limit diagram

In Fig. 7.7 the experimental data for the CG1050 sample are shown together with data from Skjødt et al. (2010) and Mishra et al. (2009) who have made forming limit diagrams for the same alloy, all in 1 mm thick specimens.

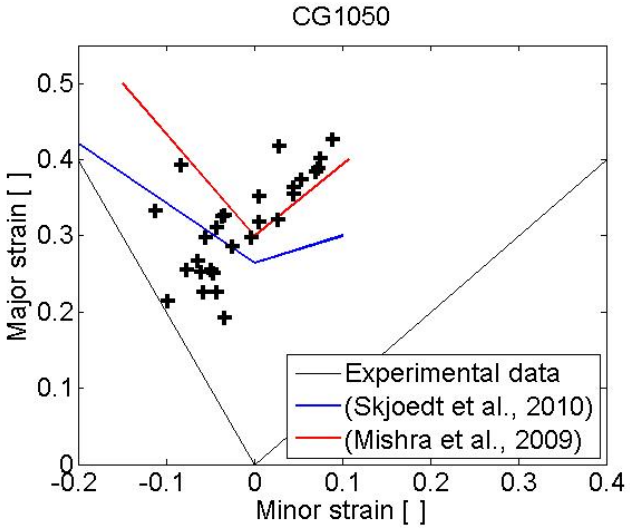

Figure 7.7: *Experimental data points compared with data from Skjødt et al. (2010) and Mishra et al. (2009)*

It can be seen that the positive minor strain values fit well with the red line but the negative minor strain values do not fit with any of the curves very well. It should also be emphasized that there are some significant differences between the results from Skjødt et al. (2010) and Mishra et al. (2009) which indicate that it is difficult to compare experiments done on different equipment. Since the present study is a comparison between different conditions all tested on the same equipment any process influence is assumed to be the same on all specimens. It should also be emphasized that Skjødt et al. (2010) and Mishra et al. (2009) do not extend further into the region of biaxial stretching.

There were no significant difference between the formability of the ARB-225 and ARB-225-CR5 samples or no visible signs of uneven deformation on the samples. In Hutanu et al. (2005) and Ananthan and Hall (1991) a gauge length over thickness ratio was described where single slip bands

were more likely to occur the higher this ratio is. This was also seen in the present studies when the sample geometry was changed, as described in Section 4.1.3.2. The thickness was not changed but the gauge length was reduced from 16 mm to 8 mm and then no Lüders bands were observed in any of the three in-plane directions tested. The samples with the smallest width were tested in a stress state close to uniaxial tension and not entirely in a pure uniaxial state. If this or the gauge length issue is the reason why Lüders bands are not observed is not fully understood.

The poor performance with respect to FLC prediction of the Swift theory using n and b parameters derived from experimental stress-strain curves instead of fitted values was also observed in Bleck et al. (1998) for several different steels. They relate the discrepancies to a lack of understanding of the flow behavior, material parameters and experimental factors. The CG1050 sheet is a well studied material with a known flow behavior and material parameters. It was demonstrated in Section 5.3.1 that the CG1050 sheet is virtually isotropic which is a basic assumption in the Swift theory. The origin of the poor performance of this theory for CG1050 has not been found. Planar anisotropy is, however, likely to play a role for the other material conditions.

The CG-CR50 sheet was included to investigate if the ARB processing had any advantages compared to conventional rolling. In biaxial tension the ARB sheet is definitely better than the conventional cold rolled material both when considering the formability and the expected final strength.

It was believed that the enhanced post-UTS elongation of the ARB-

CR50 would increase the formability of this condition. This was not seen but it could also relate to the difference in sheet thickness (ARB=1 mm and ARB-CR50=0.5 mm). It is commonly believed that the formability increases with increasing thickness (Raghavan, 1995).

The ARB-225 sheet actually shows better formability in Fig. 7.6 than the CG1050 sheet. This is, however, likely to be due to the fitting because all the experimental data points were below 0.1 minor strain for the CG1050 sheet and only the theoretical balanced biaxial point is above. In Bleck et al. (1998) it was also observed that CG1050 "only" exhibits low minor strain values. It was believed that this was due to process parameters like friction. To investigate this and get a better understanding of the biaxial region Erichsen tests were performed.

7.3 Erichsen test

The Erichsen tests were performed as described in Section 4.2.1. The results for the same five conditions (similar as in Fig. 7.6) are shown in Fig. 7.8. Since the Erichsen test is a simpler test where only the dome height (Erichsen index) was measured, it is not directly comparable to the FLD but the distance along the dotted black line in Fig. 7.6 was measured and normalized to have a frame of reference. In the Erichsen tests it is clearly seen that the CG1050 performs best of the five conditions while this was not seen in Fig. 7.6 where the ARB-225, CG1050 and ARB conditions have approximately the same formability.

Fig. 7.8 again shows that the ARB-225 and ARB sample are close to each other with a slightly better EI for the ARB-225 sample. Here there

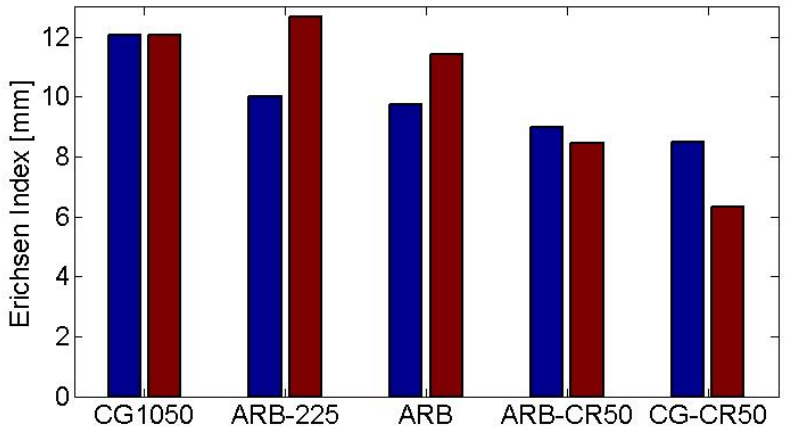

Figure 7.8: *The blue columns are the Erichsen test results measured in the Erichsen Index mm for all the conditions. The red columns are normalized distance along the dotted line in Fig. 7.6 which was the limit of the expeirmental data. They were normalized so that CG1050 has the same length as the Erichsen index.*

is a relatively large difference from the CG1050 to the ARB-225 which was also initially expected but not seen in the red columns. The ARB-CR50 and CG-CR50 also have nearly the same EI and relatively close to the ARB sample. However, it should be emphasized that the nanostructured conditions (ARB, ARB-225 and ARB-CR50) all have a better formability than the CG-CR50. The formability of the nanostructured metals cannot match the CG1050 but the nanostructured metals will have a higher strength than the coarse grained starting material even though this is also hardened during deformation.

To do further analysis of the influence of the enhanced post-UTS elongation and its effect on the formability, nanostructured sheets in three thickness have been made.

7.3.1 Thickness effect

Nanostructured sheets produced by 6 cycles of ARB of 0.5, 1 and 2 mm in thickness have been produced without changing other ARB processing parameters than the spacing between the rolls. To obtain these three ARB sheet thicknesses starting materials of similar thickness are required. The raw material was bought as 1 and 2 mm sheets to have the opportunity to produce thicker ARB sheets. To have an additional initial thickness and to match the ARB-CR50 sample in 0.5 mm thickness two sheets 1 mm in thickness were rolled down to 0.5 mm and annealed for 5 hours at 500 °C to achieve a recrystallized structure as with the other sheets. The following conditions were made:

- CG1050 (1 mm)
  - CG1050 (1 mm)
  - ARB (1 mm)
  - ARB-225 (1 mm)
  - ARB-CR50 (0.5 mm)
  - CG-CR50 (0.5 mm)
- CG1050 (0.5 mm)
  - CG1050 (0.5 mm)
  - ARB (0.5 mm)
  - ARB-225 (0.5 mm)
  - ARB-CR50 (0.25 mm) - Was not made due to a thickness issue
  - CG-CR50 (0.25 mm) - Was not made due to a thickness issue
- CG1050 (2 mm)
  - CG1050 (2 mm)
  - ARB (2 mm)
  - ARB-225 (2 mm) - Was not made because all the nanostructured

sample should come from one single ARB sheet and as described in Chapter 3 the width of the sample in 1 mm thickness sheet was restricted by the force of the rolling mill. Consequently there was only material enough to test two conditions where ARB and ARB-CR50 were prioritized.

- ARB-CR50 (1 mm)
- CG-CR50 (1 mm)

The ARB processing was done as also described in Chapter 3. Erichsen tests are performed on these new sheets for the five conditions in different thicknesses.

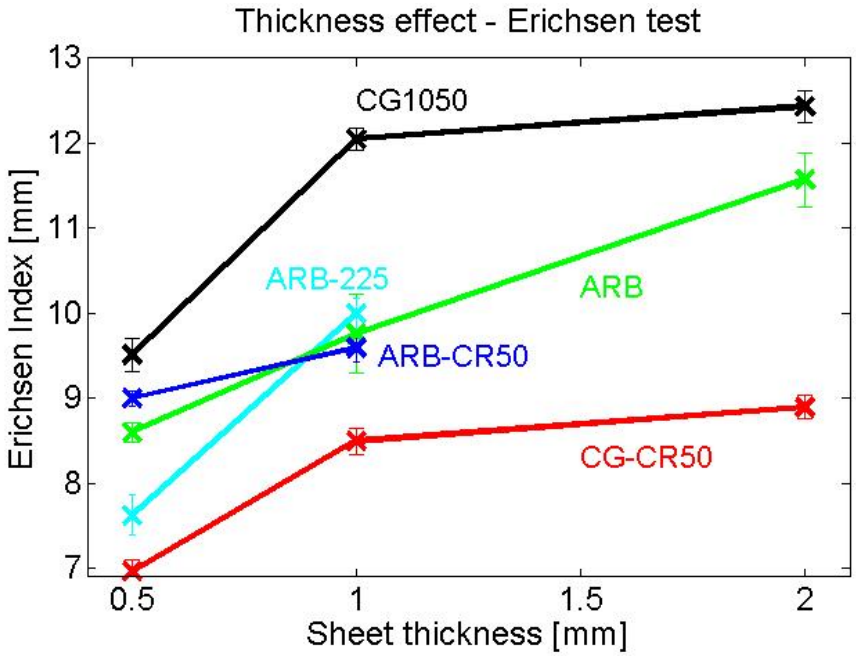

Figure 7.9: *Erichsen test results measured in the Erichsen index mm for all the conditions in different thicknesses*

The results of the experiments are shown in Fig. 7.9. The standard deviation from the 5 repetitions are shown at each point. The standard

variation is small compared to the variations between the different processing methods. The values for 1 mm were the same as seen in Fig. 7.8 except for the ARB-CR50 condition which was the 0.5 mm value. It can be seen that while the ARB condition is marginally better than the ARB-CR50 condition at 1 mm it was vice versa at 0.5 mm. The same was seen for the ARB-225 sample which performs well at 1 mm but has a quite poor result at 0.5 mm. On the other hand it was seen that the CG1050 sample achieves the best result in all thicknesses and CG-CR50 achieves the worst result in all thicknesses.

7.4 Discussion of the Erichsen tests

In Fig. 7.9 it is clearly seen that CG1050 and CG-CR50 have the best and the worst formability, respectively, in all thicknesses. Likewise it can be seen that the formability improves when the thickness of the sheet is increased. The nanostructured conditions (ARB, ARB-225 and ARB-CR50) in 1 mm sheet have EI very close to each other while the difference becomes larger between the nanostructured conditions in 0.5 mm sheet and the ranging changes compared to the results at 1 mm.

Comparing these results in biaxial stretching to the results in uniaxial tension where the total elongation of the ARB sample was 7.5% while the total elongations for the CG1050 was in the range of 40-50% it would not have been expected that the ARB sample performs so well in biaxial stretching. Typically it is believed that the total elongation of a material can be seen as a measurement of its formability as well. This is also the case for the CG1050 but not for nanostructured metals which only preform well in

biaxial stretching.
In Yoda et al. (2011) it was indicated that nanostructured materials perform better in biaxial stretching than uniaxial tension. This was definitely confirmed here where both in the FLD and in the EI the ARB-225 and ARB samples performs nearly as well as the coarse grained metal.

For the thickness effect still some questions were left unanswered. One reason for the inconsistent results in the nanostructured and annealed conditions (ARB, ARB-CR50 and ARB-225) could be due to the change in l/h ratio (see Eq. 3.1) as the thickness of the sheet is changed. The sheets of 0.5, 1 and 2 mm in thickness have a l/h indices of 12.3, 8.7 and 6.1 respectively. Specially the thick sheet with a l/h index of 6.1 has a value relatively close to the homogeneous rolling range of 0.5 to 5. This could affect the texture or the bonding strength of the ARB processing. Jamaati and Toroghinejad (2011) report that the most important factor for the bond strength was the amount of reduction. Since all the ARB processing has the same reduction (50%) this cannot be the answer but they also indicate that by increasing the reduction more virgin material was welded together due to more cracks in the bonding layer. Another factor which is not investigated is the draught through the rolling mill that could also influence the bonding. 6 cycles of ARB gives 64 layers of the original sheet that only gives a layer thickness of $8\mu m$ in the thinnest sheet. This could result in the amount of virgin aluminium was limited compared to the thicker sheets which could explain the difference in performance as the thickness of the sheets are changed. In Fig. 5.4 the bonding layer from one of the ARB cycles can be seen and has a maximum thickness of 3.6 μm and without having studied the oxide layer in depth it can be concluded that the amount

of virgin aluminium in the thinnest ARB sheet must be limited. Further investigations of ARB processing in different thicknesses, mechanical properties and a total characterization of the initial structure is needed to fully understand this inconsistency in the Erichsen results. Tensile tests of the different sheets were conducted but due to a misunderstanding during testing the results had to be disregarded.

If nanostructured metals have to gain industry acceptance their mechanical properties from batch to batch has to be studied even further to understand how even small variations in ARB processing can affect the final ARB sheet properties. Additionally an up scale in production is needed to produce sheets in large dimensions and thicker sheets. It is believed that nanostructured metals have potential if they are used under full control of the strain paths. There must exist e.g. body car parts that are produced in biaxial stretching where nanostructured metals with advantages can be used, resulting in a stronger part or the use of thinner material for a lighter construction. If a compromise between strength and ductility is needed the ARB-225 or ARB-225-CR5 conditions could be a useful choice with more than twice the yield stress of the coarse grained metal and a ductility which is nearly as good. It all comes down to the production price of the nanostructured metals.

7.5 Summary

The formabilities in biaxial stretching obtained by the bulge tests and fitting of the Swift theory are not in complete quantitative agreement with the results from the Erichsen tests. However, qualitatively the results agree well in both methods where the ARB conditions are substantially better than

the conventionally rolled CG-CR50 condition. An overall comparison with the initial CG1050 material shows that the ARB conditions are somewhat less formable but the ARB conditions should possess a higher strength. However, ranking of the ARB conditions relative to each other in the biaxial region is inconclusive, probably due to an additional effect of the sheet thickness.

Chapter 8

Conclusions and outlook

The main aim of the present PhD study is to experimentally explore the potential of nanostructured aluminium in practical inductrial applications. In order to do so four goals have been fulfilled:

- Optimize processing of commercially pure aluminium (Al1050) to produce nanostructured metal sheets
- Apply post-process treatments in the form of thermal annealing and deformation to optimize the mechanical properties
- Conduct a detailed experimental investigation of the onset and evolution of strain localization
- Investigate the performance of the sheet metal produced using a wide range of standard formability tests other than uniaxial tension

This study has succeeded to increase the size of the nanostructured sheet produced by ARB from a typical width of less than 100 mm reported in the literature to 184 mm with a final length of 700 mm after 6 cycles of ARB processing. The sheets became sufficiently large for mechanical testing in other modes than uniaxial tension.

Based on the results of previous studies two post-processing routes to optimize the mechanical performance were explored. Post-processing by thermal annealing has given a good compromise between strength and ductility compared to the strong but brittle nanostructured metal. The yield stress is more than twice that of the coarse grained material and the total elongation is restored to around 28%, which is nearly four times larger than the nanostructured metal. The annealed condition showed a very small yield point phenomenon followed by a Lüders band formation and propagation to 5% tensile strain. This Lüders band could be removed by a slight rolling.

The post-process deformation by homogenous rolling showed that rolling reduction up to 50% gradually enhances the post-UTS elongation up to 17%. This was accompanied by a slight decrease both in the uniform elongation and tensile strength.

The tensile behavior of the samples was investigated in detail by use of the ARAMIS system which showed that the nanostructured sample, without any post-processing, developed local inhomogeneous deformations at very low strains, even before the UTS. This inhomogeneous strain further developed into a shear band with increasing tensile straining. Nearly all the deformation in the sample was concentrated in the shear band with local strain values reaching over 40% while the rest of the gauge part only experienced a strain of 2-3%. After 50% post-process deformation by rolling, no shear bands were observed and only very small inhomogeneities were observed before the UTS. However, these inhomogeneities did not develop furthermore before the very end of the tensile test in the form of neck-

ing. After the UTS a homogeneous post-UTS elongation was observed up to around 6% strain which is about four times larger than the elongation at the UTS. This homogeneous post-UTS elongation was followed by an intermediate region where non-localized necking was observed, but finally localized necking occurred.

In plane strain the ARB-225 condition showed a performance comparable to that of the initial CG-CR50 material while the ARB and ARB-CR50 resembled the conventional CG-CR50 condition.

In uniaxial tension the ARB samples without post-processing performed badly with a total elongation close to 8% which is similar to the conventional CG-CR50 condition. The samples which where post-processed by annealing or deformation performed substantially better but were still inferior to the initial CG-1050 material.
The performance in the uniaxial region can therefore clearly not be used as a measure for the general formability. The present study demonstrates beyond doubt that the ARB processed material perform much better in the biaxial region than in uniaxial tension. In particular the ARB processed material and the ARB-225 post-processed material show biaxial stretching capabilities close to that of the initial material while the ARB-CR50 performs slightly poorer but still better than CG-CR50.

For future work it could therefore be interesting to investigate the mechanical properties of these sheets to see how the changes in the l/h ratio in rolling affect the mechanical properties and the post-process treatments. Likewise a more detailed study of the structural evolution in biaxial ten-

sion could be helpful to fully understand why nanostructured metals perform well in this strain path when uniaxial tension only show poor results. Once again pointing out that it is fully established that nanostructured metals perform much better in biaxial tension than uniaxial tension which opens up for industrial applications for this strain path.

Bibliography

Ananthan, V. and Hall, E. (1991). Macroscopic aspects of lüders band deformation in mild steel. *Acta metallurgica et materialia*, 39(12):3153–3160.

Bay, N. (1979). Cold pressure welding - the mechanisms governing bonding. *Journal of Engineering for Industry*, 101:121.

Bay, N. (2010). *Cold welding*. Technical University of Denmark.

Beausir, B., Scharnweber, J., Jaschinski, J., Brokmeier, H. G., Oertel, C. G., and Skrotzki, W. (2010). Plastic anisotropy of ultrafine grained aluminium alloys produced by accumulative roll bonding. *Materials Science and Engineering: A*, 527(13):3271–3278.

Bleck, W., Deng, Z., Papamantellos, K., and Gusek, C. O. (1998). A comparative study of the forming-limit diagram models for sheet steels. *Journal of Materials Processing Technology*, 83(1):223–230.

Bochniak, W. (1995). Mode of deformation and the cottrell-strokes law in fcc single crystals. *Acta metallurgica et materialia*, 43(1):225–233.

Callister, W. D. and Rethwisch, D. G. (2007). *Materials science and engineering: an introduction*. John Wiley & Sons New York:.

Carreker, R. and Hibbard, W. (1953). Tensile deformation of high-purity copper as a function of temperature, strain rate, and grain size. *Acta Metallurgica*, 1(6):654–663.

Chen, J., Lu, L., and Lu, K. (2006). Hardness and strain rate sensitivity of nanocrystalline cu. *Scripta materialia*, 54(11):1913–1918.

Considere, A. (1885). Application of iron and steel in constructions. In *Annales des Ponts et Chaussees*, volume 9, pages 574–575.

Danckert, J. (1989). *Yield criteria and flow rule for anisotropy materials*. Institute for production, AAU.

Elmustafa, A., Tambwe, M., and Stone, D. (2002). Activation volume analysis of plastic deformation in fcc materials using nanoindentation. In *MRS Proceedings*, volume 750. Cambridge Univ Press.

Erbel, S. (1979). Mechanical properties and structure of extremely strain-hardened copper. *Metals Technology*, 6(1):482–486.

Goodwin, G. (1968). Paper no. 680093. In *SAE Automotive Engineering Congress, Detroit*.

Gray, G., Lowe, T., Cady, C., Valiev, R., and Aleksandrov, I. (1997). Influence of strain rate & temperature on the mechanical response of ultrafine-grained cu, ni, and al-4cu-0.5 zr. *Nanostructured Materials*, 9(1):477–480.

Hall, E. (1951). The deformation and ageing of mild steel: Iii discussion of results. *Proceedings of the Physical Society. Section B*, 64(9):747.

Hansen, N., Mehl, R. F., et al. (2001). New discoveries in deformed metals. *Metallurgical and materials transactions A*, 32(12):2917–2935.

Hausöl, T., Schmidt, C. W., Maier, V., Böhm, W., Nguyen, H., Merklein, M., Höppel, H. W., and Göken, M. (2012). Formability of ultrafine-grained aa6016 sheets processed by accumulative roll bonding. *Key Engineering Materials*, 1665(504):575.

Heason, C. P. and Prangnell, P. B. (2002). Texture evolution and grain refinement in al deformed to ultra-high strains by accumulative roll bonding (arb). In *Materials Science Forum*, volume 408, pages 733–738. Trans Tech Publ.

Hirsch, P. B., Howie, A., Nicholson, R., Pashley, D., and Whelan, M. J. (1965). *Electron microscopy of thin crystals*, volume 320. Butterworths London.

Hoffmann, H. and Hong, S. (2006). Tensile test of very thin sheet metal and determination of flow stress considering the scaling effect. *CIRP Annals-Manufacturing Technology*, 55(1):263–266.

Hoffmann, H. and Vogl, C. (2003). Determination of true stress-strain-curves and normal anisotropy in tensile tests with optical strain measurement. *CIRP Annals-Manufacturing Technology*, 52(1):217–220.

Hogström, P., Ringsberg, J., and Johnson, E. (2009). An experimental and numerical study of the effects of length scale and strain state on the necking and fracture behaviours in sheet metals. *International Journal of Impact Engineering*, 36(10):1194–1203.

Höppel, H., Staud, D., Merklein, M., Geiger, M., and Göken, M. (2008a). Formability of accumulative roll bonded aluminum aa1050 and aa6016 investigated using bulge tests. *Advanced Engineering Materials*, 10(12):1101–1109.

Höppel, H. W., Göken, M., et al. (2008b). Deformation behaviour of accumulative roll bonded and friction stir welded aluminium alloys. In *Materials Science Forum*, volume 584, pages 833–839. Trans Tech Publ.

Höppel, H. W., May, J., and Göken, M. (2004). Enhanced strength and ductility in ultrafine-grained aluminium produced by accumulative roll bonding. *Advanced engineering materials*, 6(9):781–784.

Huang, X. (2007). Characterization of nanostructured metals produced by plastic deformation. *Journal of Materials Science*, 42(5):1577–1583.

Huang, X. (2009). Tailoring dislocation structures and mechanical properties of nanostructured metals produced by plastic deformation. *Scripta Materialia*, 60(12):1078–1082.

Huang, X., Hansen, N., and Tsuji, N. (2006a). Hardening by annealing and softening by deformation in nanostructured metals. *Science*, 312(5771):249.

Huang, X., Kamikawa, N., and Hansen, N. (2008a). Property optimization of nanostructured arb-processed al by post-process deformation. *Journal of Materials Science*, 43(23):7397–7402.

Huang, X., Kamikawa, N., and Hansen, N. (2008b). Strengthening mechanisms in nanostructured aluminum. *Materials Science and Engineering: A*, 483:102–104.

Huang, X., Kamikawa, N., and Hansen, N. (2010). Strengthening mechanisms and optimization of structure and properties in a nanostructured if steel. *Journal of Materials Science*, 45(17):4761–4769.

Huang, X., Kamikawa, N., Tsuji, N., and Hansen, N. (2006b). correlation between texture and structure in high purity al processed by arb. *Ultrafine Grained Materials IV*.

Huang, X., Kamikawa, N., Tsuji, N., and Hansen, N. (2008c). Nanostructured aluminum and if steel produced by rolling-a comparative study. *ISIJ international*, 48(8):1080–1087.

Huang, X., Tsuji, N., and Pantleon, W. (2009). Strengthening mechanisms, flow instabilities and property optimization in nanostructured metals. In *30th Risø International Symposium on Materials Science: Nanostructured metals–Fundamentals to applications*, pages 59–80.

Hughes, D. and Hansen, N. (2000). Microstructure and strength of nickel at large strains. *Acta materialia*, 48(11):2985–3004.

Humphreys, F. (2004). Characterisation of fine-scale microstructures by electron backscatter diffraction (ebsd). *Scripta materialia*, 51(8):771–776.

Hutanu, R., Clapham, L., and Rogge, R. (2005). Intergranular strain and texture in steel lüders bands. *Acta materialia*, 53(12):3517–3524.

Hwang, Y.-M., Lin, Y.-K., and Chuang, H.-C. (2009). Forming limit diagrams of tubular materials by bulge tests. *Journal of Materials Processing Technology*, 209(11):5024–5034.

Isaev, N., Grigorova, T., and Zabrodin, P. (2009). Strain-rate sensitivity of the flow stress of ultrafine-grain aluminum at temperatures 4.2–295 k. *Low Temperature Physics*, 35:898.

Iwahashi, Y., Horita, Z., Nemoto, M., and Langdon, T. G. (1998). The process of grain refinement in equal-channel angular pressing. *Acta Materialia*, 46(9):3317–3331.

Jamaati, R. and Toroghinejad, M. (2011). Cold roll bonding bond strengths: review. *Materials Science and Technology*, 27(7):1101–1108.

Jong Bong, H., Barlat, F., Lee, M.-G., and Chan Ahn, D. (2012). The forming limit diagram of ferritic stainless steel sheets: experiments and modeling. *International Journal of Mechanical Sciences*.

Kalpakjian, S. and Schmid, S. R. (2004). *Manufacturing Engineering and Technology Machining*. Beijing: Mechanical Industry Press.

Kamikawa, N. (2006). *PhD Thesis*. PhD thesis, Osaka Univesity.

Kamikawa, N., Huang, X., Tsuji, N., and Hansen, N. (2009). Strengthening mechanisms in nanostructured high-purity aluminium deformed to high strain and annealed. *Acta Materialia*.

Keeler, S. P. (1968). *Circular grid system: a valuable aid for evaluating sheet metal formability*. Society of Automotive Engineers.

Kidmose, J., Lu, L., Hansen, N., Winther, G., and Huang, X. (2012a). Onset of strain localisation in nanostructured aluminium. *33th Risoe International Symposium and Material Science*, pages 265–270.

Kidmose, J., Lu, L., Winther, G., Hansen, N., and Huang, X. (2012b). Strain distribution during tensile deformation of nanostructured aluminum samples. *Journal of Materials Science*, pages 1–7.

Kim, H., Kang, S., Tsuji, N., and Minamino, Y. (2005). Elongation increase in ultra-fine grained al-fe-si alloy sheets. *Acta Materialia*, 53(6):1737–1749.

Lankford, W., Snyder, S., and Bauscher, J. (1950). New criteria for predicting the press performance of deep drawing sheets. *Trans. ASM*, 42:1197.

Laukonis, J. V. and Ghosh, A. K. (1978). Effects of strain path changes on the formability of sheet metals. *Metallurgical Transactions A*, 9(12):1849–1856.

Liu, Q., Huang, X., Lloyd, D., and Hansen, N. (2002). Microstructure and strength of commercial purity aluminium (aa 1200) cold-rolled to large strains. *Acta materialia*, 50(15):3789–3802.

Liu, Q., Juul Jensen, D., and Hansen, N. (1998). Effect of grain orientation on deformation structure in cold-rolled polycrystalline aluminium. *Acta materialia*, 46(16):5819–5838.

Lu, L., Li, S., and Lu, K. (2001). An abnormal strain rate effect on tensile behavior in nanocrystalline copper. *Scripta Materialia*, 45(10):1163–1169.

Ma, X., Lapovok, R., Gu, C., Molotnikov, A., Estrin, Y., Pereloma, E., Davies, C., and Hodgson, P. (2009). Deep drawing behaviour of ultrafine grained copper: modelling and experiment. *Journal of materials science*, 44(14):3807–3812.

May, J., Höppel, H., and Göken, M. (2005). Strain rate sensitivity of ultrafine-grained aluminium processed by severe plastic deformation. *Scripta materialia*, 53(2):189–194.

May, J., Höppel, H. W., and Göken, M. (2006). Strain rate sensitivity of ultrafine grained fcc-and bcc-type metals. In *Materials Science Forum*, volume 503, pages 781–786. Trans Tech Publ.

Merklein, M. and Vogt, U. (2009). Enhanced formability of ultrafine-grained aluminum blanks by local heat treatments. *Key Engineering Materials*, 410:169–176.

Meyers, M. and Chawla, K. (1984). Mechanical metallurgy: Principles and applications.

Mishin, O., Bay, B., and Jensen, D. J. (2000). Through-thickness texture gradients in cold-rolled aluminum. *Metallurgical and Materials Transactions A*, 31(6):1653–1662.

Mishin, O., Bay, B., Winther, G., and Jensen, D. J. (2004). The effect of roll gap geometry on microstructure in cold-rolled aluminum. *Acta materialia*, 52(20):5761–5770.

Mishra, S., Desai, S. G., Pant, P., Narasimhan, K., and Samajdar, I. (2009). Improved predictability of forming limit curves through microstructural inputs. *International Journal of Material Forming*, 2(1):59–67.

Molotnikov, A., Lapovok, R., Gu, C., Davies, C., and Estrin, Y. (2012). Size effects in micro cup drawing. *Materials Science and Engineering: A*.

Moreno-Valle, E., Monclus, M., Molina-Aldareguia, J., Enikeev, N., and Sabirov, I. (2012). Biaxial deformation behavior and enhanced formability of ultrafine-grained pure copper. *Metallurgical and Materials Transactions A*, pages 1–10.

Norfleet, D., Dimiduk, D., Polasik, S., Uchic, M., and Mills, M. (2008). Dislocation structures and their relationship to strength in deformed nickel microcrystals. *Acta Materialia*, 56(13):2988–3001.

Petch, N. (1953). The cleavage strength of polycrystals. *J. Iron Steel Inst.*, 174:25–28.

Raghavan, K. (1995). A simple technique to generate in-plane forming limit curves and selected applications. *Metallurgical and Materials Transactions A*, 26(8):2075–2084.

Rees, D. and Power, R. (1994). Forming limits in a clad steel. *Journal of materials processing technology*, 45(1):571–575.

Sabirov, I., Barnett, M., Estrin, Y., and Hodgson, P. (2009). The effect of strain rate on the deformation mechanisms and the strain rate sensitivity of an ultra-fine-grained al alloy. *Scripta materialia*, 61(2):181–184.

Saito, Y., Tsuji, N., Utsunomiya, H., Sakai, T., and Hong, R. (1998). Ultra-fine grained bulk aluminum produced by accumulative roll-bonding (arb) process. *Scripta Materialia*, 39(9):1221–1227.

Saito, Y., Utsunomiya, H., Tsuji, N., and Sakai, T. (1999). Novel ultra-high straining process for bulk materials development of the accumulative roll-bonding (arb) process. *Acta materialia*, 47(2):579–583.

Shi, X., Mishra, R. S., and Watson, T. (2008). Effect of temperature and strain rate on tensile behavior of ultrafine-grained aluminum alloys. *Materials Science and Engineering: A*, 494(1):247–252.

Skjødt, M., Silva, M., Martins, P., and Bay, N. (2010). Strategies and limits in multi-stage single-point incremental forming. *The Journal of Strain Analysis for Engineering Design*, 45(1):33–44.

Swift, H. (1952). Plastic instability under plane stress. *Journal of the Mechanics and Physics of Solids*, 1(1):1–18.

Takata, N., Okitsu, Y., and Tsuji, N. (2008). Dynamic deformation behavior of ultra fine grained aluminum produced by arb and subsequent annealing. *Matter Sci*, 43:7385–7390.

Truszkowski, W., Krol, J., and Major, B. (1982). On penetration of shear texture into the rolled aluminum and copper. *Metallurgical transactions A*, 13(4):665–669.

Tsuji, N. (2010). New routes for fabricating ultrafine-grained microstructures in bulky steels without very-high strains. *Advanced Engineering Materials*, 12(8):701–707.

Tsuji, N., Ito, Y., Saito, Y., and Minamino, Y. (2002). Strength and ductility of ultrafine grained aluminum and iron produced by arb and annealing. *Scripta materialia*, 47(12):893–899.

Tsuji, N., Saito, Y., Lee, S., and Minamino, Y. (2003). Arb (accumulative roll-bonding) and other new techniques to produce bulk ultrafine grained materials. *Advanced Engineering Materials*, 5(5):338–344.

Tsuji, N., Saito, Y., Utsunomiya, H., and Tanigawa, S. (1999). Ultra-fine grained bulk steel produced by accumulative roll-bonding (arb) process. *Scripta materialia*, 40(7):795–800.

Valiev, R., Korznikov, A., and Mulyukov, R. (1993). Structure and properties of ultrafine-grained materials produced by severe plastic deformation. *Materials Science and Engineering: A*, 168(2):141–148.

Valiev, R. Z. (1997). Structure and mechanical properties of ultrafine-grained metals. *Materials Science and Engineering: A*, 234:59–66.

Valiev, R. Z., Krasilnikov, N., and Tsenev, N. (1991). Plastic deformation of alloys with submicron-grained structure. *Materials Science and Engineering: A*, 137:35–40.

Valiev, R. Z. and Langdon, T. G. (2006). Principles of equal-channel angular pressing as a processing tool for grain refinement. *Progress in Materials Science*, 51(7):881–981.

Verlinden, B. e. a. (2007). *Thermo-Mechanical processing of metallic materials*. Elsevier, first edition.

Wei, Q. (2007). Strain rate effects in the ultrafine grain and nanocrystalline regimes influence on some constitutive responses. *Journal of Materials Science*, 42(5):1709–1727.

Wei, Q., Cheng, S., Ramesh, K., and Ma, E. (2004). Effect of nanocrystalline and ultrafine grain sizes on the strain rate sensitivity and activation volume: fcc versus bcc metals. *Materials Science and Engineering: A*, 381(1):71–79.

Winther, G., Huang, X., Godfrey, A., and Hansen, N. (2004). Critical comparison of dislocation boundary alignment studied by tem and ebsd: technical issues and theoretical consequences. *Acta materialia*, 52(15):4437–4446.

Yoda, R., Shibata, K., Morimitsu, T., Terada, D., and Tsuji, N. (2011). Formability of ultrafine-grained interstitial-free steel fabricated by accumulative roll-bonding and subsequent annealing. *Scripta Materialia*, 65(3):175–178.

Yu, C., Kao, P., and Chang, C. (2005). Transition of tensile deformation behaviors in ultrafine-grained aluminum. *Acta Materialia*, 53(15):4019–4028.

Yu, T., Huang, X., and Winther, G. (2011). *Recovery and recrystallization of nanostructured metals - mechanisms and kinetics*. Risø-PhD-79(EN). Risø National Laboratory for Sustainable Energy.

Zehetbauer, M. and Seumer, V. (1993). Cold work hardening in stages iv and v of fcc metals - i. experiments and interpretation. *Acta metallurgica et materialia*, 41(2):577–588.

DTU Vindenergi er et institut under Danmarks Tekniske Universitet med en unik integration af forskning, uddannelse, innovation og offentlige/private konsulentopgaver inden for vindenergi. Vores aktiviteter bidrager til nye muligheder og teknologier inden for udnyttelse af vindenergi, både globalt og nationalt. Forskningen har fokus på specifikke tekniske og videnskabelige områder, der er centrale for udvikling, innovation og brug af vindenergi, og som danner grundlaget for højt kvalificerede uddannelser på universitetet.

Vi har mere end 240 ansatte og heraf er ca. 60 ph.d. studerende. Forskningen tager udgangspunkt i ni forskningsprogrammer, der er organiseret i tre hovedgrupper: vindenergisystemer, vindmølleteknologi og grundlag for vindenergi.

Danmarks Tekniske Universitet
DTU Vindenergi
Nils Koppels Allé
Bygning 403
2800 Kgs. Lyngby
Telefon 45 25 25 25

info@vindenergi.dtu.dk
www.vindenergi.dtu.dk